Diss.ETH NO: 25829

Old dates, cool stories: Radiocarbon dating trees in the last cooling event

A Thesis submitted to attain the degree of

DOCTOR OF SCIENCES ETH-ZURICH
(Dr.sc. ETH Zurich)

presented by
ADAM SOOKDEO

M.Sc University of Ottawa
born on
27.07.1988
citizen of Canada

Accepted based on the recommendation of
Prof. Tim Eglinton, examiner
Prof. Hans-Arno Synal, co-examiner
Dr. Lukas Wacker, co-examiner
Assistant Prof. Micheal Dee, co-examiner
2019

Abstract

The field of radiocarbon (^{14}C) changed when tree-rings were first shown to be a direct proxy for atmospheric ^{14}C. Long-term measurements of ^{14}C derived from tree-ring chronologies showed 'wiggles' that were caused by carbon cycle, geomagnetic and solar variability. The presence of these 'wiggles' also meant a ^{14}C age had to be calibrated. The first ^{14}C calibration curve was built from tree-ring chronologies and to this day tree-ring chronologies are considered the gold standard. The most extensive tree-ring chronology extends from AD 1950 (considered present) into the most recent return to near glacial like conditions, called the Younger Dryas (YD). The cause of the YD remains a mystery, but with the discovery of 253 late-glacial pines in 2013 from Zürich, Switzerland reignited a 30-year effort to extend the most extensive (or absolute) tree-ring chronology further back in time.

To determine how old newly discovered trees were and avoid alternative time consuming and costly dating techniques we created Speed Dating: a breakthrough in direct Accelerator Mass Spectrometer (AMS) ^{14}C measurements of gas samples. Instead of going through conventional preparation techniques, wood samples were directly combusted in an elementar analyzer with the resulting CO_2 measured for its ^{14}C content on an AMS system. The Speed Dating technique was shown to be robust with excellent standard normalization, reproducible blanks and accurate dating of reference materials. Further, Speed Dating resulted in an increase of sample throughput by 15x with uncertainties of $\leq 2‰$ and the cost of an AMS date was reduced by a third.

Trees identified as potential candidates for extending the absolute tree-ring chronology, were subjected to high-precision ^{14}C dating. As no well-defined methodology exists for high-precision ^{14}C dating by AMS, we created the Quality Dating protocol an outcome of the 1705 samples we measured at ETH. The Quality Dating protocol stipulated that for high-precision ^{14}C dates by AMS, process rather than chemical blanks are to be used as an estimate of contamination. This was outcome of processed wood blanks on average, being statically different than chemical blanks. Further, standards should always be accompanied by another standard to ensure robust normalization, which was observed via a normalization of Oxalic acid II & to Oxalic acid I. Lastly, at least two references of similar composition and age to the analyte should be measured to confirm reproducible results. This was demonstrated by continual measurements of a wood sample that was ^{14}C dated by five other laboratories. By following the Quality dating protocol, an intercomparison with laboratory from Germany showed exemplary agreement in ^{14}C ages and uncertainty estimations.

The abundance of ^{14}C dates produced in this dissertation were from four chronologies, the absolute chronology and three Swiss chronologies-not linked to the present day. The absolute chronology was extended 200 years further back in time-based on high precision ^{14}C. The extended ^{14}C record of the absolute chronology could be linked to one of the Swiss chronologies. In turn, this Swiss chronology could be used to anchor the remaining chronologies. A higher calendrical certainty ($2\sigma \leq 8$ cal years) was obtained when wiggle matching to a New Zealand chronology. That was wiggle-matched to the extended absolute chronology. The ^{14}C record before and during YD was redefined with quicker increase and decrease in ^{14}C than previously noted.

The ^{14}C production estimated from the rise in atmospheric ^{14}C is increased by 20% for a period of 400 years starting at $\sim$ 12.8 kyr BP. While this increased production could be caused by either a change in geomagnetic field or oceanic circulation, century variations are akin to patterns seen in the Holocene that are assumed to be solar driven. Inferred from the correlation between total solar irradiance and ^{14}C production for recent times, we estimate that the total solar irradiance the in the YD could have been reduced by ≥ 5 W m^{-2}, which is larger than previously speculated. This could mean that a weak Sun had more a role to play in the most recent return to near glacial-like conditions of the YD.

We use the precision of our new ^{14}C record to align climatic signatures seen in various

archives for the YD to the 20% increase ^{14}C production and investigate the InterHemispheric Gradient (IHG)- the ^{14}C difference in tree-rings growing at the same time on the northern and the southern hemisphere. The elevated IHG is elevated accompanied with intense variability for ~600 year period. The change in the IHG we associate to three variations in carbon cycle that mark beginning of the YD cooling event. The first being the grand solar minimum (mentioned above) that would create a ^{14}C gradient towards the pole regions cause by the increased production. This ^{14}C gradient would be broadened by the second component, a weaker Meridional Overturning Circulation that increases concentration of atmospheric $^{14}CO_2$ in the Northern Hemisphere. The change in concentration would further be exacerbated by third a change to carbon cycle, due to an increase in strength of the Southern Ocean circulation and westerlies winds. This change would deplete atmospheric $^{14}CO_2$ in the Southern Hemisphere, promoting the observed change in IHG. The precise timing of these events (within uncertainties) and the IHG change can be considered synchronous. Oddly, the IHG change is ~100 before changes associated with YD are detected in the German Meerfelder Maar chronology. We believe this to indication that calendrical uncertainties of the Meerfelder Maar chronology are underestimated.
The work introduced in this dissertation:

- Adds and improves on existing AMS methodologies.
- Redefines placement and structure of ^{14}C during cooling event.
- Precisely identifies the largest known solar driven change.
- Synchronize various records in the YD
- Discovers an IHG change that is due to production and carbon cycle variations in the YD.

This dissertation will serve as a reference for ^{14}C studies in the future that would aim to improve calibration and understand ancient carbon cycle changes.

Zusammenfassung

Die Erkenntnis, dass Baumringe ein direktes Archiv des atmosphärischen Radiokohlenstoff (^{14}C) Pegels sind, hatte grossen Einfluss auf die ^{14}C-Methode. Lange Zeitserien von ^{14}C Messungen zeigten 'wiggles', die durch den Kohlenstoffkreislauf und Schwankungen des Erdmagnetfelds und der Sonnenaktivität verursacht wurden. Die Existenz dieser 'wiggles' bedeutet auch, dass ^{14}C-Alter kalibriert werden müssen. Die erste Kalibrationskurve wurde mit Hilfe von Jahrring-Chronologie erstellt, und bis zum heutigen Tag werden Jahrring-Chronologien als Goldstandard angesehen. Die längste Jahrring-Chronologie erstreckt sich von AD 1950 (Nullpunkt der Skala) bis zum letzten grossen Klimarückgang in nahezu eiszeitliche Verhältnisse, genannt 'Jüngere Dryas'. Es bleibt ein Rätsel, was die Jüngere Dryas ausgelöst hat, aber die Entdeckung von 253 spätglazialen Kiefern in Zürich, Schweiz, fachte von Neuem eine 30-jährige Anstrengung zur Ausweitung der absoluten Baumringchronologie in die Vergangenheit an.

Um das Alter der neu entdeckten Bäume zu bestimmen, und um langwierige und kostspielige Datierungstechniken zu vermeiden, entwickelten wir 'Speed Dating': Ein Durchbruch im Hinblick auf direkte Massenbeschleunigermessungen (AMS) von ^{14}C Gasproben. Anstatt der üblichen Aufbereitung wurden die Holzproben direkt in einem Elementar-Analysator verbrannt und das entstandene CO_2 im AMS System auf den ^{14}C Gehalt gemessen. Wir zeigten, dass die Speed-Dating Technik ausgezeichnete Normalisierung in Bezug auf den Standard, reproduzierbaren Maschinen-Untergrund und genaue Daten von Referenzproben aufweist. Speed-Dating ergab einen 15-fach höheren Probendurchsatz bei Fehlern $\leq 2\%$, und die Kosten einer AMS-Altersbestimmung wurde um ein Drittel verringert.

Bäume, die als potentielle Kandidaten für den Ausbau der absoluten Baumring-Chronologie identifiziert wurden, wurden für Messungen mit hoher Genauigkeit vorgesehen. Da es noch keine wohldefinierte Methodologie für die Hochpräzisionsdatierung mit AMS gibt, haben wir als Ergebnis der Messung von 1705 Proben an der ETH das 'Quality Dating Protocol' geschaffen. Das Protokoll legt fest, dass für Untergrundproben von Hochpräzisionsmessungen mit AMS anstelle von chemische Substanzen Proben-nahe Materialien zu verwenden sind. Dies folgte daraus, dass Untergrund-Holzproben im statistischen Mittel von chemischen Untergrundproben abwichen. Weiter sollen beide Standards zusammen verwendet werden, wie der Vergleich von Oxalsäure II zu Oxalsäure I belegte. Schliesslich sollten mindestens zwei Referenzproben von ähnlicher Zusammensetzung und Alter wie die Proben gemessen werden, um die Reproduzierbarkeit zu bestätigen. Dies wurde durch fortlaufende Messungen einer Holzprobe gezeigt, die von 5 anderen AMS-Labors datiert wurde. Auf der Basis des Quality Dating Protokolls zeigte ein Vergleich mit einem deutschen Labor eine beispielhafte Übereinstimmung in ^{14}C –Altern und Fehlerbestimmungen.

Die Mehrzahl der ^{14}C-Daten dieser Dissertation stammen von vier Chronologien, der absoluten Chronologie und drei Schweizer Chronologien, die nicht an die absolute Chronologie angeschlossen sind. Die absolute Chronologie wurde mit hochpräzisen Daten um 200 Jahre zum Älteren verlängert. Die verlängerte ^{14}C-Datensatz der absoluten Chronologie konnte mit einer der Schweizer Chronologien verbunden werden. In der Folge konnten mit dieser Chronologie die übrigen Chronologien verankert werden. Eine weitere zeitliche Festlegung ($2\sigma \leq 8$ cal Jahre) wurde mit einem wiggle-match zu einer Neuseeländischen Chronologie erreicht, die ihrerseits zur erweiterten absoluten Chronologie über wiggle-matching angeschlossen wurde. Die ^{14}C -Zeitreihe vor und in der Jüngeren Dryas wurde neu bestimmt, mit schnelleren Anstiegen und Abfällen im Vergleich zu früheren Daten.

Die aus dem atmosphärischen ^{14}C Anstieg abgeleitete ^{14}C Produktion ist über einen Zeitbereich ab $\sim$ 12.8 kyr BP über einen Zeitbereich von 400 Jahren um 20% erhöht. Während die erhöhte Produktion theoretisch auch mit Änderungen in der Stärke des Erdmagentfeldes oder Änderungen in ozeanischer Zirkulationen erklärt werden könne, so ähnelt die Struktur stark Strukturen im Hololzän, die durch Änderungen in totaler solarer Irradianz erklärt werden. Abgeleitet aus der beobachteten Beziehung zwischen der solaren Irradianz und der beobachteten ^{14}C Produktion,

schätzen wir eine um ≥ 5 W m^{-2} abgeschwächte solare Irradianz für die YD ab, was mehr ist, als bisher abgeschätzt wurde. Das könnte bedeuten, dass die Sonne eine bedeutendere Rolle für die letzte kurzzeitige Rückkehr zu nahezu glazialen Bedingen der YD gespielt hat.

Wir verwenden den neu ^{14}C Rekord um die klimatische Signaturen, die in verschiedenen Archiven beobachtet werden, mit der um 20% erhöhten ^{14}C Produktion zu synchronisieren, und untersuchen den interhemisphärischen Gradienten (IHG) – derm ^{14}C Unterschied von zeitgleich gewachsenen Baumrichen der nördlichen und der südlichen Hemisphäre. Der IHG ist über ~600 Jahre hinweg erhöhte, kombiniert mit einer erhöhten Variabilität. Die Änderung des IHG wird auf mit drei Änderungen im Kohlenstoff Kreislauf zu Beginn der YD zurück geführt. Die Erste ist ein grosses solares Mimimum (wie zuvor erwähnt), das durch die erhöhte ^{14}C Produktion einen ^{14}C Gradienten hin zu den Polregionen verursacht. Dieser ^{14}C Gradient wird durch eine zweite Komponente verstärkt, eine schwächere thermohaline Zirkulation (Meridional Overturning Circulation, MOC), die atmosphärisches $^{14}CO_2$ in der Nordhemisphäre erhöhen würde. Die erhöhte Konzentration würde weiter verstärkt durch die dritte Änderung im Kohlenstoff Kreislauf, verursacht durch einen erhöhten Zirkulation der Südozeans und erhöten Westwinden. Diese Änderungen würde das atmosphärische $^{14}CO_2$ auf der Südhemisphäre abreichern und den IHG erhöhen. Merkwürdigerweise werden die Änderungen im IHG in der Chronologie des Meerfelder Maars 100 Jahre früher als diejenigen der Jüngeren Dryas beobachtet. Wir vermuten, dass die Fehlerbreite der Zeitskala des Meerfelder Maar unterschätzt ist.

Neu Beiträge in dieser Dissertation:

- Neue und verbesserte Methodologien für AMS
- Neue Festlegung und Struktur von ^{14}C einer Abkühlungsphase
- Synchronisierung von Eiskernen
- Genaue Identifizierung des größten bekannten Grand Solar Minimum
- Entdeckung eines IHG Verlaufs in der Jüngeren Dryas, ausgelöst durch den Kohlenstoffkreislauf

Diese Dissertation wird als Referenz für zukünftige^{14}C Studien dienen, die die ^{14}C Kalibration verbessern und Änderungen im Kohlenstoffkreislauf der Vergangenheit verstehen wollen.

Contents

Chapter 1

Introduction

1.1 Motivation

On a fateful day in 2013, a technician (Daniel Nievergelt) from the forest, snow and landscape research institute was searching for a buried treasure that-with the right scientific tools-could tell a tale of climates long past. What was he looking for? To answer that question, we need to start at the beginning.

In 1929 A.E Douglass made use of tree-rings for dating ancient Indian ruins. In that he assumed tree-rings grow annually, where we now know of the possibility of missing tree-rings (Baillie and Munro, 1988) and that trees could be matched to each other by a common tree-ring growth signal (Douglas, 1929). By matching trees of different ages together, a chronology stretching in time could be built that Douglas (1929) termed dendrochronology. The tree-ring growth patterns of ancient Indian ruins were matched to a dendrochronological record that allowed Douglas (1929) to determine the exact year the runes were built. What he did not know was tree-rings could tell more than just time.

As tree-rings grow their width is dictated by local temperature and precipitation (LaMarche, 1974) with measurements ^{18}O serving as a proxy (Pearman et al., 1976). The radiocarbon (^{14}C) concentration in tree-rings reflect $^{14}CO_2$ fixed from the atmosphere during photosynthesis (Suess 1980). ^{14}C measurements over the last 8000 years from a dendrochronological record showed visible oscillation of ^{14}C with time, referred to as 'wiggles' (Suess, 1980). The ^{14}C wiggles were (and still are) a result of past changes to the ocean, Sun and geomagnetic field (Stuiver and Braziunas, 1993). These changes affected the premise of ^{14}C dating (Suess, 1980).

^{14}C dating was built on the premise that the radioactive decay of ^{14}C, which has a half-life of 5730 years (Godwin, 1962), equated to calendar years (Arnold and Libby, 1949). When in fact, a ^{14}C date can only be assigned to a calendar year through calibration. Hence the birth of a calibration curve made-up of ^{14}C dates derived from a dendrochronology record extending from 1950 AD (treated as the present) to 4450 years Before Present (cal BP) comprised of American trees (Stuiver and Becker, 1986). Now, the world's most extensive dendrochronological record used for ^{14}C calibration comes from Germany, extending from the present to 12 410 cal BP (Friedrich et al., 2004). The oldest part of this chronology is in the Younger Dryas (YD) where in Germany and the rest of Northern Hemisphere had returned to near-glacial like conditions (Dansgaard et al., 1986; Brauer et al., 2008; Steffensen et al., 2008).

The YD began around 12.9 cal kBP marking the end of a warm period known as the Allerød (Steffensen et al., 2008). The Allerød-YD transition has been theorized to be a result of strong stormy conditions (Brauer et al., 2008), low solar activity (Renssen et al., 2000) and weak ocean circulation (Broecker et al., 1989) or a combination of all three (Renssen et al., 2015). Accurately placed ^{14}C dates during this period would aid in our understanding of solar variability and ocean changes (Muscheler et al., 2000; Goslar et al., 2000; Muscheler et al., 2008; Hua et al., 2009; Hogg et al., 2016). Felix Kaiser and his colleagues tried to extend the German chronology record with

floating Swiss chronologies (Friedrich et al., 2004; Kromer et al., 2004; Schaub et al., 2008; Hua et al., 2009; Kaiser et al., 2012) that proved inauspicious (Hogg et al., 2016). This was primarily due to different regional tree-ring growth conditions and limited ^{14}C overlap.

^{14}C dates for the oldest part of the PPC are scarce with 12 dates spanning 425 years. These ^{14}C dates were determined on a Gas Proportional Counter (GPC) that requires large sample sizes (> 15g) and measurement times up to 10 days (Kromer et al., 2004). Not all trees found were viable for ^{14}C dating, leading to a total of 121 dates spanning 900-yr. The passing of Felix Kaiser in 2012, ceased efforts to extend the German chronology and improve the ^{14}C record in Allerød-YD. Until that fateful day in 2013 where a technician discovered a tree-stump at a construction site in Zürich, Switzerland.

Figure 1.1: Tree stumps recovered from a construction site in Binz, Zürich

Frequent trips to the construction site yielded 253 well-preserved pine (Pinus sylvestris L.) tree- stumps (Fig 1.1), a subset (n = 10) of which were ^{14}C dated. These dates spanned the gap between the absolute German chronology and Swiss floating chronologies. Hence, these pines trees (henceforth known as Binz trees) along with decreased sample size and increased throughput of ^{14}C dates by Accelerator Mass Spectrometry (AMS) offered the potential to accurately place and increase the number of ^{14}C before and during a cooling event. This would further tie into ^{14}C calibration as well synchronization of paleoclimate records during this period. In an endeavour to do just that as well as improve dendrochronological links and temperature reconstruction using δ^{18}O a proposal was submitted to the Swiss National Foundation (SNF).

The SNF proposal was accepted (proposal number 200021L-157187) with three PhDs funded. The first PhD Frederick Reinig was given the task to find dendrochronological links between the German chronology and Swiss trees. The second PhD Maren Pauly was given the task reconstructing temperature. And the third PhD, myself was selected to measure ^{14}C by AMS. Thus, the focus of this dissertation is to: improve on existing AMS ^{14}C dating techniques, accurately and precisely extend the tree-ring based ^{14}C record during the Allerød-YD and synchronize other paleo-records allowing for an investigation into changes in the ocean, Sun and geomagnetic field.

1.2 Measurement techniques for ^{14}C

While the majority of this dissertation is focused on improving existing AMS techniques of ^{14}C dating (Chapter 2 and 3) and the application of ^{14}C dates (Chapter 4) it is relevant to discuss the history and evolution of ^{14} measurement techniques.

^{14}C measurement began with Gas Proportional counters (GPC) that detected the electrons originating from beta decay of ^{14}C (Libby, 1961). These measurements were initially limited to environmental levels of ^{14}C unless laboratories were built deep underground (Loosli et al., 1980).

Eventually, with improvements of detectors and removal of gas impurities-that scavenge electrons or produce false positives (Kromer and Münnich, 1992 and references therein)- samples as old as 14 cal kBP could be measured (Kromer et al., 2004). While impressive, a significant drawback still existed for GPC; the relatively large amount of material (>15g of wood) and measurement times ($gleq$ ten days) required. These drawbacks stem from indirect measurements of ^{14}C.

Directly measuring ^{14}C atoms may seem trivial with mass spectrometers existing nearly since the beginning of the 20th century (Aston, 1919) but direct measurements of ^{14}C atoms presented two fundamental problems 1) it has a natural abundance of 1 part per trillion and 2) measurements of ^{14}C atom can be overshadowed by a natural competitor nitrogen (^{14}N) and molecular interferences. The advent of AMS solved these problems.

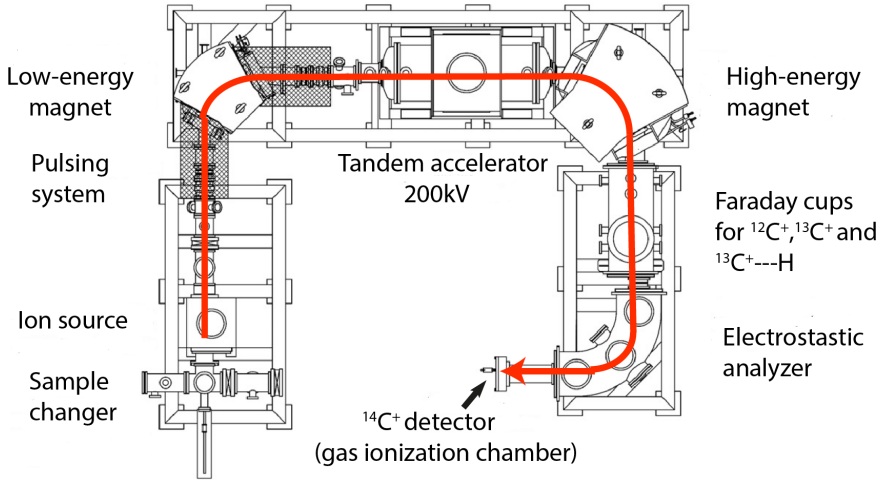

Figure 1.2: Stardard MICADAS set-up. Beam path's interaction with the components of an MICADAS (see chapter 1.2) is shown as red line. Image modified from Synal et al. (2007).

While AMS systems come in a variety of shapes and sizes (Suter, 2004), they all operate under the same fundamental principles. First, a negative ^{14}C ion beam[1] is created that suppresses the enormously abundant ^{14}N isobar as ^{14}N is incapable of forming negative ions (Bennett et al., 1977; Muller, 1997). The negative ion beam (E/q) can sometimes pass through an ElectroStatic Analyser (ESA) which selects ions with a specific energy. The beam is then subjected to an accelerator tube with a pulsing potential to ensure carbon isobar beams ^{12}C and ^{13}C have the same momentum as ^{14}C (Suter et al. 1984). Alternatively, a bouncing magnetic field can be applied that acts a momentum filter (Sie et al., 2000). Irrespective of the method used to select the beam, a magnet is always used as momentum filter. This magnet is often called the low energy magnet as afterwards the beams travel to a tandem accelerator. Here the beams of carbon are accelerated to a terminal with a considerable potential that can be up to several MeV. The carbon beams then pass through a gas or a foil where they are stripped of their charge. The newly formed positive carbon beams are accelerated to a ground potential, which can be mathematically represented as $E = (q + 1)V$ (Fifield et al., 1999 and references therein). The stripping of the charge state rapidly breaks up molecular isobars either through coulomb explosion and/or molecular collision with an inert gas (Lee et al., 1984). This stripping process thus reduces the molecular isobar by several factors (Litherland, 1980; Lee et al., 1984; Suter et al., 1999). The accelerated beam is passed through another magnet acting as momentum filter, denoted as the high-energy magnet. The emerging

[1] a positive ion source mass spectrometer has been developed by Freeman et al. (2015) but is beyond the scope of this dissertation

$^{12}C^+$, $^{13}C^+$ and $^{13}C^+$ beam (derived from $^{13}CH^+$) are collected in Faraday cups (Synal et al., 2007). The $^{14}C^+$ beam continues pass the Faraday cups where it can be subjected to another mass filter magnet and almost always passes through an ESA to a gas ionization chamber (Fifield et al., 1999; Suter, 2004; Synal et al., 2007). This chamber can contain isobutane as it has high stopping power and has a substantial ionization efficiency-creating electron-ion pars that can be counted (Oed et al., 1988).

All of the ^{14}C dates produced during this dissertation derive from a compact AMS called MIni CArbon Dating System (MICADAS, Ionplus) that follows the principles as mentioned above with the distinction of having a pulse system on the low-energy side and gas-filled stripper (Synal et al., 2007). The advantage of a MICADAS over a GPC relates to sample throughput. Samples older than two half-lives required 1-3 day measurement times on a MICADAS while a GPC would require (for similar precision) a minimum of 10 days (Kromer et al., 2004). A general overview of a MICADAS is given in Fig 1.2.

1.3 Atmospheric ^{14}C

Beyond the application of atmospheric ^{14}C to serve as chronological tool (see motivation), atmospheric ^{14}C can be used to investigate paleo- changes in the ocean, Sun and geomagnetic field as these processes are capable of regulating the concentration of atmospheric ^{14}C (Stuiver and Braziunas, 1993). The production of ^{14}C occurs in the upper atmosphere through the interactions neutrons (n°) derived from cosmic ray particles and nitrogen atoms:

$$^{14}N + n^\circ \rightarrow ^{14}C + proton$$

The extent of cosmic rays entering the upper atmosphere can be modulated by the geomagnetic field (Mazaud et al., 1991; Laj et al., 1996; Hughen et al., 2004; Beer et al., 2012). This kind of modulation is observed as long trends (>1kyr) in ^{14}C production, which can only result from changes to the geomagnetic dipole strength as cosmic rays are deflected several Earth radii from the Earth surface (Mazaud et al., 1991; Beer et al., 2012). These changes in the dipole strength have occurred over the last 800 kyr with the most recent known as the Laschamp event taking place around 41 cal kB (Guyodo and Valet, 1999). More recent and readily occurring modulations of cosmic rays are a result of solar variability.

The Sun can modify atmospheric ^{14}C production on a daily, monthly, yearly and century basis (Beer et al., 2012) as cosmic rays passing through the magnetic field of the heliosphere are deflected (McDonald, 1998). The daily and monthly variations in the magnetic field of the heliosphere are not perceived in atmospheric ^{14}C archives due to yearly integration times (Stuiver and Quay, 1980; Bard et al., 1997; Solanki et al., 2004; Miyahara et al., 2007; Muscheler et al., 2007; Miyahara et al., 2010; Beer et al., 2012; Nagaya et al., 2012; Güttler et al., 2013; Usoskin, 2017). Yearly changes derived from the heliosphere can be small with a periodicity of 11-years having amplitudes upwards of 2.5‰ in $\Delta^{14}C$ (Stuiver and Quay, 1980). These 11-year cycles have been associated with the appearance of Sunspots. Sunspot variations are known as the Schwabe cycle (Hoyt and Schatten, 1998) and the prolonged absences of Sunspots are considered to be solar minima (Stuiver and Quay, 1980). These minima can vary in strength and duration -ultimately seen in $\Delta^{14}C$- with the most considerable and abrupt change observed at 7430 cal BP (Miyake et al., 2017). This minimum was theorized to be either an unknown phase of the Sun or a grand solar minimum in combination with successive solar proton events. Large solar minimums are believed to be the driving force behind the Little Ice age that occurred in the period AD 1300-1850 (Mauquoy et al., 2002; Mann et al., 2009). A solar proton event is likely the cause of a significant increase in $\Delta^{14}C$ seen between AD 774-775 (Miyake et al., 2012; Usoskin et al., 2013) and AD 993-944 (Miyake et al., 2013), which are hazardous to spacecraft's and astronauts (Xapsos et al., 2000). To investigate solar proton events, Schwabe cycle and solar minimums has led to a plethora of new annually resolved, high precision ^{14}C dates derived from tree-rings set to enter next iteration of the

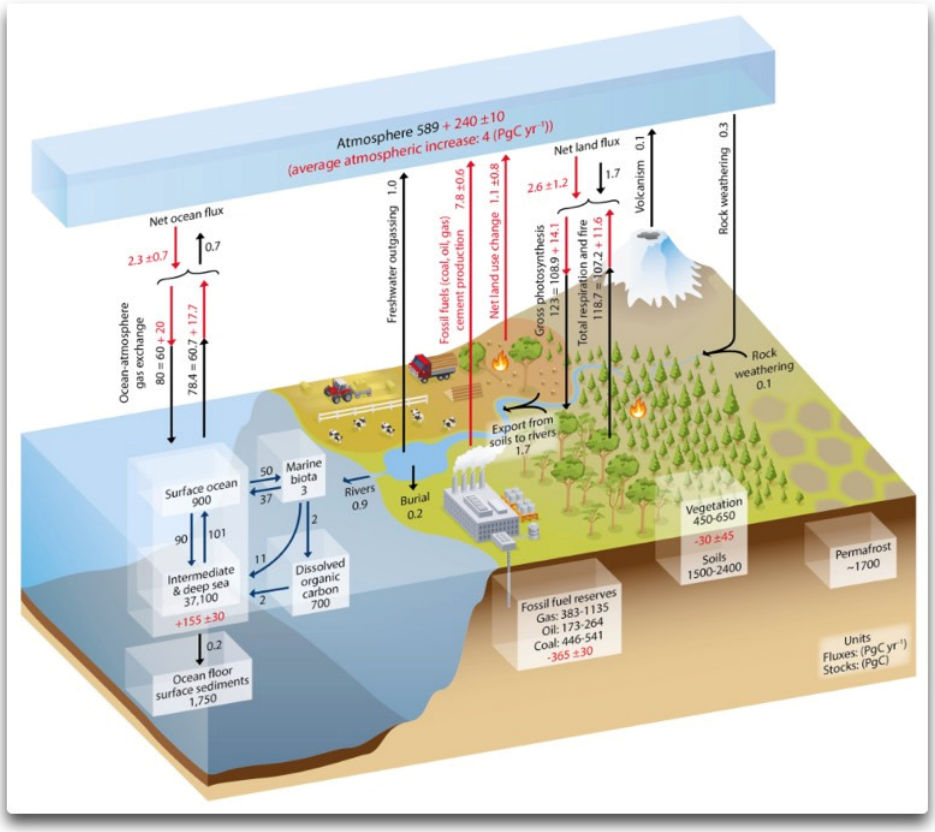

Figure 1.3: A simplified global carbon box model from the IPCC report, with values given in PgC (1 PgC = 10^{15} gC) and annual carbon exchange fluxes (Ciais et al. 2013)

international calibration curve. An added benefit of highly resolved high precision data sets allows for the investigation of oceanic variability.

Unlike the geomagnetic field and the Sun, the ocean variability does not affect production but rather varies the concentrations of atmospheric $^{14}CO_2$(Siegenthaler et al., 1980; Stocker and Wright, 1996). CO_2 is affected by carbon cycle with the most significant reservoir exchanging on timescales of $\geq$ 1 kyrs being the deep ocean (Fig 1.3; Siegenthaler et al., 1980; Stocker and Wright, 1996). Atmospheric ^{14}C derived from floating tree-ring chronologies (Kromer et al., 2004) observe abnormal increases during the YD that were associated (in part) with a downturn of deep ocean ventilation (Muscheler et al., 2000; Muscheler et al., 2008). However, a similar study of atmospheric ^{14}C derived from lake sediments indicated the changes observed in the YD could be explicable through solar modulation (Goslar et al. 2000). The different results from Muscheler et al. (2000 and 2008) and Goslar et al. (2000) can be associated with different atmospheric ^{14}C proxies containing high calendrical uncertainties and low resolution. Irrespective, these studies and those involving SPE as well as geomagnetic field variations require atmospheric ^{14}C to be coupled to ^{10}Be.

^{10}Be atoms are produced by high energy neutrons derived from cosmic rays analogous to ^{14}C production (Beer et al., 1994). Whereas ^{14}C is additionally affected by the carbon cycle, ^{10}Be is transported directly on aerosol to natural reservoirs such as ice-cores, reflecting production rates more directly (Beer et al., 1994; Bard et al., 1997; Muscheler et al., 2000; Muscheler et al., 2008). These effects can be disentangled by either converting atmospheric ^{14}C to production signal or ^{10}Be into atmospheric ^{14}C both of require the use of box model (Beer et al., 1994) that was outlined

by Oeschger et al. (1975) and Siegenthaler et al. (1980).

1.4 The cooling event: Younger Dryas

The YD was an abrupt return to near glacial like conditions with the disappearance of megafauna in the Northern Hemisphere (NH), recognized as early as 1901 in European pollen sequences (Hartz and Milthers) and clearly seen in Greenland ice cores (Johnsen et al., 1992; Alley et al., 1994). While several other proxies provide evidence for the YD, two things remain unclear 1) the cause and 2) the timing.

1.4.1 The cause of the Younger Dryas

Broecker et al. (1989) first proposed that a partial collapse of the Laurentide Ice sheet, which subsequently fed into the North Atlantic ocean, caused a complete collapse of the North Atlantic Deep Water (NADW) formation that lasted the duration of YD. As a result of the atmosphere over the ocean, which is usually warmed by the NADW, remained cold and consequently cooled Europe and North America (Broecker et al., 1989). Almost 20 years after Broecker et al., theory little to no evidence was found for the proposed path and source of fresh leading Broecker (2006) to conclude "our inability to identify the path taken by the flood is disconcerting." A year later, evidence of catastrophic flow (in support of Broecker et al., 1989) dated to 12.9 cal kBP-based on foraminifera found at the mouth of St. Lawrence estuary (Carlson et al., 2007)-was criticized by Peltier et al. (2008). Peltier et al. noted that previous studies in this area found no evidence of freshwater flux at 12.9 cal kBP. It was not until 2010 when Murton et al. discovered a 13 cal kBP flood path evident from gravels and regional erosion surface passing through the Mackenzie River to the Canadian Arctic Coastal Plain. The authors also rejected that the collapse of the Laurentide Ice sheet was solely eastward into the North Atlantic ocean and consequently would not result in a complete collapse of NADW.

Further studies indicated that the flow of fresh water coming from the Arctic would reduce the NADW by >30% (Condron and Winsor 2012) in agreement with McManus et al., (2004) observation of a rapid increase in ^{231}Pa/^{230}Th-a kinematic proxy for the meridional overturning circulation-around 12.8 cal kBP. However, a reduced NADW does not fit to previous models that assumed a full collapse as a trigger for the YD (Manabe and Stouffer, 1997). Strong winds were evident at the onset of YD from a paleoclimate record from Germany.

A floating lake sediment chronology from Meerfelder Maar (MFM), Germany extending to ~14 cal kBP (Brauer et al., 1999) contained consistently thick varves after ~12.7 cal kBP. These thick varves were accompanied by the cessation of siderite as a result of stormier conditions linked to changes in the Atlantic ocean and consequently mark the onset of YD in Germany (Brauer et al., 2008). Prior to onset of YD, an increase in ^{14}C from floating chronologies (Hajdas et al., 1998, 2003; Wohlfarth et al., 1998; Goslar et al., 2000; Kromer et al., 2004) was related to weak solar forcing.

The combination of weak solar forcing, stronger winds and weakening of the NADW were demonstrated to be key mechanisms involved in the onset of the YD (Renssen et al. 2015). However, the exact the magnitude of the forcings and interactions between them remain unclear. Further, by Renssen et al. own admission this does rule out the comet impact theory.

The comet impact theory that remains highly debated is instead of the collapse of the NADW, the impact of an asteroid would have released light-blocking dust into the sky, cooling North America (Firestone et al. 2007). South of the impact fiery projectiles would set forests alight, resulting in soot increasing the blockage of light and adding to the cooling (Kennett et al. 2008, 2009). Other groups could not detect the geochronological evidence proposed by Firestone et al. and the forest could have resulted from natural processes (see Pinter et al., 2011). The recent detection of an impact crater on Greenland, which evidence suggests it is between 100 to 12 cal

kBP old or even millions of years old (Kjaer et al., 2018) has renewed this theory with a twist. As Greenland at this time was covered in ice, a comet impact would have resulted in a massive amount of freshwater entering the Atlantic Ocean with similar to results to Broecker et al. (1989) theory, but indications for such a flood remains elusive.

1.4.2 The timing of the Younger Dryas

The exact timing of the onset the YD remains tentative. In GRIP (Johnsen et al., 1992), GISP2 (Alley, 2000) and NGRIP (Steffensen et al., 2008) ice-cores the onset of the YD is 12 700 ±100, 12 750 ±50 and 12 896 ±1.5 cal BP, respectively. While GRIP and GISP2 used δ^{18}O as an indicator for the onset of YD, NGRIP-the ice core with the highest resolution-used deuterium excess ($d = \delta D - 8\ \delta^{18}$O). Deuterium excess is a parameter that contains information on fractionation effects caused by the evaporation of source water that showed a 2-3‰ increase at 12 896 ± 1.5 cal BP representing a 2 to 4 K cooling of marine moisture (Steffensen et al., 2008). This shift is approx. 200 years before varve thickness increase and cessation of siderite occurs in MFM.

The cause for this discrepancy is still unclear. It could be that because both NGRIP and MFM have chronological uncertainties due to ice-ring or varve counting, respectively or there the 200-year delay is a mechanism of paleoclimate change that we have yet to understand.

The high resolution ^{14}C introduced in this dissertation aims to investigate solar variability during the YD (Chapter 3) and carbon cycle changes (Chapter 4).

1.5 Organization and objectives of this dissertation

This dissertation is structured in six main parts.

Chapter one is the introduction. It starts with the motivation for this work, and then three main subjects surrounding this dissertation. The first is an overview of the evolution measurement techniques, and the MICADAS used to produce a half-a-million CHF worth of ^{14}C measurements in this dissertation. The second is an overview of the paleo-environmental applications of atmospheric ^{14}C. The third is a summary of the mysteries surrounding a cooling event known as the Younger Dryas.

Chapter two presents the published paper in the journal of Radiocarbon© Speed Dating: A rapid way to determine the radiocarbon age of wood by EA- AMS, which was submitted before the end of the first year as PhD. Speed Dating represents a breakthrough in gas-based AMS dates that before were primarily used for samples with low carbon content. Instead of going through 'conventional' AMS preparation (see chapter 3) for wood samples, directly combusting and measuring the resulting CO_2 increased sample throughput by 15x, reduced the cost by a third with uncertainties of 2‰. The Speed Dating technique was used to identify Binz trees of interest for this project (Reining et al., 2018).

Chapter three introduces a paper accepted with revision(01/2019) submitted to the journal of Radiocarbon©, Quality Dating: A protocol for reproducible high precision ^{14}C dates applied to Late Glacial wood. This publication highlights the lack of protocols available to the academic community to ensure high precision ^{14}C measurements. The majority of high precision ^{14}C studies (a google search yielded 895 results) are not accompanied by measurements controls in place at the laboratory but often rely on guidelines set out by Intcal. Primarily an intercomparison study, which are also lacking (see Chapter 3); therefore, we introduce protocol that discusses quality assurances in place at ETH along with an intercomparison study. As a case study, we present new high precision dates for the Germany absolute chronology that fill a gap in IntCal13. It is our goal that this publication will serve as a guideline for other labs and create similar studies.

Chapter four reveals the extension of the absolute German chronology through wiggle-matching to Swiss trees that can also be confirmed by a tentative cross-dating performed by F. Reinig. Also, this chapter contains the calendrical placement of Swiss floating tree-ring chronology based on

^{14}C wiggle-matching. The placement of the chronologies along with 170 ^{14}C dates from the Quality Dating publication amounts to the largest density of high precision ^{14}C- a total of 1780- spanning before and after the YD. The ^{14}C dates are used to estimate production, which enables an investigation of solar variability in the YD. This chapter is presented in the format of Nature Geoscience and was submitted May 2019. This paper is titled, There goes the Sun: Reconstructing atmospheric ^{14}C reveals prolonged solar minimum in the Younger Dryas.

Chapter five is a discussion on the InterHemispheric Gradient (IHG) during the YD. The IHG is the occurrence of tree-rings growing at the same time having different hemispheric ^{14}C ages, which is controlled by the carbon cycle. In particular, the IHG is governed by more expansive ocean and strong winds in the Southern Hemisphere for the Holocene. We use the high-resolution and high precision measurement produce for this dissertation accompanied by an independent record from France and a well replicated Southern Hemisphere chronology to determine precisely the IHG. A long-lasting elevation in the IHG is discussed in relation to known climatic changes during the YD derived from various paleo-records. This defined IHG also highlights calendrical uncertainty in the critically important Meerfelder Maar chronology.

Chapter six brings us to the final section of this dissertation, the summary and outlook.

Chapter 2

Finding the right match through Speed Dating

This chapter contains the published version of Speed Dating: A rapid way to Determine the radiocarbon age of wood by EA-AMS (DOI 10.1017/RDC.2016.76), reprinted with permission of Cambridge University Press©. This paper was submitted within the first year of PhD and generated press in Germany. The paper is followed by a brief discussion on how Speed Dates were used to a build a dendrochronology record.

2.1 Speed Dating: A rapid way to Determine the radiocarbon age of wood by EA-AMS

Radiocarbon, Vol 59, Nr 3, 2017, p 933–939 DOI:10.1017/RDC.2016.76
Selected Papers from the 2015 Radiocarbon Conference, Dakar, Senegal, 16–20 November 2015

SPEED DATING: A RAPID WAY TO DETERMINE THE RADIOCARBON AGE OF WOOD BY EA-AMS

Adam Sookdeo[1,2*] • Lukas Wacker[1] • Simon Fahrni[1] • Cameron P McIntyre[1,2] • Michael Friedrich[3,4] • Frederick Reinig[5] • Daniel Nievergelt[5] • Willy Tegel[6] • Bernd Kromer[3] • Ulf Büntgen[5]

[1]Laboratory of Ion Beam Physics, ETH-Zürich, Physics, Otto-Stern-Weg 5, Zürich 8093 Switzerland.
[2]Carbon Cycle Biogeoscience, ETH-Zurich, Earth Sciences, Zürich, Switzerland.
[3]Heidelberg University, Envrionmental Physics, Heidelberg, Germany.
[4]Universitat Hohenheim, Botany, Stuttgart., Baden-Wurttemborg, Germany.
[5]Swiss Federal Research Institution WSL, Dendroecology, Birmensdorf, Switzerland.
[6]Albert-Ludwigs University Freiburg, Chair of Forest Growth and Dendroecology, Freiburg, Germany.

ABSTRACT. Radiocarbon measurements in tree rings can be used to estimate atmospheric ^{14}C concentration and thereby used to create a ^{14}C calibration curve. When wood is discovered in construction sites, rivers, buildings, and lake sediments, it is unclear if the wood could fill gaps in the ^{14}C calibration curve or if the wood is of historical interest until the age is determined by dendrochronology or ^{14}C dating. However, dendrochronological dating is subjected to many requirements and ^{14}C dating is costly and time consuming, both of which can be frivolous endeavors if the samples are not in the age range of interest. A simplified ^{14}C dating technique, called Speed Dating, was thus developed. It can be used to quickly obtain ^{14}C ages as wood samples are neither chemically treated nor graphitized. Instead, wood is combusted in an elemental analyzer (EA) and the CO_2 produced is carried into an accelerator mass spectrometer (AMS) with a gas ion source. Within a day, 75 samples can be measured with uncertainties between 0.5–2% depending on the age, preservation, and contaminants on the material and Speed Dating costs about one-third of conventional AMS dates.

KEYWORDS: ^{14}C, AMS dating, Speed Dating, MICADAS.

INTRODUCTION

Radiocarbon dates are routinely performed on tree rings of archaeological and naturally deposited wood as a dating tool and/or for determining past atmospheric ^{14}C concentration. When wood remnants are discovered at construction sites and in rivers, lake, and bog sediments, the absolute age often remains completely unknown until a dendrochronological and/or ^{14}C date can be established. The same is true when the date of historical artifacts (e.g. wooden art objects or construction time of buildings) is to be established. ^{14}C dating is of special importance as dendrochronological dating is subjected to many requirements (existence of chronologies, minimum number of rings, species, etc.) and is therefore often not immediately applicable (Cook and Kairiukstis 2013). While ^{14}C dates are typically applicable, conventional ^{14}C analysis by accelerator mass spectrometry (AMS) is relatively time consuming and expensive.

Conventional ^{14}C AMS measurements of wood involve chemical treatments to extract cellulose (Hoper et al. 1998; Brock et al. 2010; Němec et al. 2010). The cellulose is then converted to graphite by combustion and reduction, which can take several hours (Vogel et al. 1984; Xu et al. 2007; Wacker et al. 2010a). The graphitized samples are then analyzed by using an AMS fitted with Cs sputter sources (Vogel et al. 1984; Fifield 1999; Synal et al. 2007; Synal 2013), which are capable of high-precision measurements down to 2‰ on a modern sample (Calcagnile et al. 2005; Wacker et al. 2010b, 2014). This entire process is expensive and it can take over a week to prepare and measure 25 samples along with standards and blanks. As ^{14}C analysis by AMS requires an extraordinary amount of work, many samples that are collected are never dated and remain in storage. Advances in gas measurements of CO_2 by AMS (Bronk Ramsey et al. 2004;

*Corresponding author. Email: asookdeo@phys.ethz.ch.

Fahrni et al. 2013; Ruff et al. 2007) and coupling of an elemental analyzer (EA) to an AMS (Kieser et al. 2010; Ruff et al. 2010; Salazar et al. 2015) offer a novel way to ^{14}C date wood samples.

Here, we present a new method, called Speed Dating, that supersedes chemical preparation and graphitization to quickly ^{14}C date wood material. The objective of Speed Dating is to quickly determine (1) if the material falls into a time period interest of where data are scarce and, consequently, (2) whether the site where the material was discovered should be revisited to collect more samples.

METHOD

Sample Preparation and Measurement

All samples, standards, and blanks contained approximately 200 µg of carbon and were wrapped in aluminum capsules (4 × 4 × 11 mm, Elementar, Germany). For a standard, we used oxalic acid II (OXII, NIST SRM 4990C), for a chemical blank we used phthalic anhydride (PhA, Sigma-Aldrich, PN-320064-500 g), and as wood process blanks we used brown coal and kauri wood that are both older than 100,000 yr BP. The wrapped material is placed into an EA (vario MICRO cube, Elementar) where the material is combusted by flushing with oxygen for 50 s and the CO_2 produced is fed with helium carrier gas into a gas interface system (GIS, Ionplus).

In the GIS, the CO_2 is collected in a zeolite trap and then released into a gas syringe. The syringe is used to slowly inject CO_2 mixed with helium as carrier gas, into the ion source of a Mini Carbon Dating System (MICADAS, Ionplus) (Ruff et al. 2010; Wacker et al. 2013). The carbon concentration is kept consistent for all materials at 100 µg by pumping away excess CO_2. The initial setup and tuning is done on CO_2 combusted from OXII standard mixed with helium (1:20 v/v). In a procedure of about 15 min, we tune the ionization extraction potential, beam steerers in the x and y direction on the low-energy end, and the low- and high-energy magnets. More details about tuning a MICADAS can be found in Wacker et al. (2010b). The flow rate of CO_2 in helium carrier gas is adjusted to obtain maximum $^{12}C^-$ current (Fahrni et al. 2013; Wacker et al. 2013). Typically, a flow rate of 2.5 µg carbon per minute is supplied to the ion source and a $^{12}C^+$ current of 6–10 µA is measured in a Faraday cup placed after the accelerator. Detailed measurement parameters of an EA-GIS-MICADAS can be found in Fahrni et al. (2013). These measurements require minimal supervision.

Approximately 75 samples along with standards and blanks can be analyzed in a day. The EA can hold up to 120 samples at a time and samples can be continuously loaded while measurements are running. The gas cathodes used for the measurement are exchanged in a magazine every 38th sample while the measurement is running. A single sample is measured for 10–12 min, while the total time from combustion in the EA to the end of the ^{14}C analysis takes 13–15 min. The measurement of a single sample can be repeated in case a higher counting statistic, and thus a potentially higher measurement precision, is desired. Samples were bracketed by standards to detect any potential time-dependent variation. The estimated cross-contamination for an EA-AMS setup is less than 0.4% (Ruff et al. 2010). To limit correction from cross-contamination between samples with large differences in ^{14}C concentration (e.g. measurements of a standard followed by a blank), a duplicate was measured and the first measurement was considered void. Data reduction for Speed Dates and conventional AMS dates were done with the BATS program as described by Wacker et al. (2010c), in compliance with data processing for conventional AMS measurements.

During the course of a measurement, it seldom occurred that a sampled had to be remeasured. This could occur when an aluminum capsule becomes stuck in the EA sampler holder and fails to drop into the combustion tube or the inlet for CO_2 on a cathode is closed (Fahrni et al. 2013). These samples could be easily repeated by adding a duplicate at the end.

To evaluate the difference between Speed Dates and conventional AMS dates, samples from AD 770 were cellulose extracted using base-acid-base-acid-bleaching (BABAB) (Němec et al. 2010), and graphitized using an EA-AGE-3 (Wacker et al. 2010a).

DISCUSSION

Blanks and Standards

We measured the carbon content of aluminum capsules (Elementar, Germay) to be ~1 µg by combusting multiple capsules in an EA and measuring the resulting CO_2 concentration. To limit the effect of constant contamination from the Al capsules, we used sample weights of 200 µg of carbon. The measured ^{14}C content for the kauri and brown coal process blanks and the phthalic anhydride (PhA) process blank are given in Table 1. The kauri and brown coal process blanks showed a marginally higher level of contamination with a larger standard deviation than the PhA blanks. All blanks were weighed and wrapped in aluminum capsules at the same time and one would expect the same blank value for PhA and the process blanks. However, PhA comes from a stock bottle and the kauri and brown coal blanks are from relatively large pieces of wood that had to be cut into smaller sample sizes. By cutting these pieces of wood, we may have introduced minor ^{14}C contamination that explains the marginally higher ^{14}C content. As all woods were cut, the brown coal and kauri were considered to be appropriate for blank subtraction.

Three measurement campaigns of the standard OXII using the EA-GIS-MICADAS show a scatter that is in good accordance with the quoted measurement uncertainties (Figure 1). Standards were analyzed for 10–12 min until roughly 25,000 counts of ^{14}C were measured. The standard deviation was 0.008. This is due to counting statistics and the additional 0.4% uncertainty we add as sample scatter to account for variability of gas measurements by AMS (Bronk Ramsey et al. 2004; Fahrni et al. 2013; Wacker et al. 2013).

Measurements and Uncertainties

The uncertainties associated with AMS measurements arise from counting statistics, and the stability of the measurement over time (Wacker et al. 2010c). In addition, Speed Dating of untreated wood may have an additional offset compared to conventional AMS dates of cellulose because lignin and other parts of the wood (Gaudinki et al. 2005) or contamination

Table 1 Mean ^{14}C ages for three different blanks: a chemical blank (phthalic anhydride) and two process blanks (kauri and brown coal).

	Mean ^{14}C age (BP)	Standard deviation	Mean error (yr)	Nr of samples
Phthalic anhydride (PhA) blank	36,900	1400	560	4
Kauri wood blank	34,800	2800	400	5
Brown coal wood blank	34,300	3800	400	5

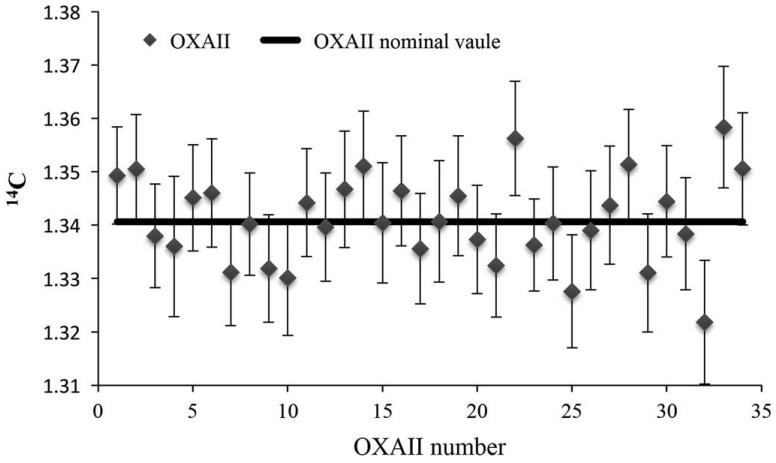

Figure 1 Fraction modern (^{14}C) values for 34 OXII samples that were analyzed by EA-GIS-MICADAS. Measurement times were between 10 and 12 min (25,000 counts of ^{14}C).

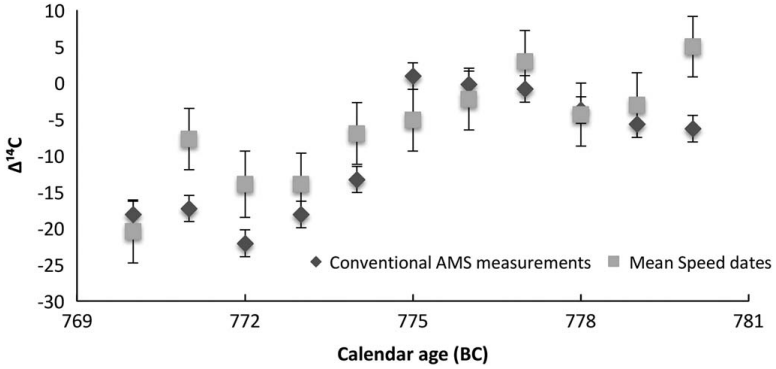

Figure 2 Mean Speed Dates and conventional AMS measurements for annual resolution between 770 and 780 BC. Speed Dates were done in triplicates.

from the matrix where samples were stored, which may have younger or older ^{14}C content than cellulose of a specific year.

We tested for any offsets of Speed Dating on annually resolved wood samples for the period AD 770–780, i.e. relatively modern wood. We measured this 10-yr period in triplicate and the same samples were dated conventionally (Figure 2). The mean Speed Date uncertainty was ±0.5% (±40 yr).

Two Speed Dates showed a slightly younger ^{14}C age than that of conventional AMS dates of cellulose. This is could be due to lignin or other parts of the wood that change over time as these compounds would introduce younger ^{14}C (Gaudinki et al. 2005). If the sample uncertainty is increased to 0.8%, Speed Dates and conventional AMS dates are within 2 standard deviations. In any case, Speed Dating provides a rapid estimate of ^{14}C age for relatively ^{14}C modern samples with acceptable precision.

Speed Dating was used to analyze 110 undated subfossil trees that were never ^{14}C dated as a contribution to the ongoing construction and extension of early Holocene and Late Glacial tree-ring chronologies (>10,000 BP). The samples age were determined to be between 14,500 to

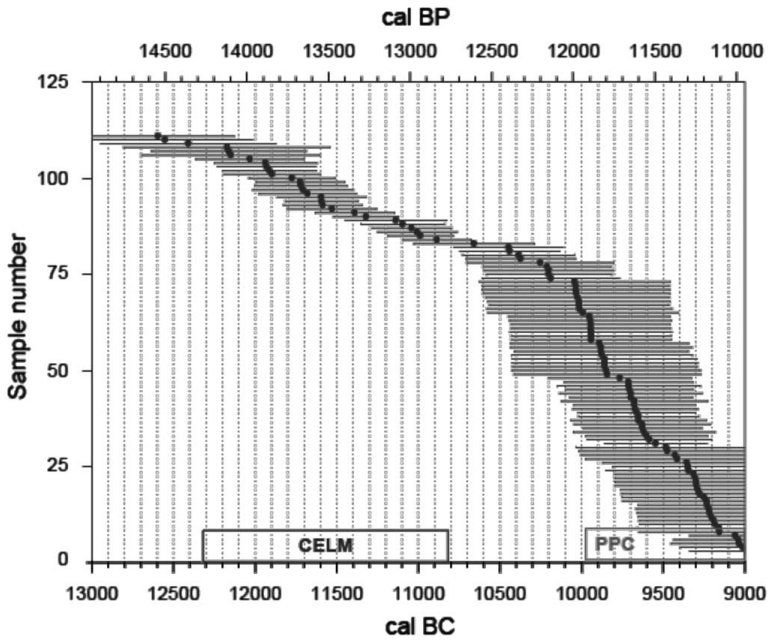

Figure 3 Calibrated Speed Dates using IntCal13 (Reimer et al. 2013) for 110 samples plotted with two Northern Hemisphere tree chronologies, CELM and PPC (see text). The span of a data point indicates the calibrated calendar age range based on Speed Dating results.

11,000 BP with uncertainties of 1–2% (80–160 yr) (Figure 3). These are acceptable uncertainties when the aim is to add a time constraint to material with no chronological context.

In addition, through Speed Dating we were able to suggest a rough chronological placement for trees that were older than 10,000 BP. The trees were placed around the Central European Lateglacial Master chronology (CELM) (Kaiser et al. 2012), and the Preboral Pine Chronology (PPC) (Friedrich et al. 2004) (Figure 3). Consequently, Speed Dating eliminated a vast majority of samples that were not of interest because these trees overlapped with CELM and PPC where already a large number of trees exist (Friedrich et al. 2004; Kaiser et al. 2012). However, 17 trees fell within the range of 12,700–11,100 BP, a period of time where Northern Hemisphere data are lacking in IntCal13 (Hogg et al. 2013; Reimer et al. 2013).

These were then dendrochronology matched (Table 2) with the expectation that the material could strengthen the tree-ring chronologies, possibly filling gaps in the Northern Hemisphere IntCal13 data set (Reimer et al. 2013) and/or potential link the floating CELM chronology to the absolutely dated European master chronology. Out of the 17 samples that were subsequently successfully dendrochronologically matched, two Speed Dates did not fall within the measurement uncertainty of the ^{14}C calendar range and were older than the dendrochronology date. This is not likely due to lignin or other parts of the wood that change over time as those compounds would introduce younger ^{14}C (Gaudinki et al. 2005). We speculate that theses samples have traces of older ^{14}C because of oil/gas residue, e.g. from when they were sampled in the field with a chainsaw or chalk used to mark the tree-ring numbers. Additionally, for sample ETH-61541, the outermost rings were sampled; thus, these rings may have had contact with carbonates or old carbon compounds from the surrounding soil. Normally, all of these contaminants would be removed by chemical pretreatment. Still, Speed Dating was capable to date those trees within ±400 yr of the true age determined with the dendrochronology.

Table 2 Speed Dates on subfossils pines from Breitenthal, southern Germany, compared to the respective dendrochronology dates on the same tree ring(s). *Indicates Speed Dates that do not agree within 2σ of the dendrochronology date. ^{14}C dates were calibrated with BATS using IntCal13 (Reimer et al. 2013).

Sample nr	Total nr of tree rings	Tree ring (s) sampled	Age (BP) ± error (yr)	cal age 2σ (BP)	Dendrochronology age (BP)
61507	118	11	10,090 ± 110	12,050–11,250	11,536
61512	77	5–10	10,050 ± 110	12,000–11,250	11,539
61505	107	90–100	10,090 ± 110	12,050–11,250	11,257
61504	81	80–81	10,250 ± 100	12,450–11,350	11,913
61503	139	60–70	10,080 ± 100	12,050–11,250	11,570
61510	112	10–15	9980 ± 100	11,850–11,150	11,659
61527	115	20–25	10,150 ± 100	12,000–11,250	11,801
61526	132	131–132	10,140 ± 110	12,150–11,250	11,717
61511	145	50–52	10,200 ± 110	12,350–11,350	11,935
61554	85	81–85	10,200 ± 110	12,350–11,350	11,780
61541*	103	99–103	10,500 ± 120	12,650–11,950	11,776
61532	50	1–2	10,600 ± 140	12,650–12,050	11,886
61529	71	1–3	10,000 ± 100	11,950–11,250	11,856
61539	91	1–5	10,200 ± 110	12,350–11,350	11,904
61551*	89	40–50	11,100 ± 100	13,150–12,750	11,946
61534	82	78–82	10,200 ± 110	12,450–11,350	11,839
62697	172	52–55	10,000 ± 150	12,050–11,150	11,627

Time Consumption and Costs

Up to 75 unknown samples can be analyzed with Speed Dating per day. The measurements require minimal user input (at least every 3 hr) and is extremely efficient compared to conventional dating techniques. Conventional AMS dating requires the subsequent processes of (a) cellulose preparation (2 days), (b) graphitization (2–5 days), and (c) measurement (1–2 days). Meanwhile, Speed Dating can yield results in a single day. We estimate the cost of Speed Dating samples to be less than one-third that of conventional AMS dating.

CONCLUSIONS

Speed Dating offers a rapid way to estimate the ^{14}C date for wood material as it is faster than conventional AMS measurements at roughly one-third the cost. Up to 75 wood samples can be analyzed within a day. The achieved measurement uncertainties were with 0.5–2% (60–160 yr), depending on the age of the wood. In this respect, Speed Dating is not an application to replace or be used in substitute for conventional high-precision measurement. Rather, Speed Dating can be used to add in an efficient way a time constraint to previously undated material to determine if the sample(s) or a site(s) warrants further investigation.

ACKNOWLEDGMENTS

The research was funded by the D-A-CH Lead-Agency agreement of the Swiss National Science Foundation (SNF) and the German Research Foundation (DFG).

REFERENCES

Brock F, Higham T, Ditchfield P, Bronk Ramsey C. 2010. Current pretreatment methods for AMS radiocarbon dating at the Oxford Radiocarbon Accelerator Unit (ORAU). *Radiocarbon* 52(1):103–12.

Bronk Ramsey C, Ditchfield P, Humm M. 2004. Using a gas ion source for radiocarbon AMS and GC-AMS. *Radiocarbon* 46(1):25–32.

Calcagnile L, Quarta G, D'Elia M. 2005. High-resolution accelerator-based mass spectrometry: precision, accuracy and background. *Applied Radiation and Isotopes* 62(4):623–9.

Cook ER, Kairiukstis LA. 2013. *Methods of Dendrochronology: Applications in the Environmental Sciences*. Dordrecht: Springer Science & Business Media.

Fahrni SM, Wacker L, Synal HA, Szidat S. 2013. Improving a gas ion source for ^{14}C AMS. *Nuclear Instruments and Methods in Physics Research B* 294(1):320–7.

Fifield LK. 1999. Accelerator mass spectrometry and its applications. *Reports on Progress in Physics* 62(8):1223–74.

Friedrich M, Remmele S, Kromer B, Hofmann J, Spurk M, Kaiser KF, Orcel C, Küppers M. 2004. The 12,460-year Hohenheim oak and pine tree-ring chronology from central Europe—a unique annual record for radiocarbon calibration and paleoenvironment reconstructions. *Radiocarbon* 46(3):1111–22.

Gaudinski JB, Dawson TE, Quideau S, Schuur EA, Roden JS, Trumbore SE, Sandquist DR, Oh SW, Wasylishen RE. 2005. Comparative analysis of cellulose preparation techniques for use with ^{13}C, ^{14}C, and ^{18}O isotopic measurements. *Analytical Chemistry* 77(22):7212–24.

Hogg AG, Hua Q, Blackwell PG, Niu M, Buck CE, Guilderson TP, Heaton TJ, Palmer JG, Reimer PJ, Reimer RW, Turney CSM, Zimmerman SRH. 2013. SHCal13 Southern Hemisphere calibration, 50,000 years cal BP. *Radicarbon* 55(4):1889–903.

Hoper ST, McCormac FG, Hogg AG, Higham TFG, Head MJ. 1998. Evaluation of wood pretreatments on oak and cedar. *Radiocarbon* 40(1):45–50.

Kaiser KF, Friedrich M, Miramont C, Kromer B, Sgier M, Schaub M, Boeren I, Remmele S, Talamo S, Guibal F, Sivan O. 2012. Challenging process to make the Lateglacial tree-ring chronologies from Europe absolute–an inventory. *Quaternary Science Reviews* 12(36):78–90.

Kieser WE, Leung K, Krestina N, Zhao XL, Litherland AE, Cornett J. 2010. Development and testing of an integrated combustion and gas ion source system for AMS. *Nuclear Instruments and Methods in Physics Research B* 268(7):784–6.

Němec M, Wacker L, Gäggeler H. 2010. Optimization of the automated graphitization system AGE-1. *Radiocarbon* 52(2–3):1380–93.

Reimer PJ, Bard E, Bayliss A, Beck JW, Blackwell PG, Bronk Ramsey C, Grootes PM, Guilderson TP, Haflidason H, Hajdas I, Hatté C, Heaton TJ, Hoffmann DL, Hogg AG, Hughen KA, Kaiser KF, Kromer B, Manning SW, Niu M, Reimer RW, Richards DA, Scott EM, Southon JR, Staff RA, Turney CSM, van der Plicht J. 2013. IntCal13 and Marine13 radiocarbon age calibration curves 0–50,000 years cal BP. *Radiocarbon* 55(4):1869–87.

Ruff M, Wacker L, Gäggeler HW, Suter M, Synal H-A, Szidat S. 2007. A gas ion source for radiocarbon measurements at 200 kV. *Radiocarbon* 49(2):307–14.

Ruff M, Fahrni S, Gäggeler HW, Hajdas I, Suter M, Synal H-A, Szidat S, Wacker L. 2010. Online radiocarbon measurements of small samples using elemental analyzer and MICADAS gas ion source. *Radiocarbon* 52(4):1645–56.

Salazar G, Zhang YL, Agrios K, Szidat S. 2015. Development of a method for fast and automatic radiocarbon measurement of aerosol samples by online coupling of an elemental analyzer with a MICADAS AMS. *Nuclear Instruments and Methods in Physics Research B* 361(1):163–7.

Synal H-A. 2013. Developments in accelerator mass spectrometry. *International Journal of Mass Spectrometry* 349(1):192–202.

Synal H-A, Stocker M, Suter M. 2007. MICADAS: a new compact radiocarbon AMS system. *Nuclear Instruments and Methods in Physics Research B* 259(1):7–13.

Vogel JS, Southon JR, Nelson DE, Brown TA. 1984. Performance of catalytically condensed carbon for use in accelerator mass-spectrometry. *Nuclear Instruments and Methods in Physics Research B* 5(2):289–93.

Wacker L, Němec M, Bourquin J. 2010a. A revolutionary graphitisation system: fully automated, compact and simple. *Nuclear Instruments and Methods in Physics Research B* 268(7):931–4.

Wacker L, Bonani G, Friedrich M, Hajdas I, Kromer B, Němec M, Ruff M, Suter M, Synal H-A, Vockenhuber C. 2010b. MICADAS: routine and high-precision radiocarbon dating. *Radiocarbon* 52(3):252–62.

Wacker L, Christl M, Synal H-A. 2010c. Bats: a new tool for AMS data reduction. *Nuclear Instruments and Methods in Physics Research B* 268(7):976–9.

Wacker L, Fahrni SM, Hajdas I, Molnar M, Synal HA, Szidat S, Zhang YL. 2013. A versatile gas interface for routine radiocarbon analysis with a gas ion source. *Nuclear Instruments and Methods in Physics Research B* 294(1):315–9.

Wacker L, Güttler D, Goll J, Hurni JP, Synal H-A, Walti N. 2014. Radiocarbon dating to a single year by means of rapid atmospheric ^{14}C changes. *Radiocarbon* 56(2):573–9.

Xu X, Trumbore SE, Zheng S, Southon JR, McDuffee KE, Luttgen M, Liu JC. 2007. Modifying a sealed tube zinc reduction method for preparation of AMS graphite targets: reducing background and attaining high precision. *Nuclear Instruments and Methods in Physics Research B* 259(1):320–9.

2.2 Consequences of Speed dating Binz trees

Speed dates of several Binz trees were used in part to confirm dendrochronology links and assign dendrochronology calendar ages by F. Reinig (Fig 2.1). The Speed Dates I measured as part of joint effort are given in appendix.

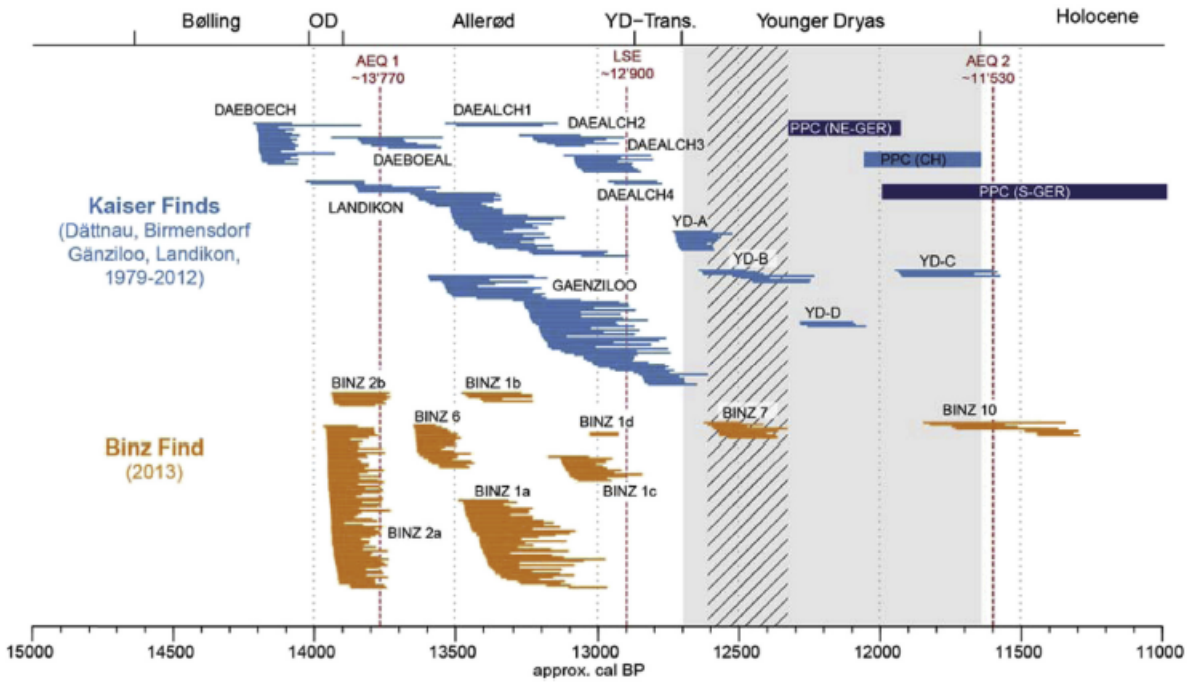

Figure 2.1: Various Binz chronologies with pre-existing Swiss chronologies, modified from Reining et al. (2018)

Surprisingly, the majority of Binz trees were either too old or too young to connect to absolute German chronology or extend Swiss floating chronologies, except Binz group 7. No dendrochronology cross-date between this group and those of Kaiser et al. (2012) were discovered by Reining et al. (2018). In lieu of this, we decided to ^{14}C date Binz group 7 and re-date Kaiser et al. (2012) chronologies to wiggling-match chronologies. To minimize uncertainties in wiggle-matching of chronologies requires high-precision ^{14}C dates.

The term 'high-precision' is used quite often with a lack of protocols available to the academic community. By and large, a quality insurance test proposed by IntCal is an intercomparison. These studies (although only a handful exists) may mention chemical methods applied to analytes but normally focus on laboratory offsets (Adolphi et al. 2013; Hogg et al. 2013).

In an effort to ensure the ^{14}C dates produced in this study were precise we implemented quality insurances from the first set measurements until the last ^{14}C date, totaling 1705. The quality protocol we are trying to introduce to academic community is presented in Chapter 3.

Chapter 3

A protocol for high precision ^{14}C dating

This chapter contains the paper accepted with revision (01/2019) that was submitted to the journal of Radiocarbon. This paper summarize the methodology we used at ETH to ensure high precision and accurate ^{14}C dates produce in this dissertation.

3.1 Quality Dating: A protocol for reproducible high precision ^{14}C dates applied to Late Glacial wood

Adam Sookdeo[1,2*], Bernd Kromer[3], Ulf Büntgen[5,6,7], Michael Friedrich[3,8], Gerd Helle[9], Daniel Nievergelt[5], Maren Pauly[9], Frederick Reinig[5,10], Kerstin Treydte[5], Hans-Arno Synal[1], Lukas Wacker[1]

[1] ETH Zurich, Laboratory of Ion Beam Physics, Zurich, Switzerland
[2] ETH-Zurich, Carbon Cycle Biogeoscience, Zürich, Switzerland
[3] Heidelberg University, Institute of Environmental Physics, Heidelberg, Germany
[4] University of Bern, Climate and Environmental Physics & Oeschger Center for Climate Change Research, Bern, Switzerland
[5] Swiss Federal Research Institute WSL, Birmensdorf, Switzerland
[6] University of Cambridge, Department of Geography, Cambridge, UK
[7] University Brno, Global Change Research Institute CAS and Masaryk, Brno, Czech Republic
[8] Hohenheim University, Institute of Botany, Stuttgart, Germany
[9] GFZ German Research Centre for Geosciences, Potsdam, Germany
[10] University Mainz, Department of Geography, Johannes Gutenberg, Germany
*Corresponding author: A. Sookdeo, Laboratory of Ion Beam Physics, ETH-Zürich, Zürich, 8093, Switzerland. (asookdeo@phys.ethz.ch)

3.1.1 Abstract

Advances in accelerator mass spectrometry have resulted in an unprecedented amount of new high-precision radiocarbon (^{14}C) -dates, some of which will redefine the international ^{14}C calibration curves (IntCal and SHCal). Often these datasets are unaccompanied by detailed quality insurances in place at the laboratory, questioning whether the ^{14}C structure is real, a result of a laboratory variation or sample-scatter. A handful of intercomparison studies attempt to root out laboratory offsets but may fail to identify sample-scatter and are often financial constrained. Here we introduce a protocol, called Quality Dating, implemented at ETH-Zürich to ensure reproducible & accurate high-precision ^{14}C-dates. The protocol highlights the importance of the continuous measurements and evaluation of blanks, standards, references and replicates. This protocol is tested on an absolutely dated German Late Glacial tree-ring chronology, part of which is intercompared with the Curt Engelhorn-Center for Archaeometry. Together with CEZA, a dataset containing 170 highly-resolved, highly-precise ^{14}C -dates supplement and restructure three decadal dates spanning 280 cal. years in IntCal.

3.1.2 INTRODUCTION

Radiocarbon (^{14}C) dating can be used to determine the age of an object or for reconstruction of past atmospheric and oceanic ^{14}C concentrations. While a calendrical age of a ^{14}C -date(s) is determined through calibration (IntCal, SHCal), reconstructed concentrations are derived from a variety of archives. These ^{14}C-archives, in turn, form the backbone of IntCal (Reimer et al 2013a) and SHCal (Hogg et al. 2013a); the touchstone for which are tree-ring chronologies. Tree-rings, can be dendrochronologically dated with absolute certainty from 1950 AD (considered present) to $\sim$ 12k Before Present (BP; Friedrich et al. 2004) and are direct measure of atmospheric ^{14}C (Becker 1993; Kromer and Becker 1993; Stuiver and Pearson 1993; Friedrich et al. 1999; Reimer et al. 2013b). Single tree-rings serve as means to reconstruction atmospheric ^{14}C with annual resolution. Annual ^{14}C -dating of trees is possible thanks to the relatively small sample-size ($\geq$ 10mg) required for an Accelerator Mass Spectrometer (AMS) date. New annual or high resolution AMS ^{14}C -dates help to establish 'wiggles' and identify rapid increases in atmospheric in IntCal and SHCal.

The origin of a 'wiggle' can be the result of a production or concentration change (Stuiver and Braziunas 1993), with rapid increases associated to solar forcing (Miyake et al. 2012; Miyake et al. 2013; Büntgen et al 2018). Production changes to ^{14}C are inversely related to solar activity and are correlated to changes in the geomagnetic field. Rapid increases (year-to-year change) have been discovered twice in tree-rings (Miyake et al. 2012; Miyake et al. 2013; Büntgen et al 2018) that are speculated to be of solar flare (Usoskin et al. 2013), which can negatively impact astronauts and the international space station (Xapsos et al). In addition, tightly calendrical constrained, well-defined 'wiggles' and solar flares will help reduce the uncertainty of a ^{14}C -date(s) calibration to IntCal and SHCal. However, before datasets containing such features are incorporated into IntCal or SHCal , they must be tested for their consistency and reproducibility. (Reimer et al. 2013b).

Intercomparsions focus on the reproducibility of a set of unknowns and fruitfully determine any potential laboratory offsets (Adolphi et al. 2013; Hogg et al. 2013b). These studies are often expensive and time consuming, thus not always feasible for every ^{14}C laboratory nor every ^{14}C project. To identify internal issue many laboratories have quality insurances in place but are not published, making it difficult to ascertain whether the ^{14}C structure in a dataset is real, a result of a laboratory variation or sample-scatter.

Here we present ETH's protocol to ensure reliable, reproducible high-precision ^{14}C dates: "Quality Dating." As a case study, we apply the Quality Dating protocol to ^{14}C dates on Late Glacial wood from 12.16-11.88 kBP, where only three decadal dates exits in IntCal13 (Reimer et al. 2013a) and intercompared our results with the Curt-Engelhorn-Zentrum for Archaeometry (CEZA).

3.1.3 METHOD

Dendrochronology

Tree-Ring Width (TRW) measurements were from at least two radii of each sample using a LINTAB measuring device with a precision of 0.01 mm and the software program TSAPWin (Rinn, 1996). The TRW measurements were visually and statistically cross-dated using t-values (tBP) and Gleichläufigkeit (Glk) indices (Baillie and Pilcher, 1973) in TSAPWin. Chronologies were established and checked with Cofecha (Holmes, 1983). Individual trees (BREI0232, COTT0418) were selected by wood quality, length and positioning within the developed chronologies (Friedrich et al. 2004) for ^{14}C dating. Whole tree-rings were sampled with a mixture of biennial to septennial dependent on the width of single-rings. The dendrochronological linkages from Preboreal Pine Chronology (PPC)-Cottbus (Cott) and PPC-Breitenthal (BREI) can be seen in figure 3.1.

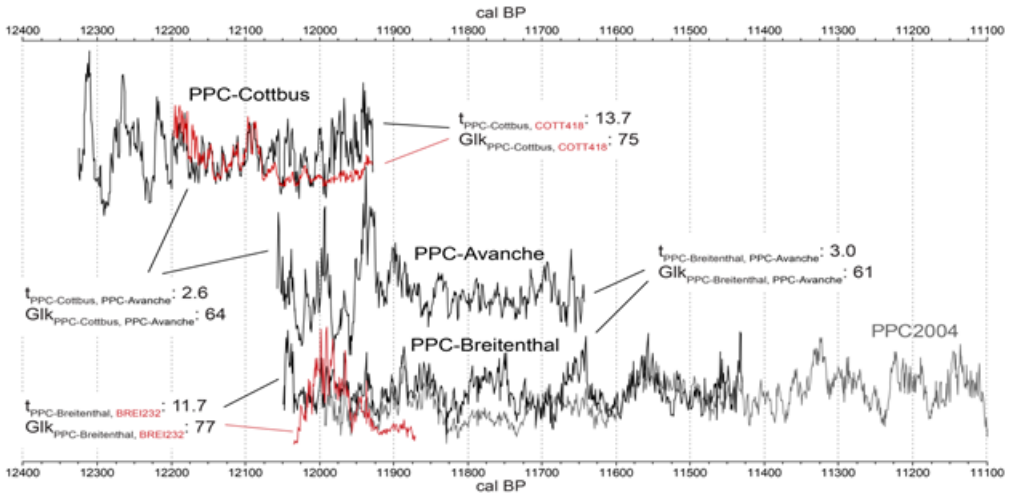

Figure 3.1: The t-value and Glk values for the dendrochronological linkage of PPC chronologies around 12 kBP are given.

Sample Preparation and Measurements

A chemical blank, Phthalic Anhydride (PhA, SigmaAldrich, PN-320064-500 g), was used to detect contamination from the graphitization process and the MIni CArbon DAting System (MICADAS). Fossilized wood "Braunkohle" (BK, also known as brown coal is lignite from Reichwalde, Gemany) and kauri wood (KB, MIS 7, New Zealand) were used as process blanks. Standards were Oxalic acid II (OXII, NIST SRM 4990C) and Oxalic acid I (OXI, SRM 4990B). The reference, a 10-year block of kauri wood (TK121) is from the Younger Dryas, a period of time representative of the samples introduced in this study, dated to 10968 ±21 ^{14}C yrs (1-σ; Hogg et al. 2013b). The samples BREI0232 and COTT418 are pines (*Pinus sylvestris L*) from the PPC. These pines were part of a larger discovery in Breitenthal and Cottbus, Germany (Friedrich et al. 2004).

Process blanks, reference material and samples were chemically treated to extract cellulose. Cellulose is a component of wood that has remained unchanged over time and is necessary for an accurate ^{14}C -date (Hoper et al. 1998; Brock et al. 2010; Sookdeo et al 2017). Cellulose was extracted in batches of 56 (2 TK121, 2 BK, 2 KB and 50 samples) using a modified base-acid-base-acid-bleaching method outlined by Němec et al. (2010). The modified method involved an over the weekend base step at 60°C and the second acid step was a wash, which resulted in whiter cellulose than the method outlined by Němec et al. (2010). The extracted cellulose was placed in a freeze dryer overnight. For each of the standards, blanks and samples 1mg of carbon were placed inside aluminum capsules (4 × 4 × 11 mm, Elementar) and closed. These capsules were placed into an Elemental Analyzer (EA, Vario MICROcube, Elementar) sample holder.

Samples, standards and blanks were dropped into the heated chamber of an EA one at a time, where oxygen gas was fed in for 50 sec to facilitate the combustion of carbon to carbon dioxide, which was captured in a zeolite trap. The estimated cross-contamination between capsules in an EA is less than 0.6‰ (Wacker et al. 2010a). Nevertheless, to limit cross-contamination between blanks, standards and samples, two pre-conditioning blanks, standards or samples were run to deterge the system before sampling. The pre-conditioning materials were combusted in the EA, loaded onto the trap and then discarded. The graphitized materials were pressed into aluminum cathodes (Ionplus), organized and placed in the sample holder of a MICADAS (Ionplus), known as a magazine.

One magazine contained seven standards, either four OXI or three OXII or vice versa, one PhA, four process-blank (two BK, two KB), two TK121 and 25 samples. Samples were bracketed by standards to detect any potential time-dependent variation. Magazines were measured on a MICADAS at the Laboratory of Ion Beam Physics, ETH-Zürich (Synal et al. 2007; Wacker et

al. 2010b). Measurements times varied between two or three days or until the uncertainty on a samples' ^{14}C -age were approx. 21 years (200 000 ^{14}C counts). Data reduction was carried out with the BATS program as described by Wacker et al. (2010c), in compliance with data processing for AMS measurements.

As an opportunity to further test the methodology used at ETH, 72 identical samples were sent to, prepared at and the ^{14}C age determined at CEZA on their MICADAS. These samples are given labelled identifier 'MAMS.' The samples, process blanks and reference materials measured at CEZA were treated identically to extract cellulose. The applied cellulose method was a base (overnight; 4% NaOH)-acid (30min; 4% HCl)-base (30min; 4% NaOH)-bleaching (at least 60min; pH 3 $NaClO_2$) with all steps undertaken at 60°C. The bleaching was repeated until material turned white after which the material was washed thoroughly with deionized water. Samples were dried in an oven at 80°C and approx. 1mg of carbon was placed in aluminum capsules (Elementar) and combusted in an EA (Vario MIRCOcube, Elementar). Samples were either graphitized on an in-house system or an AGE-3 (Ionplus). The custom graphitization system used a liquid-nitrogen-cooled trap in contrast to the zeolite trap of an AGE-3. Graphite was compressed into aluminum cathodes (Ionplus). In addition, to the 72 samples mentioned above, 23 and three samples from the PPC were measured at ETH-Zürich and CEZA, respectively.

3.1.4 RESULTS AND DISCUSSION

Blanks

The distribution of 33 combustion blanks (PhA), and 164 process blanks (BK and KB) are compared in figure 3.2. While a PhA blank is typically indistinguishable from a process blank, the mean $F^{14}C$ values differ ($p \ll 0.05$) with 0.00132 ±0.00005 (1-σ; 53.3k ^{14}C yrs) compared to 0.00164 ± 0.00003 $F^{14}C$ (1-σ; 51.7k ^{14}C yrs), respectively. The more degrade fossilized wood (BK) is indistinguishable from the better preserved Kauri wood (KB), though its cellulose yield was reduced by approx. 30%.

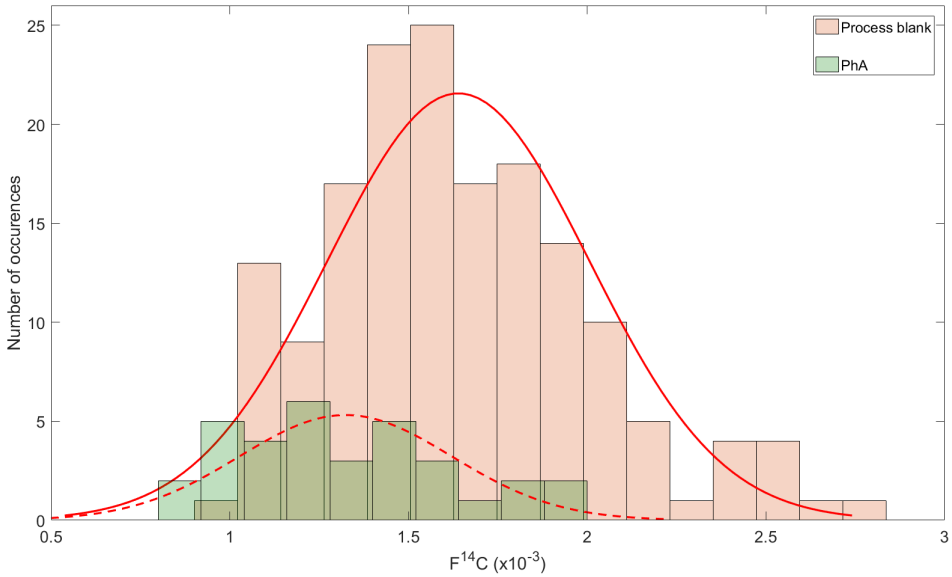

Figure 3.2: Distributions of F14C for 166 process blanks (Kauri and Brown coal wood, red) and 33 chemical blank (PhA, green) measured at ETH-Zürich over 2 years are fitted with normal distributions (red lines).

The difference between the combustion and process blanks arises as the combustion blank is

not subjected to the cellulose extraction treatment. The role of the PhA is to detect any potential contamination during graphitization and target preparation, but is not used for data reduction as it tends to underestimate ^{14}C introduced during sample processing. Rather, the process blank, for which we observed on average as larger $F^{14}C$ (figure 3.2), are used for background correction with a $F^{14}C$ of 0.0003 was used for the error propagation.

To appropriately estimate ^{14}C background and variability, we suggest having at least four process blanks per 25 samples – the first step of our protocol.

Standards

Standards of OXII, OXI or another compound with a known ^{14}C concentration are used to determine the $F^{14}C$ value for a sample. The linearity of standard normalization in between months and years of measurements is rarely reported. Over the course of two years, a mixture of seven OXII and OXI per magazine measured at ETH is extremely consistent (Wacker et al. in press). The mean $F^{14}C$ for 77 OXII normalized to OXI was 1.340119 ±0.000184 (1-σ), in good agreement with the consensus value of 1.34066 ±0.00043 (1-σ; Mann 1983; Stuiver 1983). The strong reproducibility of our standards was not affected by different cation ($^{12}C^+$ and $^{13}C^+$) currents measured between magazines (Wacker et al. in press). In addition, the uncertainties of the individual standards, as well as the samples, have a relative 1‰ added for the reproducibility of the analysis, including preparation. The additional uncertainty was estimated from the reproduction of the reference material and the intercomparison with Mannheim. While a drawback of multiple standard can be time (if more are required) and cost (if a new standards have to be order), the added benefit, leads us to the second step of our protocol, always measure various standards in replicates.

Reference material

The results of reference material provided crucial information on whether sample preparations along with ^{14}C measurements are reproducible. TK121, a 10-year block of wood from the towai chronology (Hogg et al. 2016) serves as a reference for this study, as it has 1) been ^{14}C-dated by five different laboratories-with a consensus age of 10968 ±21 ^{14}C yrs (1-σ; Hogg et al. 2013b), 2) no large year-to-year variations (Hogg et al. 2016) and 3) a representative ^{14}C age and composition to the samples presented in this study. The TK121 measure over the course of two years at ETH is given in figure 3.3.

The mean ^{14}C age was determined to be 10 954 ±2 (1-σ) with a variability of ±20. A normalized χ^2_{red}-test performed on TK121 yield a value of 0.72. A significance level (α) of 0.05 for a dataset of this size, is 0.76, indicating our uncertainties are precise with a tendency to be conservatively overestimated. However, this could be the result of the well preserved nature of kauri wood, and not justifiable to reduce our ^{14}C uncertainties for other samples. Therefore, the uncertainties quoted here and on German Late Glacial wood are not reduced. Rather these uncertainties include contributions from the variability of the background (±0.00003 in $F^{14}C$), standards (±0.000184 in $F^{14}C$), counting statistics (approx. ‰) and 1‰ for the reproducibility of the analysis. The uncertainties for 81 TK121 are all within the 1-σ) of Hogg et al. (2013b). Hence, the third step of our protocol is to measure two references per 25 unknowns.

Intercomparison between CEZA and ETH-Zürich on late-glacial wood

Intercomparisons unlike internal references or duplicates can identify laboratory offsets (Adolphi et al. 2013; Hogg et al. 2013b). Late-Glacial tree-rings measured at ETH generated structure (see Extension of the PPC) not visible in IntCal13. More so, this structure is reflected in the 72 identical samples chemically extracted, graphitized and ^{14}C dated at CEZA (see methods), which are in excellent agreement in a distribution of differences, figure 3.4.. The mean of this distribution was determined to be -3 ±4 ^{14}C yrs (1-σ) with a χ^2_{red} of 1.06.

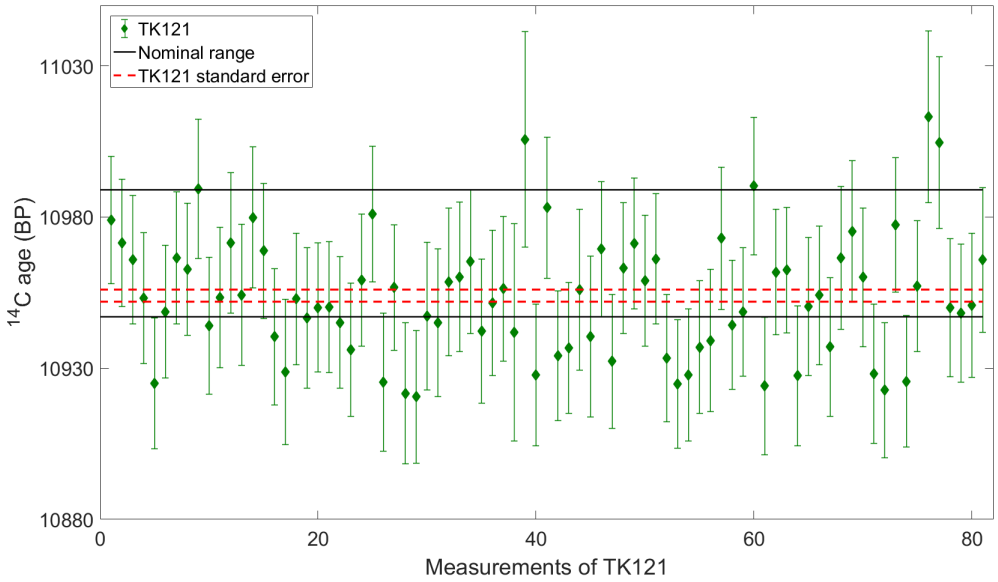

Figure 3.3: ^{14}C age for 81 reference samples (TK121, green) measured at ETH-Zürich with their mean value (1-σ limits, red lines) and the nominal value (black, see methods).

This χ^2_{red} value is an indication that the calculated uncertainties in both laboratories were appropriately estimated, which is in slight contrast to our findings based on the references. While in principle the increased χ^2_{red}- of the replications compared to the reference material could be explained by a possible underestimation of uncertainties by CEZA, we think the increase χ^2_{red} is more likely due to the different state of preservation of the wood samples. Thus the excellent agreement between CEZA and ETH validate the Quality Dating protocol implemented on Late Glacial wood. It is not realistic for all laboratories to be able to have the time and afford the work necessary for an intercomparison. Therefore, the fourth step of our protocol is to either have an intercomparison (ideally) or measure at least every fifth unknown in duplicates.

Extension of the PPC

The oldest part of world's longest absolute chronology, the PPC, has three decadal ^{14}C-dates covering a period between 12 160 to 11 880 cal BP in IntCal13 (Reimer et al. 2013a). Together with the CEZA we introduce 170 high-precision ^{14}C -dates that fill this period with high temporal resolution and structure, 3.4b. The ^{14}C record starts with a plateau at 12.16 cal kBP lasting over 200 cal. years - unprecedented in IntCal13 (Reimer et al. 2013a) with less variation than the Hallstatt plateau. This plateau has two small visible ^{14}C wiggles, before it is truncated by a 110 ^{14}C yrs (13‰ in Δ^{14}C) change within 40 calendar years, not evident in the decadal measurements within IntCal13. This extension of the PPC will be submitted to the next iteration of Intcal. The structure introduced for this period is neither a result of large sample scatter nor laboratory offsets because of the excellent agreement with CEZA.

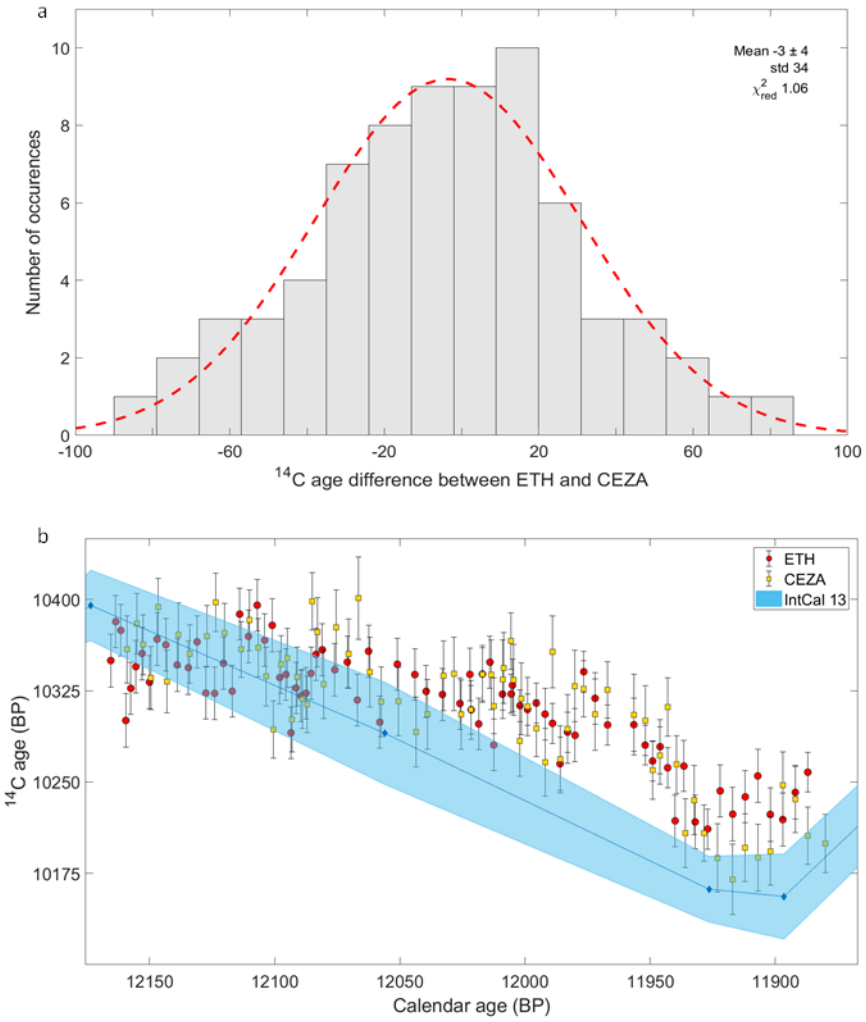

Figure 3.4: a) Histogram of ^{14}C age differences for the same samples prepared and measured separately at ETH-Zürich and CEZA (grey), overlaid with a normal curve (red). b) ^{14}C ages for dendrochronological dated tree-rings of the PPC measured at ETH-Zürich (red) and CEZA (yellow) are compared with the latest calibration curve IntCal13 curve (blue).

3.1.5 CONCLUSION

Advances in AMS measurements have led to a rush of high precision, timely resolved ^{14}C-dates but paucity exists on discussions of quality insurances. The here presented Quality Dating protocol at ETH ensures reproducible, accurate and precise ^{14}C -dates by:

- Having samples accompanied with process blanks rather than combustible blanks
- Running multiple standards of varying ^{14}C concentrations
- Continual measurements of references that is comparable in age and composition to the sample
- Replication of measurements, ideally by another laboratory

This confirms proper background correction, robust standard normalization and reproducible results. By no means is this the only way to ensure high-precision ^{14}C -dates and we hope that other ^{14}C laboratories will published their own protocols in the near future.

3.1.6 Acknowledgments

The research was funded by the D-A-CH Lead-Agency agreement of the Swiss National Science Foundation (SNF) and the German Research Foundation (DFG, Kr726/10-1).

3.1.7 References

^{14}C dating of wood samples at Lund University and ETH-Zurich AMS facilities: extraction, graphitization, and measurement. Radiocarbon 55(2):391-400.
Baillie MG, Pilcher JR. 1973. A simple crossdating program for tree-ring research. Tree-ring bulletin.
Becker B. 1993. An 11,000-year German oak and pine dendrochronology for radiocarbon calibration. Radiocarbon 35(1):201-13.
Brock F, Higham T, Ditchfield P, Bronk Ramsey C. 2010. Current pretreatment methods for AMS radiocarbon dating at the Oxford Radiocarbon Accelerator Unit (ORAU). Radiocarbon 52(1):103–12.
Buntgen, U., Wacker, L., Galvan, J.D., Arnold, S., Arseneault, D., Baillie, M., Beer, J., Bernabei, M., Bleicher, N., Boswijk, G., Brauning, A., Carrer, M., Ljungqvist, F.C., Cherubini, P., Christl, M., Christie, D.A., Clark, P.W., Cook, E.R., D'Arrigo, R., Davi, N., Eggertsson, O., Esper, J., Fowler, A.M., Gedalof, Z., Gennaretti, F., Griessinger, J., Grissino-Mayer, H., Grudd, H., Gunnarson, B.E., Hantemirov, R., Herzig, F., Hessl, A., Heussner, K.U., Jull, A.J.T., Kukarskih, V., Kirdyanov, A., Kolar, T., Krusic, P.J., Kyncl, T., Lara, A., LeQuesne, C., Linderholm, H.W., Loader, N.J., Luckman, B., Miyake, F., Myglan, V.S., Nicolussi, K., Oppenheimer, C., Palmer, J., Panyushkina, I., Pederson, N., Rybnicek, M., Schweingruber, F.H., Seim, A., Sigl, M., Churakova Sidorova, O., Speer, J.H., Synal, H.A., Tegel, W., Treydte, K., Villalba, R., Wiles, G., Wilson, R., Winship, L.J., Wunder, J., Yang, B., Young, G.H.F., 2018. Tree rings reveal globally coherent signature of cosmogenic radiocarbon events in 774 and 993 CE. Nat Commun 9, 3605-11.
Friedrich M, Kromer B, Spurk M, Hofmann J, Kaiser KF. 1999 Paleo-environment and radiocarbon calibration as derived from Lateglacial/Early Holocene tree-ring chronologies. Quaternary International 61(1):27-39.
Friedrich M, Remmele S, Kromer B, Hofmann J, Spurk M, Kaiser KF, Orcel C, Küppers M. 2004. The 12,460-year Hohenheim oak and pine tree-ring chronology from central Europe—a unique annual record for radiocarbon calibration and paleoenvironment reconstructions. Radiocarbon 46(3):1111-22.
Hogg A, Turney C, Palmer J, Southon J, Kromer B, Bronk Ramsey C, Boswijk G, Fenwick P, Noronha A, Staff R, Friedrich M. 2013. The New Zealand kauri (Agathis australis) research project: a radiocarbon dating intercomparison of Younger Dryas wood and implications for IntCal13. Radiocarbon 55(4):2035–48.
Hogg A, Southon J, Turney C, Palmer J, Ramsey CB, Fenwick P, Boswijk G, Büntgen U, Friedrich M, Helle G, Hughen K. 2016. Decadally resolved lateglacial radiocarbon evidence from New Zealand kauri. Radiocarbon 58(4):709-33.
Holmes RL. 1983. Program COFECHA user's manual. Laboratory of Tree-Ring Research, The University of Arizona, Tucson.
Hoper ST, McCormac FG, Hogg AG, Higham TFG, Head MJ. 1998. Evaluation of wood pretreatments on oak and cedar. Radiocarbon 40(1):45–50.
Hua Q, Barbetti M, Fink D, Kaiser KF, Friedrich M, Kromer B, Levchenko VA, Zoppi U, Smith AM, Bertuch F. 2009. Atmospheric ^{14}C variations derived from tree rings during the early Younger Dryas. Quaternary Science Reviews 28(25):2982-90.
Kromer B, Becker B. 1993. German oak and pine ^{14}C calibration, 7200–9439 BC. Radiocarbon 35(1):125-35.
Mann WB. 1983. An International Reference Material for Radiocarbon Dating. Radiocarbon, 25 519-527.
Miyake, F., Nagaya, K., Masuda, K., Nakamura, T., 2012. A signature of cosmic-ray increase in AD 774–775 from tree rings in Japan. Nature 486, 240-5.
Miyake, F., Masuda, K., Nakamura, T., 2013. Another rapid event in the carbon-14 content of tree rings. Nature communications 4, 1748-51.
Němec M, Wacker L, Gäggeler H. 2010. Optimization of the automated graphitization system

AGE-1. Radiocarbon 52(2–3):1380–93.
Reimer PJ, Baillie MGL, Bard E, Bayliss A, Beck JW, Blackwell PG, Bronk Ramsey C, Buck CE, Burr GS, Edwards RL, Friedrich M, Grootes PM, Guilderson TP, Hajdas I, Heaton TJ, Hogg AG, Hughen KA, Kaiser KF, Kromer B, McCormac FG, Manning SW, Niu M, Reimer RW, Richards DA, Southon JR, Talamo S, Turney CSM, van der Plicht J, Weyhenmeyer CE. 2009. IntCal09 and Marine09 radiocarbon age calibration curves 0–50,000 years cal BP. Radiocarbon 51(4):1111–50.
Reimer PJ, Bard E, Bayliss A, Beck JW, Blackwell PG, Bronk Ramsey C, Grootes PM, Guilderson TP, Haflidason H, Hajdas I, Hatté C, Heaton TJ, Hoffmann DL, Hogg AG, Hughen KA, Kaiser KF, Kromer B, Manning SW, Niu M, Reimer RW, Richards DA, Scott EM, Southon JR, Staff RA, Turney CSM, van der Plicht J. 2013a. IntCal13 and Marine13 radiocarbon age calibration curves 0–50,000 years cal BP. Radiocarbon 55(4):1869–87.
Reimer PJ, Bard E, Bayliss A, Beck JW, Blackwell PG, Ramsey CB, Brown DM, Buck CE, Edwards RL, Friedrich M, Grootes PM, Guilderson TP, Haflidason H, Hajdas I, Hatté C, Heaton TJ, Hogg AG, Hughen KA, Kaiser KF, Kromer B, Manning SW, Niu M, Reimer RW, Richards DA, Scott EM, Southon JR, Turney CSM, van der Plicht J. 2013b. Selection and treatment of data for radiocarbon calibration: an update to the International Calibration (IntCal) criteria. Radiocarbon 55(4):1923-45.
Rinn F. 1996. Tsap V 3.6 Reference manual: computer program for tree-ring analysis and presentation. Rinntech, Heidelberg.
Sookdeo, A., Wacker, L., Fahrni, S., McIntyre, C.P., Friedrich, M., Reinig, F., Nievergelt, D., Tegel, W., Kromer, B., Büntgen, U., 2017. Speed dating: a rapid way to determine the radiocarbon age of wood by EA-AMS. Radiocarbon 59, 933-939.
Stuiver M. 1983. International Agreements and the Use of the New Oxalic-Acid Standard. Radiocarbon 25 793-795.
Stuiver M, Pearson GW. 1993. High-precision bidecadal calibration of the radiocarbon time scale, AD 1950–500 BC and 2500–6000 BC. Radiocarbon 35(1):1-23.
Stuiver, M., Braziunas, T.F., 1993. Sun, ocean, climate and atmospheric $^{14}CO_2$: an evaluation of causal and spectral relationships. The Holocene 3, 289-305.
Synal H-A, Stocker M, Suter M. 2007. MICADAS: a new compact radiocarbon AMS system. Nuclear Instruments and Methods in Physics Research B 259(1):7–13.
Usoskin, I., Kromer, B., Ludlow, F., Beer, J., Friedrich, M., Kovaltsov, G., Solanki, S., Wacker, L., 2013. The AD775 cosmic event revisited: the Sun is to blame. Astronomy & Astrophysics 552, L3.
Wacker L, Němec M, Bourquin J. 2010a. A revolutionary graphitisation system: fully automated, compact and simple. Nuclear Instruments and Methods in Physics Research B 268(7):931–4.
Wacker L, Bonani G, Friedrich M, Hajdas I, Kromer B, Němec M, Ruff M, Suter M, Synal H-A, Vockenhuber C. 2010b. MICADAS: routine and high-precision radiocarbon dating. Radiocarbon 52(3):252–62.
Wacker L, Christl M, Synal H-A. 2010c. Bats: a new tool for AMS data reduction. Nuclear Instruments and Methods in Physics Research B 268(7):976–9.
Wacker L, Bollhalder S, Sookdeo A, Synal H-A. submitted. Re-evaluation of the New Oxalic Acid Standard with AMS. Nuclear Instruments and Methods in Physics Research B.
Xapsos, M.A., Barth, J.L., Stassinopoulos, E.G., Messenger, S.R., Walters, R.J., Summers, G.P., Burke, E.A., 2000. Characterizing solar proton energy spectra for radiation effects applications. IEEE Transactions on Nuclear Science 47, 2218-2223.

Chapter 4

Redefining ^{14}C 'wiggles' and their origins before and during a cooling event

Quality dating was implemented for all 1705 samples produced at ETH during this dissertation. This chapter reveals the extension of the absolute German chronology through wiggle-matching to Swiss trees that confirmed tentative dendrochronology cross-dated performed by F. Reinig. Moreover,additional cross-dates performed by F. Reinig are in agreement with wiggle-matches of trees within Swiss chronologies. In light of dendrochronology cross-date between the absolute chronology and Swiss floating chronologies, Swiss chronologies were wiggle-matched to a New Zealand towai chronology (Hogg et al., 2016). The increased replication and synchronization of dendrochronologies enables an investigation of solar forcing in the YD. This paper it titled: 'There goes the Sun: Reconstructing atmospheric ^{14}C reveals prolonged solar minimum in the Younger Dryas' is presented as it was submitted to Nature Geoscience.

4.1 There goes the Sun: Reconstructing atmospheric ^{14}C reveals prolonged solar minimum in the Younger Dryas

Adam Sookdeo[1,2*], Bernd Kromer[3], Florian Adolphi[4], Jürg Beer[5], Ulf Büntgen[6,7,8], Michael Friedrich [3,9], Giulia Guidobaldi[1], Gerd Helle[10], Alan Hogg[11], Raimund Muscheler[12], Daniel Nievergelt[6], Jonathan Palmer[13], Maren Pauly[10], Frederick Reinig[6,14] Willy Tegel[15], Kerstin Treydte[6], Chris Turney[13] Hans-Arno Synal[1], Lukas Wacker[1]

[1] ETH Zurich, Laboratory of Ion Beam Physics, Zurich, Switzerland

[2] ETH-Zurich, Carbon Cycle Biogeoscience, Zürich, Switzerland

[3] Heidelberg University, Institute of Environmental Physics, Heidelberg, Germany

[4] University of Bern, Climate and Environmental Physics & Oeschger Center for Climate Change Research, Bern, Switzerland

[5] Swiss Federal Institute of Aquatic Science and Technology EAWAG, Zürich, Switzerland

[6] Swiss Federal Research Institute WSL, Birmensdorf, Switzerland

[7] University of Cambridge, Department of Geography, Cambridge, UK

[8] University Brno, Global Change Research Institute CAS and Masaryk, Brno, Czech Republic

[9] Hohenheim University, Institute of Botany, Stuttgart, Germany

[10] GFZ German Research Centre for Geosciences, Potsdam, Germany

[11] University of Waikato, Waikato Radiocarbon Dating Laboratory, Hamilton, New Zealand

[12] Lund University, Department of Geology-Quaternary Sciences, Lund, Sweden

[13] University of New South Wales, School of Biological, Earth and Environmental Sciences, Sydney, Australia

[14] University Mainz, Department of Geography, Johannes Gutenberg, Germany

[15] Albert-Ludwigs University of Freiburg, Chair of Forest Growth and Dendroecology, Freiburg, Germany

*Corresponding author: A. Sookdeo, Laboratory of Ion Beam Physics, ETH-Zürich, Zürich, 8093, Switzerland. (asookdeo@phys.ethz.ch)

Abstract

The Younger Dryas (YD) is marked by an abrupt return to near glacial-like conditions, ending the conversion to a warmer, interglacial climate. The radiocarbon (^{14}C) record for this period is composed of an absolutely dated (ending in 1950 AD) tree-ring chronology -the 'golden standard' for ^{14}C calibration. Efforts to extend the absolutely dated chronology further into the YD have proven frivolously due weak tree-ring overlap and low ^{14}C replication. Here we introduce the principal density of high-precision annual tree-ring ^{14}C-dates (n =1610) that in part extend the absolute ^{14}C record. This extension anchors within ±6 cal yr (2-σ) a well replicated floating New Zealand chronology and in-turn the remainder of our chronologies within ±8 cal yr (2-σ). ^{14}C production estimates shows a 40% increase in the YD that occurs within a century, which is greater than any continuous rise in the Holocene. The duration of this steep rise is caused by reduced solar activity that is potentially larger than previous estimates. This work will help align the sequence of climatic events in the YD and subsequently provide a framework for probable outcomes of solar forcing coupled to anthropogenic induced changes.

MAIN

The Earth has undergone several large climatic shifts, the most recent of which (excluding global warming) is the Younger Dryas (YD), starting near 12.9 cal kBP (before 1950 AD)[1]. The YD is denoted by a rapid cooling event that occurred faster than those induced by the movement of mass ice sheets, which are called 'Henrich' events (ref 2 and references therein). Input of fresh water from Henrich events reduced the strength of the Atlantic meridional overturning circulation, leading to a general cooling[3]. Unlike, Henrich events ice-rafted debris in the YD is limited[4, 5] and shutdown of the Atlantic meridional overturning circulation was not as prominent[6, 7]. Hence, other theories suggest that YD event was not solely caused by changes to ocean circulation and instead occurred through a combination of reduced solar forcing and altered atmospheric circulation[8, 9, 10]. These changes could have occurred through either natural processes or a comet impact[11] for which the timing is debatable[12]. Timing of natural processes such as altered atmospheric circulation, temperature changes in Europe and solar variability relay on accurate and precise radiocarbon (^{14}C) calibration.

The 'golden standard' for ^{14}C calibration are tree-rings as they 1) commonly form annually incorporating atmospheric ^{14}C for that year and 2) can be cross-matched from tree-to-tree creating dendrochronologies. Dendrochronologies are considered to be absolutely dated if the record ends in 1950 AD, otherwise they are considered 'floating' in time. The most extensive absolutely dated dendrochronology is the German Preboreal Pine tree-ring Chronology (PPC) (ref 13 and references therein). The PPC start date remains at 12 325 cal BP despite attempts to extend the record further back due to weak dendrochronological links[13] and ^{14}C overlap[14]. Tree-ring dates younger than 12 325 cal BP are predominantly from German and Swiss floating dendrochronologies[15]. ^{14}C-dates made on the absolute and floating dendrochronologies are mostly decadal blocks with low temporal resolution[13, 15] -the exception being high-precision ^{14}C-dates on the PPC between 12 160- 11 880 cal BP (Sookdeo et al. submitted). The decadal dates of floating ^{14}C records have been repositioned calendrically over the years, with matches to marine records[15], dendrochronologies from the Southern Hemisphere[16] and the common cosmogenic production signal of ^{10}Be in ice-cores[17, 18]. The most recent attempt to position

Swiss and German dendrochronologies used wiggle-matching against an extensively replicated and continuously decadally ^{14}C-dated floating New Zealand dendrochronology, named "towai"[14, 19]. The calendrical placement of the towai relied on 18 dates wiggle-matched to less precise dates from the PPC resulting in a calendrical uncertainty of ±14 years (2-σ). In the following we present the highest density of annual ^{14}C-dates (n= 1610) made on Swiss trees, which redefines and synchronizes placements of dendrochronologies to investigate solar activity during the YD.

RECONSTRUCTING ATMOSHPHERIC RADIOCARBON

The oldest of the^{14}C-dates introduced here are positioned calendrically through a combination of wiggle-matching (see supplementary table) and tentative dendrochronology dates to the PPC (Reining et al. submitted). The extended PPC increases the number of ^{14}C measurements by a factor of six and allows for unmatched precision and accurate wiggle-matching of the towai, which is shifted ten years younger than its current placement with an improved uncertainty of six years (2-σ), within the 95% CI previous placement[14], Fig. 1. The new placement of the towai anchors two Swiss floating dendrochronologies, ZHYD1 (formerly YD-B) and SWILM.

The ZHYD-1 is now a factor of four times more resolved and repositioned by seven decades (±8 cal yr, 2-σ) compared to 2013 addition of the international calibration curve (IntCal13)[20] and is within the 95% CI of Hogg *et al.*[14] placement. In addition, the ZHYD1 shows larger amplitudes changes than original decadal ^{14}C-dates[15] submitted to IntCal13 that are more in line with towai but offer improved constrains on fast events occurring within the decades, Fig.1. The number of ^{14}C- dates derived on the SWILM chronology has increased by factor of three and has be calendrical repositioned by four decades (±8 cal yr, 2-σ) compared to IntCal13 and is outside the 95% CI of Hogg *et al*.[14] placement. This discrepancy is due to the low replication and resolution of ^{14}C on the SWILM when it was first wiggle-match to the towai accompanied by a sharp 40‰ in Δ^{14}C rise carrying more weight when trying to minimizing the difference. Our new SWILM record is well replicated both before and after the steep rise in ^{14}C, enabling placement to the towai that is without equal. The new placement of the SWILM was used to wiggle the French barbier chronology[21], which was originally "visually tuned" to the towai, Fig. 1.

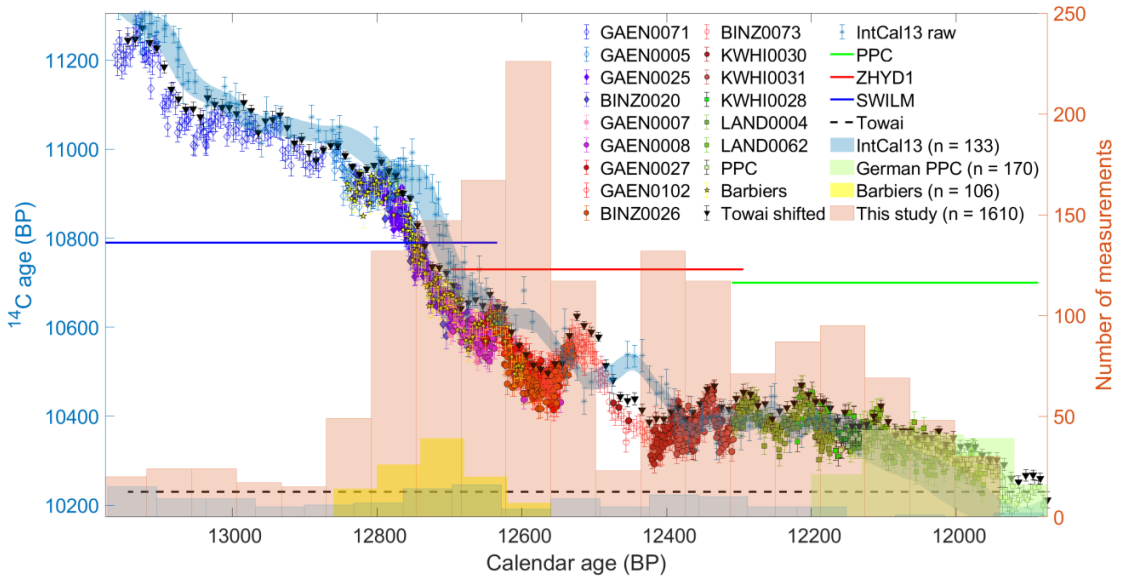

Figure 1 Terrestrial ^{14}C records in the YD. Individual trees measured for this study are given in the legend with their respective dendrochronology denoted as symbols: PPC (green squares), ZHYD1 (red circles), and SWILM (blue diamonds). The towai chronology (black inverted arrow; Hogg et al., 2016) is shifted bases on a wiggle-match to the PPC. In turn, the shifted towai was used to position ZHYD1 and SWILM. The barbiers (yellow pentagrams; Capano et al., 2017) positioned against the SWILM. Tree-ring data from IntCal13 (Reimer et al., 2013a) are plotted (blue *) and the smooth random walk curve (blue fill). ^{14}C calendar ranges are given for the PPC (green line), ZHYD1 (red line), SWILM (blue line) and towai (black line). The number of ^{14}C measured as with bin sizes of 65 cal years are given for IntCal13 (blue; Reimer et al, 2013) German trees of the PPC (green; Sookdeo et al., in press), Barbier (yellow; Capno et al. 2018;) and this study (red).

PRODUCTION

The structural changes in ^{14}C during the YD could have resulted from production variations that are driven by solar and geomagnetic forcing, with amplitudes modulated by reduced deep ocean ventilation[22, 23]. Solar forcing, was proposed to behind upwards of 80‰ changes in $\Delta^{14}C$ observed in marine sediments and corals in YD[8]. However, bi-decadal ^{14}C measurements on two Polish lake sediments[24] along with floating tree-ring measurements[15] showed smaller amplitudes of 40% in $\Delta^{14}C$ that were either associated with natural variations or ocean driven. In addition, by matching floating tree-ring chronologies to common cosmogenic production signal of ^{10}Be derived from ice-core, GISP2 revealed an offset in amplitudes that were postulated to be a result of a 30% reduced deep ventilation[17]. Later measurements of ^{10}Be on ice-core, GRIP showed inconsistences with measurements on GISP2 that have yet to be reconciled[25]. It is difficult to decide, which ice-core record is accurate when comparing common production signatures to the new ^{14}C record as perfect agreement between ^{10}Be flux and ^{14}C cannot be expected[17]. Nevertheless, with the new ^{14}C record we can estimate production levels using a carbon box model assuming Holocene-like conditions (Brehm et al. submitted) after correcting for different atmospheric CO_2 concentrations[26].

The ^{14}C production for the YD and part of our record that captures the Allerød compared to the Holocene shows variable levels, Fig. 2. The Allerød and the onset of the YD –as defined in ice-core NGRIP[1] – show ^{14}C production variations that are close to Holocene. That is until a 40% increase at ~12.8 cal kBP in the YD, which is greater than any continuous rise in the Holocene (Fig 2b-d) leading to a 400-yr period where ^{14}C production is 20% higher than and gradually recovers to Holocene-like levels. During this 400-yr period production varies on century scales, which are likely solar driven.

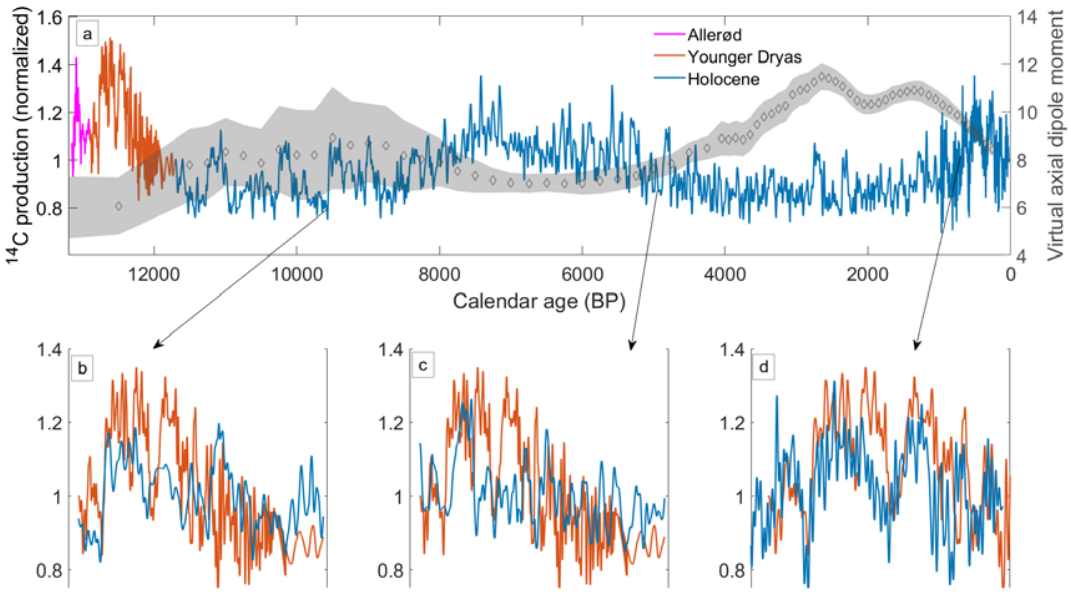

Figure 2 ^{14}C production for the last ~13 cal kBP. a) ^{14}C production for the last 1000-yrs of the Holocene (blue) is calculated from annual ^{14}C made on tree-rings (Brehm et al. submitted) with the rest of Holocene and last 175-years of the YD (orange) based on tree-ring ^{14}C dates in IntCal13 (Reimer et al. 2013). The remainder of the YD and the end of Allerød (pink) is based on ^{14}C introduced in this study. b), c), d) are periods of the Holocene with visual large changes in production (black arrows) scaled to have a mean of 1 and compared to a scaled production from the YD. The boundaries of the YD are defined by deuterium excess from NGRIP (Steffensen et al. 2008)

Solar forcing was shown to be responsible for century variations the Wolf, Spörer and Maunder minima observed between ~600-100 BP[27], Fig. 2d. In particular, these minima corresponded to intervals of where Sun-spots were absents. While for the first time we are able to observe on average 11-year Sun-spot (Schwabe) cycles in the ^{14}C record for the YD, we miss smaller $\Delta^{14}C$ modulation averaging below our precision of 1.6‰ (peak to peak, 1-σ), Fig 3. It is thus trying to ascertain whether these minimums in the YD are the result of absent Sun-spots but does indicate that the underlying mechanics of solar forcing are similar to what has been observed for the last 1000 years. The long-term 400-yr trend of a 20% rise in ^{14}C production in the YD could be the result of the Sun and a combination of the geomagnetic field or the ocean. However, estimates of the virtual axial dipole moment – a measure of the geomagnetic field strength- remain limited for the YD (ref [28] and references therein) and oceanic effects on ^{14}C production cannot be estimated without accurate measurements of ^{10}Be fluxes (see above).

SOLAR INFLUENCE ON THE ONSET OF THE YOUNGER DRYAS

Oceanic, solar and altered atmospheric circulation are currently speculated to have caused the YD that resulted from either an extra-terrestrial impact[11] or natural causes[3, 8, 9, 10]. Initially, Firestone *et al.*[11] proposed an extra-terrestrial impact in America would cool the environment by releasing light-blocking dust particles, which was further exacerbated by soot released from forest set alight by fiery projectiles[29]. In the absence of impact crater the theory remained debated[30] until one was discovered in Greenland[12]. An impact in Greenland would (along with light emitting particles) release fresh-water into Atlantic Ocean, slowing down the Atlantic meridional overturning circulation. Beyond the large increase in ^{14}C production there appears to be no sign perturbation to the carbon-cycle as would be expected from extra-terrestrial impact. This along with the unknown timing of the extra-terrestrial impact[12] and elusive flood paths indicates natural variations caused the sequences of events in the YD. With recent studies and our new ^{14}C record previous estimates of natural variations to the total solar irradiance in the YD may have been underestimated.

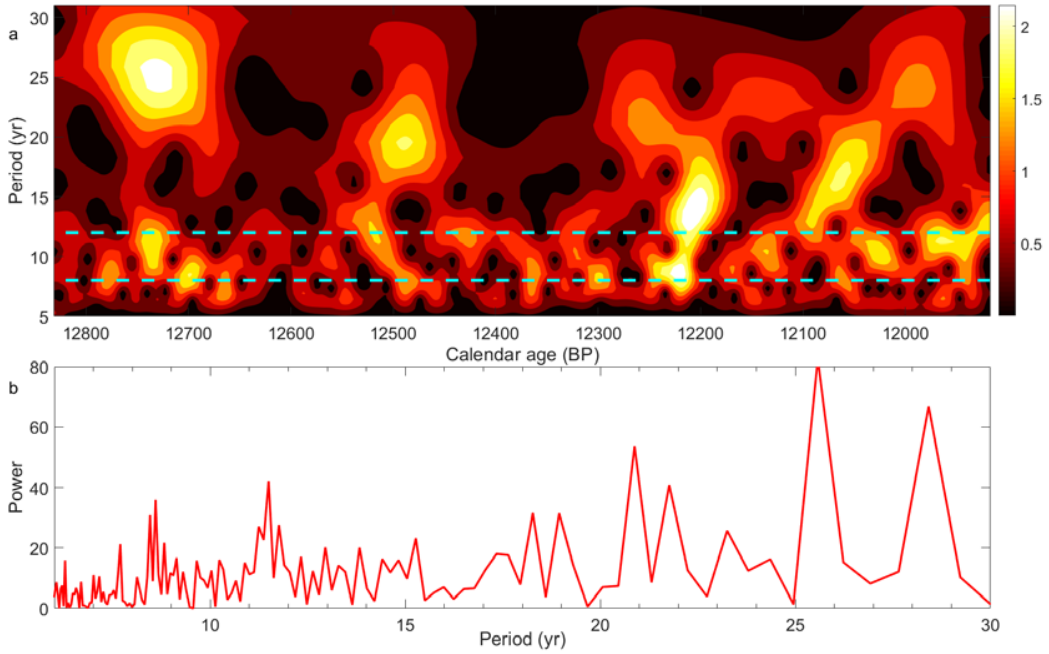

Figure 3 Spectral analysis of atmospheric $\Delta^{14}C$ for the period, 12.8 - 11.9 cal kBP. (a) Wavelet anaylsis and (b) power spectrum (see methods). Horizontal dashes lines represent on average where 11-cycles are expected

Renssen *et al.*[10] proposed a change of 2 W m^{-2} to the total solar irradiance that in combination with a three-year, 5 Sv freshwater pulse and altered atmospheric circulation led to the rapid onset of the YD. Recent estimate of total solar irradiance change between the Maunder minimum, which is speculated to have led to the Little Ice Age[31, 32] and current minima ranges between 3.7 and 4.5 W m^{-2} [33]. The increase ^{14}C production at ~12.8 cal kBP is 40% greater than the Maunder minimum when both periods are scaled to have a mean of one (Fig. 2d). A reduced total solar irradiance of ≥ 4 W m^{-2} could also diminish the need for a three-year, 5 Sv freshwater pulse to be more in-line with geological evidence of a one-year, 0.3 Sv [5]. To test such features would require complex climate models, which is beyond the scope of this study.

OUTLOOK

Although, the ^{14}C calibration curve along with solar variations are now precisely timed (±6-8yrs, 2-σ), calibration of sediments records that give context to the YD remain hindered. Marcofossils ^{14}C-dated in Polish lake sediments[24] and Kråkenes[34] are hinder by large uncertainties >11‰ in $\Delta^{14}C$. Re-measuring these marcofossil with the new high-precision capabilities of accelerator mass spectrometry will help with capturing the sequence of climatic changes in the YD. The Meerfedler Maar record[35] can be re-calibrating by using decadal ^{14}C-dates of tree-rings[15] that time the Laacher See eruption. This shifts Laacher See eruption by~+XX cal years moving Meerfedler Maar chronology to younger ages. A shift to younger ages is in direct contrast to what has been proposed by aligning Vedda Ash tephra from different chronologies[36], which highlights chronological issues. Lastly, resolving issues in ^{10}Be of ice-cores will enable synchronisation of common production signature found in our ^{14}C tree-ring record teasing out solar and oceanic forcing. All of which, would provide a framework for testing probable outcomes of solar forcing coupled to anthropogenic induced changes.

METHODS

Subfossil pines (Pinus sylvestris L.) were discovered over the course of three decades with their dendrochronological links and geological context being discussed in detail[16, 37, 38, 39]. Three trees were sampled from the youngest Swiss chronology (ZHYD3) with tree-rings sampled biennially, triennially and quadrennially. Six trees were sampled from the floating Zurich YD-1 (ZHYD-1, an

updated YD-B chronology), which includes tentative dendrochronological links to Binz trees (Reinig et al., submitted). Tree-rings were sampled from ZHYD1 annually except the youngest ^{14}C-dated tree-rings due to narrow rings. From the floating YD-A chronology[37] two trees were sampled with tree-rings sampled annually to octennially as a consequence of narrow rings and a gap of 25 rings is present as a result of ring deterioration. Three pines were sampled from the floating SWILM chronology[38] with tree-rings sampled annually. A single tree was sampled in annual resolution with ^{14}C overlap to the SWILM but not cross-dated by dendrochronology (see results).

All dates performed on Swiss pines adhere to the Quality Dating protocol (Sookdeo et al., submitted) and were measured as graphite on an in-house Mini CArbon Dating system (MICADAS, Ionplus). In brief, cellulose was extracted using Němec et al.[40] base-acid-base-bleaching steps, placed in a freeze dryer overnight, combusted and graphitized with an in-house AGE-3 system (Ionplus). Samples where measured in batches of 25 accompanied by seven standards, a mixture of oxalic acid I (OXI; NIST SRM 4990B) and II (OXII; NIST SRM 4990C), four wood process blanks- two brown coal wood and two kauri samples-one chemical blank, phthalic anhydride (PhA, Sigma-Aldrich,PN-320064-500 g), and duplicates of a reference material, TK121 with consensus ^{14}C age of 10968 ± 21 (1- σ)[41]. Samples were measured until >200 kcounts of ^{14}C age per were obtained on the MICADAS. A least square (χ^2) distribution model was built in-house with MATLAB (R2017b; The MathWorks Inc™) to ^{14}C wiggle-match high-precision datasets. The least square function we used is defined by Ramsey et al. (2001) as:

$$\chi^2 = \sum_{i=1}^{n} \frac{(x_i - x(t_s + \Delta t_i)^2}{\delta x_i^2}$$

where $x_i \pm \delta x_i$ is ^{14}C measurements, t_s is the death year of a tree and Δt_i are tree-rings relative to t_s. The reduced χ^2 distribution (χ^2_{red}) is obtained by dividing χ^2 by the degrees of freedom (n-1). To create equidistant data when possible the calendar ages were extrapolated based on the number of tree-rings with a constant ^{14}C age and the uncertainty was multiplied by $\sqrt{}$ of the number of rings; otherwise, via linear interpolation. As such the degree of freedom is reduced

to n-2. For comparison of towai (Hogg et al., 2016) and this study's datasets, an additional loss of freedom (n-3) occurred with the consideration of interhemispheric gradient[14, 42]. An additional uncertainty of 1‰ was added to account trees growing in different hemispheres. The uncertainties are reported within a 95% confidence interval (2- σ) based on a maximum value, F_{crit} from statistical tables.

Spectral analyses were carried with a Butterworth band-pass filter of 5 yr^{-1} and 30 yr^{-1}, power spectrums were produced using MATLABS's built-in fast Fourier transform and wavelet analyses were generated with MATLAB's wavelet toolbox (The MathWorks Inc™, 2018).

References

1. Steffensen JP, Andersen KK, Bigler M, Clausen HB, Dahl-Jensen D, Fischer H*, et al.* High-resolution Greenland ice core data show abrupt climate change happens in few years. *Science* 2008, **321**(5889)**:** 680-684.

2. Kindler P, Guillevic M, Baumgartner M, Schwander J, Landais A, Leuenberger M. Temperature reconstruction from 10 to 120 kyr b2k from the NGRIP ice core. *Clim Past* 2014, **10**(2)**:** 887-902.

3. Broecker WS. Massive iceberg discharges as triggers for global climate change. *Nature* 1994, **372:** 421.

4. Broecker WS. Was the Younger Dryas Triggered by a Flood? *Science* 2006, **312**(5777)**:** 1146-1148.

5. Murton JB, Bateman MD, Dallimore SR, Teller JT, Yang Z. Identification of Younger Dryas outburst flood path from Lake Agassiz to the Arctic Ocean. *Nature* 2010, **464:** 740.

6. McManus JF, Francois R, Gherardi J-M, Keigwin LD, Brown-Leger S. Collapse and rapid resumption of Atlantic meridional circulation linked to deglacial climate changes. *Nature* 2004, **428**(6985)**:** 834.

7. Barker S, Diz P, Vautravers MJ, Pike J, Knorr G, Hall IR*, et al.* Interhemispheric Atlantic seesaw response during the last deglaciation. *Nature* 2009, **457:** 1097.

8. Renssen H, Geel Bv, Plicht Jvd, Magny M. Reduced solar activity as a trigger for the start of the Younger Dryas? *Quaternary International* 2000, **68-71:** 373-383.

9. Brauer A, Haug GH, Dulski P, Sigman DM, Negendank JFW. An abrupt wind shift in western Europe at the onset of the Younger Dryas cold period. *Nature Geoscience* 2008, **1**(8)**:** 520-523.

10. Renssen H, Mairesse A, Goosse H, Mathiot P, Heiri O, Roche DM*, et al.* Multiple causes of the Younger Dryas cold period. *Nature Geoscience* 2015, **8**(12)**:** 946-949.

11. Firestone RB, West A, Kennett JP, Becker L, Bunch TE, Revay ZS*, et al.* Evidence for an extraterrestrial impact 12,900 years ago that contributed to the megafaunal extinctions and the Younger Dryas cooling. *Proceedings of the National Academy of Sciences* 2007, **104**(41)**:** 16016-16021.

12. Kjær KH, Larsen NK, Binder T, Bjørk AA, Eisen O, Fahnestock MA*, et al.* A large impact crater beneath Hiawatha Glacier in northwest Greenland. *Science Advances* 2018, **4**(11)**:** eaar8173.

13. Friedrich M, Remmele S, Kromer B, Hofmann J, Spurk M, Kaiser KF*, et al.* The 12,460-year Hohenheim oak and pine tree-ring chronology from central Europe—a unique annual record for radiocarbon calibration and paleoenvironment reconstructions. *Radiocarbon* 2004, **46**(3)**:** 1111-1122.

14. Hogg A, Southon J, Turney C, Palmer J, Ramsey CB, Fenwick P*, et al.* Decadally Resolved Lateglacial Radiocarbon Evidence from New Zealand Kauri. *Radiocarbon* 2016, **58**(04)**:** 709-733.

15. Kromer B, Friedrich M, Hughen KA, Kaiser F, Remmele S, Schaub M*, et al.* Late Glacial 14C Ages from a Floating, 1382-Ring Pine Chronology. *Radiocarbon* 2004, **46**(03)**:** 1203-1209.

16. Hua Q, Barbetti M, Fink D, Kaiser KF, Friedrich M, Kromer B*, et al.* Atmospheric 14C variations derived from tree rings during the early Younger Dryas. *Quaternary Science Reviews* 2009, **28**(25-26)**:** 2982-2990.

17. Muscheler R, Kromer B, Björck S, Svensson A, Friedrich M, Kaiser KF*, et al.* Tree rings and ice cores reveal 14C calibration uncertainties during the Younger Dryas. *Nature Geoscience* 2008, **1**(4)**:** 263-267.

18. Muscheler R, Adolphi F, Knudsen MF. Assessing the differences between the IntCal and Greenland ice-core time scales for the last 14,000 years via the common cosmogenic radionuclide variations. *Quaternary Science Reviews* 2014, **106:** 81-87.

19. Hogg A, Southon J, Turney C, Palmer J, Bronk Ramsey C, Fenwick P*, et al.* Punctuated Shutdown of Atlantic Meridional Overturning Circulation during Greenland Stadial 1. *Scientific Reports* 2016, **6:** 25902.

20. Reimer PJ, Bard E, Bayliss A, Beck JW, Blackwell PG, Ramsey CB*, et al.* IntCal13 and Marine13 Radiocarbon Age Calibration Curves 0–50,000 Years cal BP. *Radiocarbon* 2013, **55**(04)**:** 1869-1887.

21. Capano M, Miramont C, Guibal F, Kromer B, Tuna T, Fagault Y*, et al.* Wood 14C Dating with AixMICADAS: Methods and Application to Tree-Ring Sequences from the Younger Dryas Event in the Southern French Alps. *Radiocarbon* 2017, **60**(01)**:** 51-74.

22. Muscheler R, Beer J, Wagner G, Finkel RC. Changes in deep-water formation during the Younger Dryas event inferred from 10 Be and 14 C records. *Nature* 2000, **408**(6812)**:** 567.

23. Muscheler R, Beer J, Wagner G, Laj C, Kissel C, Raisbeck GM*, et al.* Changes in the carbon cycle during the last deglaciation as indicated by the comparison of 10Be and 14C records. *Earth and Planetary Science Letters* 2004, **219**(3-4)**:** 325-340.

24. Goslar T, Arnold M, Tisnerat-Laborde N, Czernik J, Wi, ecedil K. Variations of Younger Dryas atmospheric radiocarbon explicable without ocean circulation changes. *Nature* 2000, **403**(6772)**:** 877-880.

25. Adolphi F, Muscheler R, Svensson A, Aldahan A, Possnert G, Beer J*, et al.* Persistent link between solar activity and Greenland climate during the Last Glacial Maximum. *Nature Geoscience* 2014, **7:** 662.

26. Members WDP, Buizert C, Adrian B, Ahn J, Albert M, Alley RB*, et al.* Precise interpolar phasing of abrupt climate change during the last ice age. *Nature* 2015, **520:** 661.

27. Stuiver M, Quay PD. Changes in atmospheric carbon-14 attributed to a variable sun. *Science* 1980, **207**(4426)**:** 11-19.

28. Knudsen MF, Riisager P, Donadini F, Snowball I, Muscheler R, Korhonen K*, et al.* Variations in the geomagnetic dipole moment during the Holocene and the past 50 kyr. *Earth and Planetary Science Letters* 2008, **272**(1)**:** 319-329.

29. Kennett DJ, Kennett JP, West GJ, Erlandson JM, Johnson JR, Hendy IL*, et al.* Wildfire and abrupt ecosystem disruption on California's Northern Channel Islands at the Ållerød–Younger Dryas boundary (13.0–12.9ka). *Quaternary Science Reviews* 2008, **27**(27)**:** 2530-2545.

30. Pinter N, Scott AC, Daulton TL, Podoll A, Koeberl C, Anderson RS*, et al.* The Younger Dryas impact hypothesis: A requiem. *Earth-Science Reviews* 2011, **106**(3)**:** 247-264.

31. Mauquoy D, van Geel B, Blaauw M, van der Plicht J. Evidence from northwest European bogs shows 'Little Ice Age' climatic changes driven by variations in solar activity. *The Holocene* 2002, **12**(1)**:** 1-6.

32. Mann ME, Zhang Z, Rutherford S, Bradley RS, Hughes MK, Shindell D*, et al.* Global Signatures and Dynamical Origins of the Little Ice Age and Medieval Climate Anomaly. *Science* 2009, **326**(5957)**:** 1256-1260.

33. Egorova T, Schmutz W, Rozanov E, Shapiro AI, Usoskin I, Beer J*, et al.* Revised historical solar irradiance forcing. *A&A* 2018, **615:** A85.

34. Gulliksen S, Birks HH, Possnert G, Mangerud J. A calendar age estimate of the Younger Dryas-Holocene boundary at Kråkenes, western Norway. *The Holocene* 1998, **8**(3)**:** 249-259.

35. Brauer A, Endres C, Negendank JF. Lateglacial calendar year chronology based on annually laminated sediments from Lake Meerfelder Maar, Germany. *Quaternary International* 1999, **61**(1)**:** 17-25.

36. Lane CS, Brauer A, Blockley SPE, Dulski P. Volcanic ash reveals time-transgressive abrupt climate change during the Younger Dryas. *Geology* 2013, **41**(12)**:** 1251-1254.

37. Schaub M, Kaiser KF, Frank DC, Büntgen U, Kromer B, Talamo S. Environmental change during the Allerød and Younger Dryas reconstructed from Swiss tree-ring data. *Boreas* 2008, **37**(1)**:** 74-86.

38. Kaiser KF, Friedrich M, Miramont C, Kromer B, Sgier M, Schaub M*, et al.* Challenging process to make the Lateglacial tree-ring chronologies from Europe absolute – an inventory. *Quaternary Science Reviews* 2012, **36:** 78-90.

39. Reinig F, Nievergelt D, Esper J, Friedrich M, Helle G, Hellmann L*, et al.* New tree-ring evidence for the Late Glacial period from the northern pre-Alps in eastern Switzerland. *Quaternary Science Reviews* 2018, **186:** 215-224.

40. Němec M, Wacker L, Hajdas I, Gäggeler H. Alternative methods for cellulose preparation for AMS measurement. *Radiocarbon* 2010, **52**(3)**:** 1358-1370.

41. Hogg A, Turney C, Palmer J, Southon J, Kromer B, Ramsey CB*, et al.* The New Zealand kauri (Agathis australis) research project: a radiocarbon dating intercomparison of Younger Dryas wood and implications for IntCal13. *Radiocarbon* 2013, **55**(4)**:** 2035-2048.

42. Hogg A, Palmer J, Boswijk G, Reimer P, Brown D. Investigating the Interhemispheric 14C Offset in the 1st Millennium AD and Assessment of Laboratory Bias and Calibration Errors. *Radiocarbon* 2009, **51**(04)**:** 1177-1186.

Supplementary information

Placements of chronologies

Extension of the absolute German chronology

The 95% CI of a wiggle-match of the ZHYD3 to the 170 high-precision ^{14}C of PPC (Sookdeo et al., in press) falls within the tentative absolute dendrochronology link proposed by Reining et al. (submitted). The placement and subsequent placement of other chronologies discussed below can be found in Tab. S1. The ZHYD3 extension of the PPC introduces 389 nearly annually resolved ^{14}C in 150-years. This period contains a prominent 'wiggle' (10‰ in Δ^{14}C) at 12.2 cal kBP and an additional 'wiggle' (6‰ in Δ^{14}C) found at around 12.3 cal kBP, Fig.1.

Placement of the SH towai record

As the towai chronology was published with decadal ^{14}C dates (with up to five replicates per sample; Hogg et al.2016) the ^{14}C dates of ZHYD3/PPC (henceforth referred to as PPC) were converted to weighted decadal blocks for wiggle-matching. The wiggle-match, after accounting for the different ^{14}C ages of trees growing in North and South –the Interhemispheric gradient (IHG) – Fig.S1 shows good agreement with structures discussed by Sookdeo et al. (in press) and alignment with two prominent wiggles mentioned above (Fig.1).

Placement of the ZHYD1 and YD-A

Tentative dendrochronological links for trees within the ZHYD1 are supported ^{14}C in this study and stable isotopes work that is on-going by Reinig et al. The 635 ^{14}C dates of ZHYD1 were converted to weighted decadal blocks for wiggle-matching to towai, in the same manner as the PPC. The agreement of a rise in ^{14}C (18‰ in Δ^{14}C), a plateau, a decline (11‰ in Δ^{14}C) followed by another increase (25‰ in Δ^{14}C) and two prominent 'wiggles' (both 8‰ in Δ^{14}C) of the towai and ZHYD1 securely places the chronology (Tab. S1). The uncertainty of this placement and subsequent floating chronologies is the sum of squared uncertainties from the wiggle-match and that of the existing floating chronology.

The tentative dendrochronological link of the YD-A to ZHYD1 (Reining et al., submitted) is supported by a wiggle-match of 160 ^{14}C dates from the YDA to ZHYD1, Tab. S1. The chronologies were combined for ensuing discussions. Calendrical and ^{14}C overlap between the ZHYD1 and PPC is limited, Fig.1.

Placement of the SWILM, BINZ0020 and Barbier chronology

The 375 ^{14}C dates SWILM chronology was wiggle-matched to towai in the same manner as the PPC and ZHYD1. The alignment of a climb in ^{14}C (20‰ in Δ^{14}C), a plateau, two 'wiggles' (both 7‰ in Δ^{14}C) and intense increase of (35‰ in Δ^{14}C) in SWILM to towai, firmly places the chronology (Tab. S1). The 98 ^{14}C dates from BINZ0020 were wiggle-matched to SWILM. In addition the barbier chronology was wiggle-matched to the SWILM placement.

Table S1 Placements of ^{14}C dates by wiggle-match or dendrochronology. Chronologies from previous studies are PPC (Sookdeo et al., in press), towai (Hogg et al., 2016) and barbier (Capano et al., 2017). Wiggle matches are reported with a 2-σ uncertainty. An average IHG of 40 ±10 ^{14}C yrs (2-σ) was found between the chronologies. All dendrochronological placements corresponding to Reining et al. (submitted)

Chronology (*trees measured*)	**Matched to**	**^{14}C wiggle-match**	**^{14}C dates placed by dendrochronology**
ZHYD3 (*LAND004/62, KHWI0028*)	PPC	12307 - 11950 ±6	12310 - 11953
Towai	ZHYD3/PPC	13144 - 11704 ±6	-
ZHYD1 (*GAEN0027/102, BINZ0026/73, KHWI0030/31*)	Towai	12652 – 12294 ±8	-
YD-A (*GAEN007/8*)	ZHYD1	12691 – 12539 ± 11	12698 - 12546
SWILM (*GAEN005/71*)	Towai	13161 -12634 ±8	-
(*BINZ0020*)	SWILM	12831 -12704 ±8	-
Barbier	SWILM	12841 -12599 ±10	-

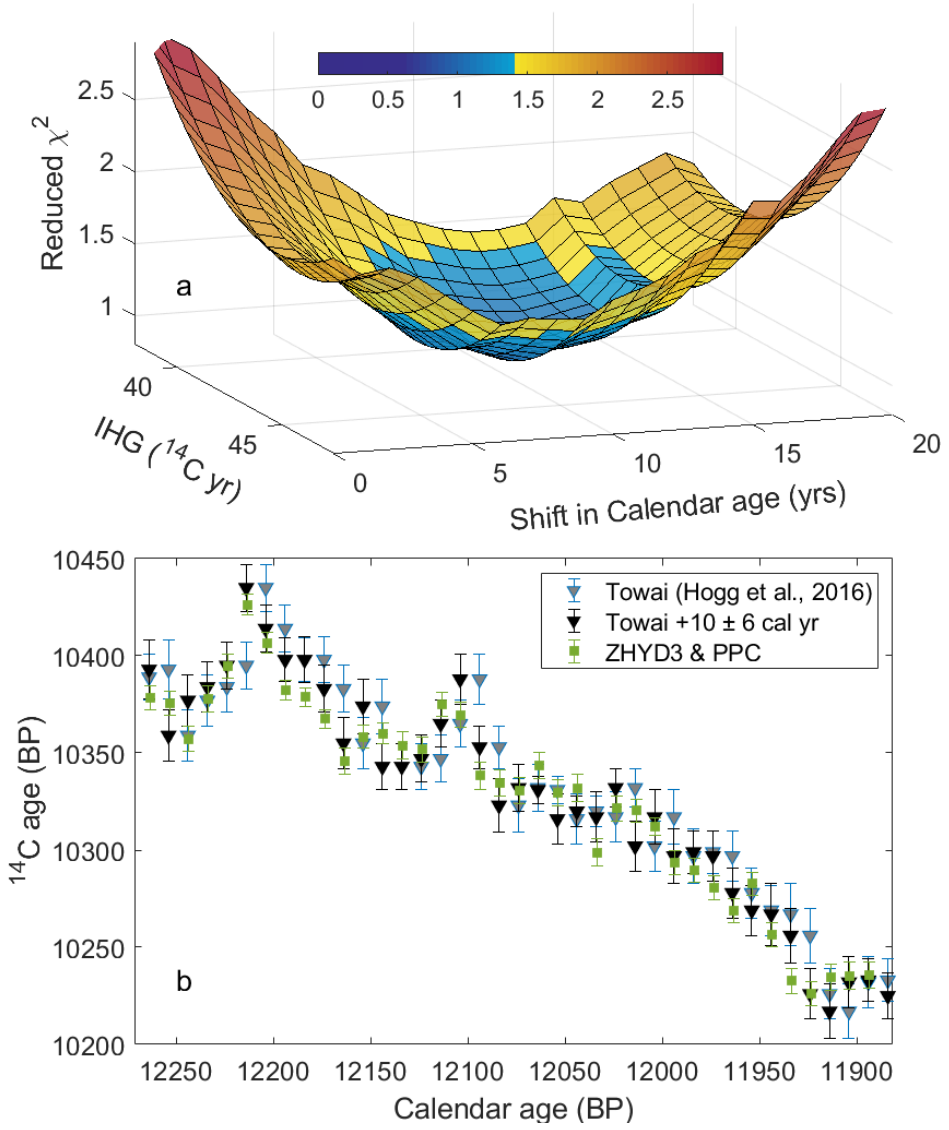

Figure S3 Wiggle-match of the towai chronology (Hogg et al., 2016) to extended PPC (see text). (a) Reduced chi-square model, values shown in blue are within the 95% CI. (b) The decadal ^{14}C averages of the extended PPC (green), the towai placement by Hogg et al., (2016; gray-blue) and the new position based on our wiggle match (black). The 14C age of the towai has be altered by -35 ^{14}C yrs to account for interhemispheric gradient.

Chapter 5

Trees in north, trees in the south

Here we present a discussion on the Interhemispheric gradient (IHG) during the YD. The IHG is the occurrence of tree-rings growing at the same time having different hemispheric ^{14}C ages, which is controlled by the carbon cycle. In particular, the IHG is governed by more expansive ocean and strong winds in the Southern Hemisphere for the Holocene. We use the high-resolution and high-precision measurement produce in this dissertation accompanied by an independent record from France and a well-replicated Southern Hemisphere chronology to determine precisely the IHG. A long-lasting elevation in the IHG is discussed in relation to known climatic changes during the YD derived from various paleo-records. This precisely defined IHG also highlights calendrical uncertainty in the critically important Meerfelder Maar chronology.

5.1 The Interhemispheric gradient during the most recent cooling

5.1.1 Introduction

The 2018 Intergovernmental Panel on Climate Change (IPCC) has reported that 1.5°C global warming above pre-industrial levels will negatively impact: resources, biodiversity, ecosystems, food security, cities, tourism and extreme climate events (O. Hoegh-Guldberg et al., in press). The models used to describe such projections are based on scenario 'x' rather than a prediction. These projections, as well as scenarios, can be tested and better modelled by understanding the processes behind previous large-scale climate-change. Mass ice-sheet movements originating from the Laurentide ice-sheet towards the North Atlantic ocean are associated with rapid cooling in the Northern Hemisphere (NH; Broecker et al. 1994). These types of mass ice-sheet migration are seen as ice-rafted debris in ocean sediments (Henrich, 1988) and have become known as Henrich events. The input of freshwater to the North Atlantic triggers a reduced flow of warm Southern Hemisphere (SH) waters to the NH-formed by Meridional Overturning Circulation (MOC, Broecker, 1994). The reduced MOC creates colder airs over Europe, eventually leading to cooling over the entire NH (Broecker, 1994). The most recent cooling to near glacial-like conditions was the Younger Dryas (YD) but much remains uncertain about the origin and timing of events.

The onset of the YD is marked by similar temperatures to those associated with Henrich events but is notably quicker (Kindler et al., 2014) with limited evidence of ice-rafted debris (Broecker, 2006 and references therein). Flood pathways of the mass ice sheets suggested by Broecker et al. (1989) were discovered in St. Lawrence estuary (Carlson et al., 2007) and the Mackenzie River (Murton et al., 2010), both of which were radiocarbon (^{14}C) dated (within uncertainties) to ~ 12.9 kyr BP (Before 1950 AD). The collapse of the MOC during the YD was predicted to be weaker than a Henrich event based on the multiple flood pathways not directed towards North Atlantic Ocean (Murton et al., 2010). In agreement with a kinetic proxy ($^{231}Pa/^{230}Th$) for MOC that observed a smaller change in the YD than the first Henrich event (McManus et al., 2004). Such a weakened state of the MOC would not explain the cooling that marks the YD; thus, additional mechanisms

were proposed.

Initially, the comet impact theory hypothesized that an asteroid striking in North America would trigger the YD (Firestone et al., 2007). The impact of an asteroid would cool America through the release of light-blocking dust particles. South of the fiery impact, projectiles would set forests alight, resulting in soot that would advance the blockage of light and cooling (Kennett et al., 2008 &2009). In the absence of an impact crater in North American and non-reproducible geochronological evidence, the forest fires could have resulted from natural processes (Pinter et al., 2011). An impact crater found on Greenland, which could be millions of years old or as young as 12 kyr BP, has reignited the compact impact with a twist. The same light blocking particles would be emitted along with an injection of fresh-water from the impacted Greenland ice-sheet, but indications for such a flood remain elusive. In place of a comet, the effect on solar forcing was theorized to be by a weak Sun (Renssen et al. 2000).

A weak Sun was based on an increasing trend of ^{14}C (inversely related to Solar activity) seen in floating chronologies (Hajdas et al., 1998, 2003; Wohlfarth et al., 1998; Kromer et al., 2004). In chapter four we showed this increase was more significant than previously thought, better calendrically constrained and similarly we associated it to a grand solar minimum. Curiously, the grand solar minimum, which starts at 12 810 ± 20 kyr BP (1-σ) occurs about 100 years after the onset of YD in NGRIP ice-core that is defined by a substantial observed change in Deuterium excesses.

Deuterium excesses ($d = \delta D - 8\ \delta^{18}O$) is a measure of the fractionation effects caused by evaporation of the source water. NGRIP at 12896 ± 1.5 kyr BP is marked by an increase of d by 2-3‰ associated to cooling transition (Steffensen et al., 2008). This uncertainty of d is relative to the ice-layers within the core of which has calendrical uncertainty of ± 50 years (Muscheler et al., 2014). Ice-core GRIP, which is on the same time-scale as NGRIP observes a cooling of air temperature[1] also ~200 years after the detected increase in marine moisture temperature (Steffensen et al., 2008). This is likely the result of delayed response or d being oversensitive during this period. No delay (within uncertainties) is seen for the onset of the YD in air temperature and indicators in Europe.

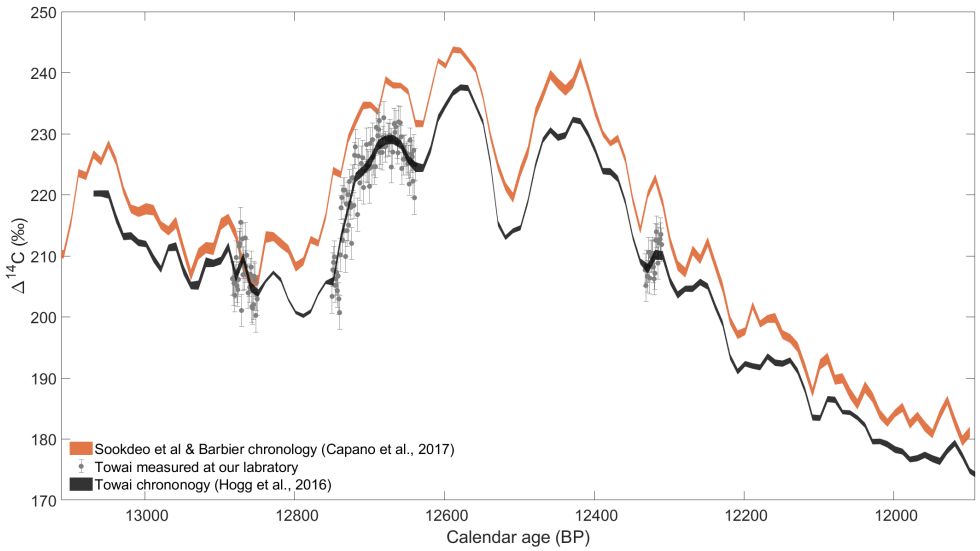

Figure 5.1: Weighted 10 year blocks means of ^{14}C Sookdeo et al Capaneo et al. 2017 (orange). Part of the towai was measured in annual (n> 100) resolution at our lab (gray). And the towai chronology introduced by Hogg et al. 2016 (black).

[1]Cooling of air temperature is observed as a decrease of ^{18}O in ice-cores (Pearman et al., 1976).

Sediment cores from Meerfelder Maar (MFM), Germany mark the onset of YD with consistently thick varves and the cessation of siderite after ~12.7 kyr BP (Brauer et al., 1999 & 2008). The thick varves and absence of siderite were interpreted as indicators of stormier conditions that passed over a cold North Atlantic Ocean before entering Germany (Brauer et al., 2008).

Here we use the sharp rise in ^{14}C production (Chapter 4) and the Interhemispheric Gradient (IHG) to investigate the sequence of events surrounding the YD. The IHG is a measure of the difference in ^{14}C ages of trees-rings growing at the same time in NH and SH (Cain & Suess 1976). For the Holocene, the IHG is observed to be 35 ± 3 ^{14}C yr (1σ), a result of more ^{14}C-depleted CO_2 in the SH (see supplementary information). This depletion is considered to be a result of more expansive ocean coverage along with stronger winds in the SH compared to NH (Cain and Suess 1976; Braziunas et al., 1995). A first attempt to determine any change in the IHG at the beginning of the YD was performed by Hogg et al. (2016) However, the measurement precision did not allow for a safe interpretation due to low sampling resolution on the NH record.

5.1.2 Results and discussion

A subset of tree-rings in the towai chronology was annual ^{14}C dated at our laboratory, figure 5.1. No visible discrepancies between annual towai measurements (n > 100) and Hogg et al. (2016) ensure that the IHG we observe is not a product of laboratory offsets (McCormac et al., 1998; Hogg et al., 2009a). The Barbier chronology (Capano et al., 2017) was incorporated into NH record of this study to further increase the robustness of the observed IHG. We use decadal weighted means of chronologies introduced in this dissertation and the Barbier chronology to compare to decadal blocks of towai measured by Hogg et al. (2016).

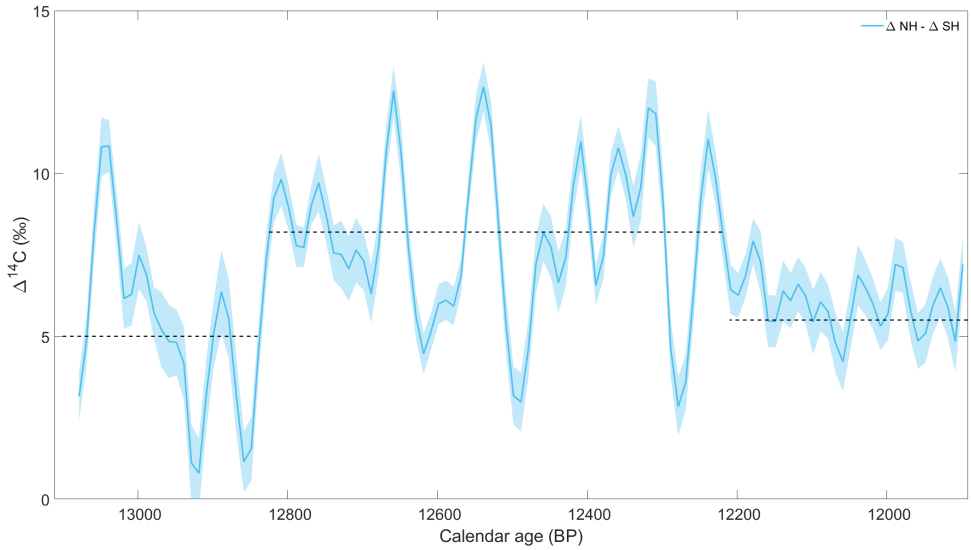

Figure 5.2: The IHG for 10 years block of the NH and SH, shaded blue errors indicated 1-σ uncertainties.

While the IHG for this period is similar to values observed in the Holocene, a remarkable increase of ~3 ‰ in $\Delta^{14}C$), occurs around 12.8 kyr BP. After, the mean IHG remains elevated for ~ 600 years, with large fluctuations (≥ 4) before returning to Holocene-like levels, figure 5.2. The longevity of this IHG change cannot be explained by a reduced phase of the MOC, as it remains for the majority of the YD (McManus et al., 2004). Further, it is also questionable whether the IHG change is the result of a comet impact. A comet impacting Greenland around 12.8 kyr BP (Kjaer et al., 2018), should cause a distribution in the carbon cycle that would change IHG. This change would have dramatic and within a year or two eventually leading to sustained IHG for duration

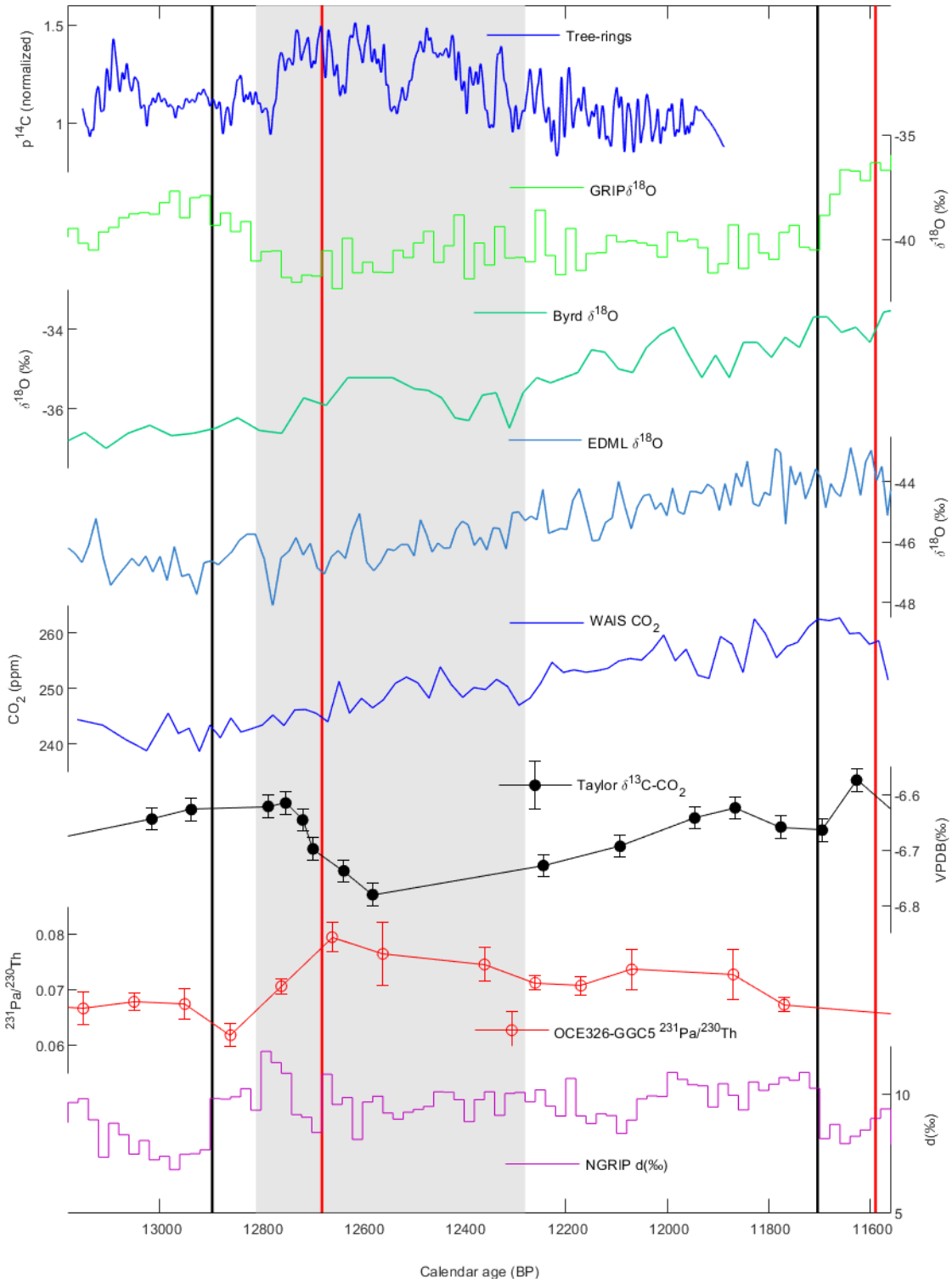

Figure 5.3: ^{14}C production (Chapter 4). GRIP ice-core δ^{18}O (Johnsen et al. 1992). Byrd ice-core δ^{18}O (Blunier et al.).EDML ice-core δ^{18}O (Epica community members, 2006). Taylor Glacial δ^{13}C-CO_2 (Bauksa et al., 2016).OCE326-GGC5 sediment-core ^{231}Pa/^{230}Th (McManus et al., 2004). WAIS CO_2 (WAIS Divide project members 2015). NGRIP *d* excess (Steffensen et al., 2008). The gray patch indicates calendrical where an elevation of IHG occurred. Black and red vertical lines indicated the start and end dates of YD in the NGRIP and MFM, respectively.

of the YD. Neither of which, is visible in the IHG for the period. Thus the comet-derived crater

discovered by Kjaer et al. (2018) has to be older than 13 kyr BP. Without a comet, the elevated IHG must arise from some other forcing.

We consider a combination of three primary forces to be responsible for the observed IHG change, figure 5.3:

1. A grand solar minimum seen in the in production of ^{14}C.
2. A reduced MOC noted by McManus et al. (2004) as an increase $^{231}Pa/^{230}Th$.
3. More active Southern Oceans perceived as the anti-phase trend in ^{18}O from SH ice-cores (Broecker, 1997; Stocker and Johnsen 2003) for which we have plotted Bryd & EDML.

A grand solar minimum would increase production of ^{14}C at the poles eventually causing a larger gradient due to the carbon cycle dynamics as the signal in SH is more dampened due to the larger surface of the ocean. Such an effect was most likely also seen with global measurements AD 774-775 event (Büntgen et al., 2018), where due to a globally increased ^{14}C production a stronger ^{14}C increase in the atmosphere was observed on the NH than the SH. Similarly, the combined effects of a grand solar minimum, weak MOC in the NH (enriching atmospheric $^{14}CO_2$) and increase SH ocean (depleting atmospheric $^{14}CO_2$) would further drive the IHG. The stronger SH westerlies winds that are associated with cold phases of the North Atlantic oceans (Anderson et al., 2009; Lee et al., 2011) would also deplete ^{14}C in the SH. The change in the westerlies winds may not be constant but frequently reoccurring, explaining the significant variations in the IHG (figure 5.2). These variations may also be the result of an increase in biological pump activity, which is associated with the rise of CO_2 and decreasing $\delta^{13}C$-CO_2 (Bauska et al. 2016). While there is relatively linearly increase of CO_2 (WAIS) and gradual decline of $\delta^{13}C$-CO_2 (Taylor) there may have been more sporadic changes not captured because of the resolution of the ice cores. These sporadic changes would introduce depleted $^{14}CO_2$ from the SH ocean, affecting the IHG. The above changes are synchronous with the beginning of the IHG change and also corresponds to (within calendrical uncertainties) the onset of YD in GRIP.

The onset of YD in GRIP proposed by Johnsen et al. (1992) is 12700 ± 100 kyr BP and in agreement with the beginning of the change in the IHG (figure 5.3). NGRIP is not with change *d* excess occuring ~100-yr before the IHG (Steffenson et al. 2008). This ~150-yr difference could again point to a delayed response of marine moisture and air temperatures changes or oversensitive of *d* excess for this period. The start of IHG change does not align with the onset of YD in MFM at 12 680 ± 50 kyr BP (Brauer et al., 1999).

This begs the question, are the calendrical uncertainties in the MFM underestimated? Underestimated calendrical uncertainties would explain why the forcing mentioned above, that affect the IHG does not affect varve and siderite formation until ~100 years later in the MFM. If the start date of YD in the MFM were to be shifted to start of the IHG, it would still align with the onset and agree with the end date of the YD recorded in GRIP (figure 5.3). However, this shift would then disagree with Lane et al. (2013) finding that Vedda ash (another tephra marker) in MFM should be shifted younger to align with other records containing Vedda ash. It is, therefore, uncertain were the calendrical issues in lie in the MFM and should be the study of future investigation.

5.1.3 Conclusion

The IHG allows for new insights into the timing of paleoclimate events that resulted in a general cooling of the NH. The IHG allows primarily detecting changes in the carbon cycle and thus adds important information for a better understanding of the cause of the YD cold event. The study presented here relies heavily on high-resolution and high precision measurement on the SH as well as the NH to determine precisely the IHG. We measured a significant increase in IHG starting at ~ 12.8 kyr BP, delayed about 150 years compared to the increase in the deuterium excess in Greenland ice cores, which defines the onset of the YD. The IHG offset changes back to pre-YD

and Holocene levels after roughly 600 years. We think the observed change in IHG is a result of three major forces influencing the carbon cycle:

- A grand solar minimum
- A reduced Meridional Overturning Circulation
- More active Southern Oceans accompanied by increase in SH westerlies wind.

The onset of the YD in the MFM chronology is outside the 95% CI for calendrical onset of the elevated IHG, which is possible due to have underestimated of the MFM. One feature remains unsolved, why the IHG returned before the end YD.

Supplementary information

This weighted mean of the IHG is calculated based on values in table S.1. It ignores IHG observed by Stuiver and Braziunas (1998) because of an issue with radon-blank corrections and values between AD 245-335 due to 30% of data points be anomalously low (see Hogg et al., 2009)

Table S.1 previously published Interhemispheric gradient observations

Authors	Geographic location of Sample pairs Southern/ Northern Hemisphere	Cal age of Samples	Interhemispheric Gradient (^{14}C yr±1σ)
Lerman et al., 1970	Northern Patagonia/ Europe	~AD 1835	36 ± 8
Vogel et al., 1986	South Africa/ Netherlands	~AD 1840-1890	36 ± 7
Vogel et al., 1993	South Africa/ Netherlands	~AD 1835-1900	31 ± 5
Stuiver and Braziunas 1998	Chile/ Western United States	19th century	23 ± 4
Hogg et al., 2002	New Zealand/ United Kingdom	AD 1950-1850	40 ± 13
Hogg et al., 2009	New Zealand/ Ireland	AD 245-335 AD 745-785 AD 895-935	21 ± 9 57 ± 12 37 ± 12

5.1.4 References

Anderson, R., Ali, S., Bradtmiller, L., Nielsen, S., Fleisher, M., Anderson, B., Burckle, L., 2009. Wind-driven upwelling in the Southern Ocean and the deglacial rise in atmospheric CO<$_2$. Science 323, 1443-1448.

Bauska, T.K., Baggenstos, D., Brook, E.J., Mix, A.C., Marcott, S.A., Petrenko, V.V., Schaefer, H., Severinghaus, J.P., Lee, J.E., 2016. Carbon isotopes characterize rapid changes in atmospheric carbon dioxide during the last deglaciation. Proc. Natl. Acad. Sci. U. S. A. 113, 3465-3470.

Brauer, A., Endres, C., Negendank, J.F., 1999. Lateglacial calendar year chronology based on annually laminated sediments from Lake Meerfelder Maar, Germany. Quaternary International 61, 17-25.

Brauer, A., Haug, G.H., Dulski, P., Sigman, D.M., Negendank, J.F.W., 2008. An abrupt wind shift in western Europe at the onset of the Younger Dryas cold period. Nature Geoscience 1, 520-523.

Braziunas, T.F., Fung, I.Y., Stuiver, M., 1995. The preindustrial atmospheric14CO2 latitudinal gradient as related to exchanges among atmospheric, oceanic, and terrestrial reservoirs. Global Biogeochemical Cycles 9, 565-584.

Broecker, W.S., 1994. Massive iceberg discharges as triggers for global climate change. Nature 372, 421.

Broecker, W.S., 1997. Thermohaline Circulation, the Achilles Heel of Our Climate System: Will Man-Made CO<$_2$ Upset the Current Balance? Science 278, 1582-1588.

Broecker, W.S., 2006. Was the Younger Dryas Triggered by a Flood? Science 312, 1146-1148.

Broecker, W.S., Kennett, J.P., Flower, B.P., Teller, J.T., Trumbore, S., Bonani, G., Wolfli, W., 1989. Routing of meltwater from the Laurentide Ice Sheet during the Younger Dryas cold episode. Nature 341, 318.

Büntgen, U., Wacker, L., Galván, J.D., Arnold, S., Arseneault, D., Baillie, M., Beer, J., Bernabei, M., Bleicher, N., Boswijk, G., Bräuning, A., Carrer, M., Ljungqvist, F.C., Cherubini, P., Christl, M., Christie, D.A., Clark, P.W., Cook, E.R., D'Arrigo, R., Davi, N., Eggertsson, Ó., Esper, J., Fowler, A.M., Gedalof, Z.e., Gennaretti, F., Grießinger, J., Grissino-Mayer, H., Grudd, H., Gunnarson, B.E., Hantemirov, R., Herzig, F., Hessl, A., Heussner, K.-U., Jull, A.J.T., Kukarskih, V., Kirdyanov, A., Kolář, T., Krusic, P.J., Kyncl, T., Lara, A., LeQuesne, C., Linderholm, H.W., Loader, N.J., Luckman, B., Miyake, F., Myglan, V.S., Nicolussi, K., Oppenheimer, C., Palmer, J., Panyushkina, I., Pederson, N., Rybníček, M., Schweingruber, F.H., Seim, A., Sigl, M., Churakova, O., Speer, J.H., Synal, H.-A., Tegel, W., Treydte, K., Villalba, R., Wiles, G., Wilson, R., Winship, L.J., Wunder, J., Yang, B., Young, G.H.F., 2018. Tree rings reveal globally coherent signature of cosmogenic radiocarbon events in 774 and 993 CE. Nature Communications 9, 3605.

Cain, W.F., Suess, H.E., 1976. Carbon 14 in tree rings. Journal of Geophysical Research 81, 3688-3694.

Capano, M., Miramont, C., Guibal, F., Kromer, B., Tuna, T., Fagault, Y., Bard, E., 2017. Wood 14C Dating with AixMICADAS: Methods and Application to Tree-Ring Sequences from the Younger Dryas Event in the Southern French Alps. Radiocarbon 60, 51-74.

Blunier, T., Chappellaz, J., Schwander, J., Dällenbach, A., Stauffer, B., Stocker, T.F., Raynaud, D., Jouzel, J., Clausen, H.B., Hammer, C.U., Johnsen, S.J., 1998. Asynchrony of Antarctic and Greenland climate change during the last glacial period. Nature 394, 739.

Carlson, A.E., Clark, P.U., Haley, B.A., Klinkhammer, G.P., Simmons, K., Brook, E.J., Meissner, K.J., 2007. Geochemical proxies of North American freshwater routing during the Younger Dryas cold event. Proceedings of the National Academy of Sciences 104, 6556-6561.

Epica community members, Barbante, C., Barnola, J.M., Becagli, S., Beer, J., Bigler, M., Boutron, C., Blunier, T., Castellano, E., Cattani, O., Chappellaz, J., Dahl-Jensen, D., Debret, M., Delmonte, B., Dick, D., Falourd, S., Faria, S., Federer, U., Fischer, H., Freitag, J., Frenzel, A., Fritzsche, D., Fundel, F., Gabrielli, P., Gaspari, V., Gersonde, R., Graf, W., Grigoriev, D., Hamann, I., Hansson, M., Hoffmann, G., Hutterli, M.A., Huybrechts, P., Isaksson, E., Johnsen, S., Jouzel, J., Kaczmarska, M., Karlin, T., Kaufmann, P., Kipfstuhl, S., Kohno, M., Lambert, F., Lambrecht,

A., Lambrecht, A., Landais, A., Lawer, G., Leuenberger, M., Littot, G., Loulergue, L., Lüthi, D., Maggi, V., Marino, F., Masson-Delmotte, V., Meyer, H., Miller, H., Mulvaney, R., Narcisi, B., Oerlemans, J., Oerter, H., Parrenin, F., Petit, J.R., Raisbeck, G., Raynaud, D., Röthlisberger, R., Ruth, U., Rybak, O., Severi, M., Schmitt, J., Schwander, J., Siegenthaler, U., Siggaard-Andersen, M.L., Spahni, R., Steffensen, J.P., Stenni, B., Stocker, T.F., Tison, J.L., Traversi, R., Udisti, R., Valero-Delgado, F., van den Broeke, M.R., van de Wal, R.S.W., Wagenbach, D., Wegner, A., Weiler, K., Wilhelms, F., Winther, J.G., Wolff, E., 2006. One-to-one coupling of glacial climate variability in Greenland and Antarctica. Nature 444, 195. Firestone, R.B., West, A., Kennett, J.P., Becker, L., Bunch, T.E., Revay, Z.S., Schultz, P.H., Belgya, T., Kennett, D.J., Erlandson, J.M., Dickenson, O.J., Goodyear, A.C., Harris, R.S., Howard, G.A., Kloosterman, J.B., Lechler, P., Mayewski, P.A., Montgomery, J., Poreda, R., Darrah, T., Hee, S.S.Q., Smith, A.R., Stich, A., Topping, W., Wittke, J.H., Wolbach, W.S., 2007. Evidence for an extraterrestrial impact 12,900 years ago that contributed to the megafaunal extinctions and the Younger Dryas cooling. Proceedings of the National Academy of Sciences 104, 16016-16021.

Hajdas, I., Bonani, G., Boden, P., Peteet, D.M., Mann, D.H., 1998. Cold reversal on Kodiak Island, Alaska, correlated with the European Younger Dryas by using variations of atmospheric 14C content. Geology 26, 1047-1050.

Hajdas, I., Bonani, G., Moreno, P.I., Ariztegui, D., 2003. Precise radiocarbon dating of Late-Glacial cooling in mid-latitude South America. Quaternary Research 59, 70-78.

Heinrich, H., 1988. Origin and Consequences of Cyclic Ice Rafting in the Northeast Atlantic Ocean During the Past 130,000 Years. Quaternary Research 29, 142-152.

Hogg, A., Bronk Ramsey, C., Turney, C., Palmer, J., 2009. Bayesian Evaluation of the Southern Hemisphere Radiocarbon Offset during the Holocene. Radiocarbon 51, 1165-1176.

Hogg, A., Palmer, J., Boswijk, G., Reimer, P., Brown, D., 2009. Investigating the Interhemispheric ^{14}C Offset in the 1st Millennium AD and Assessment of Laboratory Bias and Calibration Errors. Radiocarbon 51, 1177-1186.

Hogg, A., Southon, J., Turney, C., Palmer, J., Ramsey, C.B., Fenwick, P., Boswijk, G., Büntgen, U., Friedrich, M., Helle, G., Hughen, K., Jones, R., Kromer, B., Noronha, A., Reinig, F., Reynard, L., Staff, R., Wacker, L., 2016. Decadally Resolved Lateglacial Radiocarbon Evidence from New Zealand Kauri. Radiocarbon 58, 709-733.

Johnsen, S.J., Clausen, H.B., Dansgaard, W., Fuhrer, K., Gundestrup, N., Hammer, C.U., Iversen, P., Jouzel, J., Stauffer, B., steffensen, J.P., 1992. Irregular glacial interstadials recorded in a new Greenland ice core. Nature 359, 311. Kennett, D.J., Kennett, J.P., West, A., Mercer, C., Hee, S.S.Q., Bement, L., Bunch, T.E., Sellers, M., Wolbach, W.S., 2009. Nanodiamonds in the Younger Dryas Boundary Sediment Layer. Science 323, 94-94.

Kennett, D.J., Kennett, J.P., West, G.J., Erlandson, J.M., Johnson, J.R., Hendy, I.L., West, A., Culleton, B.J., Jones, T.L., Stafford, T.W., 2008. Wildfire and abrupt ecosystem disruption on California's Northern Channel Islands at the Ållerød–Younger Dryas boundary (13.0–12.9ka). Quaternary Science Reviews 27, 2530-2545.

Kindler, P., Guillevic, M., Baumgartner, M., Schwander, J., Landais, A., Leuenberger, M., 2014. Temperature reconstruction from 10 to 120 kyr b2k from the NGRIP ice core. Clim. Past 10, 887-902.

Kjær, K.H., Larsen, N.K., Binder, T., Bjørk, A.A., Eisen, O., Fahnestock, M.A., Funder, S., Garde, A.A., Haack, H., Helm, V., Houmark-Nielsen, M., Kjeldsen, K.K., Khan, S.A., Machguth, H., McDonald, I., Morlighem, M., Mouginot, J., Paden, J.D., Waight, T.E., Weikusat, C., Willerslev, E., MacGregor, J.A., 2018. A large impact crater beneath Hiawatha Glacier in northwest Greenland. Science Advances 4.

Kromer, B., Friedrich, M., Hughen, K.A., Kaiser, F., Remmele, S., Schaub, M., Talamo, S., 2004. Late Glacial ^{14}C Ages from a Floating, 1382-Ring Pine Chronology. Radiocarbon 46, 1203-1209.

Lane, C.S., Brauer, A., Blockley, S.P.E., Dulski, P., 2013. Volcanic ash reveals time-transgressive abrupt climate change during the Younger Dryas. Geology 41, 1251-1254.

Lee, S.-Y., Chiang, J.C.H., Matsumoto, K., Tokos, K.S., 2011. Southern Ocean wind response to North Atlantic cooling and the rise in atmospheric CO_2: Modeling perspective and paleoceanographic implications. Paleoceanography 26.
McCormac, F.G., Hogg, A.G., Higham, T.F.G., Baillie, M.G.L., Palmer, J.G., Xiong, L., Pilcher, J.R., Brown, D., Hoper, S.T., 1998. Variations of Radiocarbon in Tree Rings: Southern Hemisphere Offset Preliminary Results. Radiocarbon 40, 1153-1159.
McManus, J.F., Francois, R., Gherardi, J.-M., Keigwin, L.D., Brown-Leger, S., 2004. Collapse and rapid resumption of Atlantic meridional circulation linked to deglacial climate changes. Nature 428, 834.
Murton, J.B., Bateman, M.D., Dallimore, S.R., Teller, J.T., Yang, Z., 2010. Identification of Younger Dryas outburst flood path from Lake Agassiz to the Arctic Ocean. Nature 464, 740.
Muscheler, R., Adolphi, F., Knudsen, M.F., 2014. Assessing the differences between the IntCal and Greenland ice-core time scales for the last 14,000 years via the common cosmogenic radionuclide variations. Quaternary Science Reviews 106, 81-87.
Pinter, N., Scott, A.C., Daulton, T.L., Podoll, A., Koeberl, C., Anderson, R.S., Ishman, S.E., 2011. The Younger Dryas impact hypothesis: A requiem. Earth-Science Reviews 106, 247-264.
Renssen, H., Geel, B.v., Plicht, J.v.d., Magny, M., 2000. Reduced solar activity as a trigger for the start of the Younger Dryas? Quaternary International 68-71, 373-383.
Renssen, H., Mairesse, A., Goosse, H., Mathiot, P., Heiri, O., Roche, D.M., Nisancioglu, K.H., Valdes, P.J., 2015. Multiple causes of the Younger Dryas cold period. Nature Geoscience 8, 946-949.
Steffensen, J.P., Andersen, K.K., Bigler, M., Clausen, H.B., Dahl-Jensen, D., Fischer, H., Goto-Azuma, K., Hansson, M., Johnsen, S.J., Jouzel, J., 2008. High-resolution Greenland ice core data show abrupt climate change happens in few years. Science 321, 680-684.
Stocker, T.F., Johnsen, S.J., 2003. A minimum thermodynamic model for the bipolar seesaw. Paleoceanography 18.
WAIS divide project members ., Buizert, C., Adrian, B., Ahn, J., Albert, M., Alley, R.B., Baggenstos, D., Bauska, T.K., Bay, R.C., Bencivengo, B.B., Bentley, C.R., Brook, E.J., Chellman, N.J., Clow, G.D., Cole-Dai, J., Conway, H., Cravens, E., Cuffey, K.M., Dunbar, N.W., Edwards, J.S., Fegyveresi, J.M., Ferris, D.G., Fitzpatrick, J.J., Fudge, T.J., Gibson, C.J., Gkinis, V., Goetz, J.J., Gregory, S., Hargreaves, G.M., Iverson, N., Johnson, J.A., Jones, T.R., Kalk, M.L., Kippenhan, M.J., Koffman, B.G., Kreutz, K., Kuhl, T.W., Lebar, D.A., Lee, J.E., Marcott, S.A., Markle, B.R., Maselli, O.J., McConnell, J.R., McGwire, K.C., Mitchell, L.E., Mortensen, N.B., Neff, P.D., Nishiizumi, K., Nunn, R.M., Orsi, A.J., Pasteris, D.R., Pedro, J.B., Pettit, E.C., Buford Price, P., Priscu, J.C., Rhodes, R.H., Rosen, J.L., Schauer, A.J., Schoenemann, S.W., Sendelbach, P.J., Severinghaus, J.P., Shturmakov, A.J., Sigl, M., Slawny, K.R., Souney, J.M., Sowers, T.A., Spencer, M.K., Steig, E.J., Taylor, K.C., Twickler, M.S., Vaughn, B.H., Voigt, D.E., Waddington, E.D., Welten, K.C., Wendricks, A.W., White, J.W.C., Winstrup, M., Wong, G.J., Woodruff, T.E., 2015. Precise interpolar phasing of abrupt climate change during the last ice age. Nature 520, 661.
Wohlfarth , B., Björck, S., Possnert, G., Holmquist , B., 1998. An 800-year long, radiocarbon-dated varve chronology from south-eastern Sweden. Boreas 27, 243-257.

Chapter 6

Summary and outlook

On that fateful day in 2013, the 253 Binz trees were discovered leading to (in part) this dissertation. One of the main goals of the project was to extend the absolute German dendrochronology with Binz trees, a preliminary ^{14}C dating of ten trees overlapped and extended several hundred to thousands of years older than the absolute chronology. Thus began my PhD: to methodological find and date the 'right' trees, place those trees precisely on calendrical time-scales and finally figure out the underlying story behind those dates.

The technique used to date those ten trees involved a chemical process, along with measurement times that could last several days. Determining the ^{14}C age of remaining Binz trees would take $\sim$ 10 weeks. We deliberated if there was a way we could somehow skip or reduce the chemical processes involved, leading to the creation of Speed Dating. Speed Dating, made use of the existing Elementar Analyzer (EA) coupled to a MICADAS, which had limited applications. The EA was used to combust wood samples with the resulting CO_2-a fraction of which contains ^{14}C-measured on the MICADAS. This application of EA-MICADAS, Speed Dating was shown to have:

- Robust standard normalization
- Reproducible blanks
- accurate ^{14}C dating of reference materials
- Capable of ^{14}C dating samples older than 25 kyr.

The Speed Dating application increased sample throughput by 15x, reduced the cost by a third and uncertainties $\leq$2% were obtainable. The paper, 'Speed Dating: A rapid way to Determine the radiocarbon age of wood by EA-AMS' was submitted to the journal of Radiocarbon within the first year of my PhD.

The Speed Dates of Binz dendrochronologies were either too old or too young to extend the absolute chronology. One chronology, Binz 7 overlapped with floating Swiss chronologies with a small number of trees. In the hunt for more trees, we visited storage facilities in Germany and Switzerland, Speed dating over 800 samples, all of which were too young to extend the absolute chronology. In lieu of new trees, we decided to work with the absolute chronology, the Swiss floating chronologies (built by Felix Kaiser and his colleagues) as well the newly discovered Binz 7 chronology. As these chronologies overlapped in time-based on over 100 decadal ^{14}C dates and Speed Dates-leading us to pursue the possibility of linking chronologies by high-precision 'wiggle' matching.

Oddly, the term, 'high-precision ^{14}C dates' is used in numerous publications (a google search yielded 895 results) with minimal discussions on quality control. A main control for testing the quality of a ^{14}C date is a laboratory-to-laboratory comparison. These intercomparisons are few and far between with only a handful of published. In light of this, we submitted 'Quality Dating a protocol for reproducible high precision ^{14}C dates applied to Late Glacial wood' to the journal of

Radiocarbon, which was accepted with revision on 01/2019. The Quality dating protocol was an outcome of the 1705 samples we measured at ETH always being accompanied by

- Four process blanks rather than chemical blanks due to significantly different ^{14}C ages.
- Seven standards, four or three of which were OXAI and the remainder OXAII to ensure robust standard normalization.
- Two references, representative of the sample material and age to confirm reproducible results.

Also, we had an intercomparison experiment with CEZA in Germany that showed a minimal difference in ^{14}C ages and appropriate uncertainty estimations. During Quality Dating, we worked on wiggle-matching trees from floating chronologies to the absolute chronology. In combination with the measurements from CEZA (n = 75), 1780 ^{14}C dates were used to draft the paper 'There goes the Sun: Reconstructing atmospheric ^{14}C reveals prolonged solar minimum in the Younger Dryas' submitted to Nature Geoscience. Tree-ring chronologies in this were:

- extended and increases the resolution by a factor of six for the absolute dated chronology.
- Precisely calendrically places the floating SH towai chronology.
- Increase the resolution by a factor of four for the floating ZHYD1 chronology, which is shifted by +70-years.
- Increases the resolution by a factor of three for the floating SWILM chronology, which is shifted by +35-years.

The extension of the absolute chronology and precise calendrical placement of the floating chronology enables the investigation of solar variability. We see that in the YD there is 40% increase in production that is unmatched in the Holocene. This is the start of a 400-yr period that on average remains 20% elevated when compared to the Holocene. Both the 40% rise and variations during the 400-yr period are shown to be solar driven with patterns matching those seen in Holocene, albeit with larger amplitudes. Moreover, solar forcing in the YD is speculated to be reduced by more than 5 W m−2, which is greater than previously estimated. This weak Sun could have played more of a role in the onset of the YD.

The almost continuous overlap between the Swiss and German ^{14}C dates presented in this dissertation and the New Zealand chronology enabled an investigation of the InterHemispheric Gradient (IHG). The IHG allows primarily for detecting changes in the carbon cycle and thus adds important information for a better understanding of the cause of the YD cold event. The study presented here relies heavily on high-resolution and high precision measurement on the SH as well as the NH to determine precisely the IHG. We measured a significant increase in IHG starting at $\sim$ 12.8 kyr BP, delayed about 150 years compared to the increase in the deuterium excess in Greenland ice cores defining the onset of the YD. The IHG offset changes back to pre-YD and Holocene levels after roughly 600 years. We think the observed change in IHG is a result of three major forces influencing the carbon cycle:

- A grand solar minimum
- A reduced Meridional Overturning Circulation
- More active Southern Oceans accompanied by increase in SH westerlies wind.

The onset of the YD in the MFM chronology is outside the 95% CI for calendrical onset of the elevated IHG, which is possible due to underestimation of the MFM. There is ongoing work by F. Reinig to precisely date Laacher See tephra-an anchor in the MFM- by wiggle-matching to SWILM chronology produced in this study (figure 6.1).

In the future, similar studies will be able to take advantage of Speed Dating, to find the 'right' trees and Quality Dating to investigate modulation of atmospheric ^{14}C. These modulations can highlight variations in Solar activity and the Earth systems making it an exciting time to be in the field of ^{14}C.

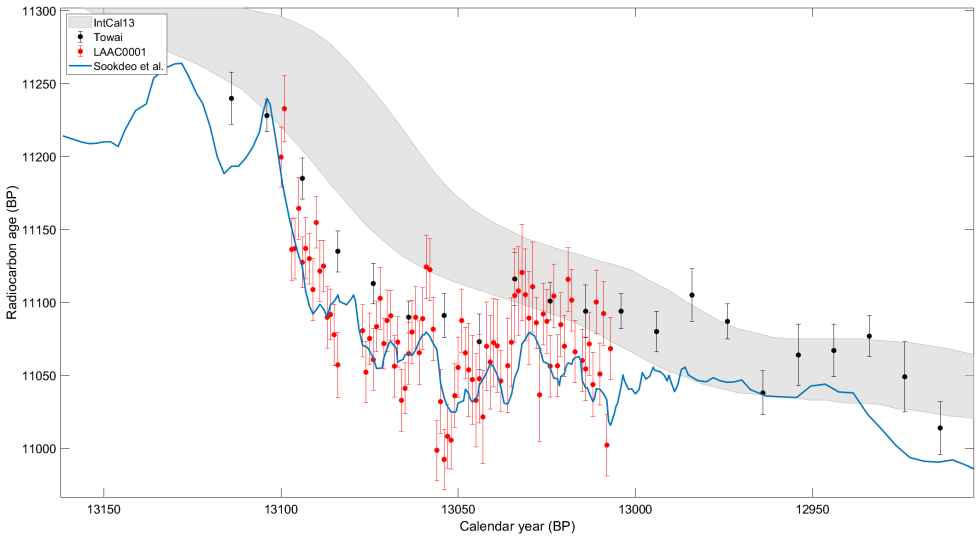

Figure 6.1: Work be F. Reining to wiggle a tree, LAAC0001 (red), which is believed to have died during the Laacher See eruption to SWILM dates produced in this dissertation (blue). IntCal13 is given gray and the towai chronology in black.

Appendices

Appendix A

High-precision ^{14}C dates

Below is a table containing all high-precision ^{14}C dates produced during this dissertation.

Table appendix A : All 1705 highly resolved, high-precision ^{14}C performed at ETH-Zürich during this dissertation. All dates listd below followed the Quality Dating protocol.

Tree_Name	Tree-ring (midpoint)	calage cal BP	calspan	calsigD	c14age	c14sig	lab_id
GAEN0005	63.5	12802.5	2	4	10894	22	ETH-63365
GAEN0005	61.5	12804.5	2	4	10889	22	ETH-63366
GAEN0005	61.5	12804.5	2	4	10892	21	ETH-63366
GAEN0005	59.5	12806.5	2	4	10929	21	ETH-63367
GAEN0005	59.5	12806.5	2	4	10887	21	ETH-63367
GAEN0005	57.5	12808.5	2	4	10907	27	ETH-63368
GAEN0005	57.5	12808.5	2	4	10882	21	ETH-63368
GAEN0005	55.5	12810.5	2	4	10905	22	ETH-63369
GAEN0005	51.5	12814.5	2	4	10905	21	ETH-63371
GAEN0005	49.5	12816.5	2	4	10930	22	ETH-63372
GAEN0005	47.5	12818.5	2	4	10926	21	ETH-63373
GAEN0005	47.5	12818.5	2	4	10910	21	ETH-63373
GAEN0005	43.5	12822.5	2	4	10931	24	ETH-63375
GAEN0005	41.5	12824.5	2	4	10913	22	ETH-63376
GAEN0005	41.5	12824.5	2	4	10870	21	ETH-63376
GAEN0005	37.5	12828.5	2	4	10919	22	ETH-63378
GAEN0005	35.5	12830.5	2	4	10940	22	ETH-63379
GAEN0005	35.5	12830.5	2	4	10947	21	ETH-63379
GAEN0005	33.5	12832.5	2	4	10904	22	ETH-63380
GAEN0005	31.5	12834.5	2	4	10929	22	ETH-63381
GAEN0005	31.5	12834.5	2	4	10873	21	ETH-63381
GAEN0005	29.5	12836.5	2	4	10941	24	ETH-63382
GAEN0005	27.5	12838.5	2	4	10958	22	ETH-63383
GAEN0005	27.5	12838.5	2	4	10950	21	ETH-63383
GAEN0005	25.5	12840.5	2	4	10930	22	ETH-63384
GAEN0005	25.5	12840.5	2	4	10907	21	ETH-63384
GAEN0005	23.5	12842.5	2	4	10931	24	ETH-63385
GAEN0005	21.5	12844.5	2	4	10952	22	ETH-63386
GAEN0005	19.5	12846.5	2	4	10895	22	ETH-63387
GAEN0005	19.5	12846.5	2	4	10957	21	ETH-63387
GAEN0005	17.5	12848.5	2	4	10959	22	ETH-63388
GAEN0005	17.5	12848.5	2	4	10957	21	ETH-63388
GAEN0005	15.5	12850.5	2	4	10995	24	ETH-63389
GAEN0005	13.5	12852.5	2	4	11016	21	ETH-63390
GAEN0005	11.5	12854.5	2	4	10994	21	ETH-63391
GAEN0005	10	12856	1	4	10994	21	ETH-63392
GAEN0005	10	12856	1	4	10979	21	ETH-63392
GAEN0005	7.5	12858.5	2	4	10993	22	ETH-63393
GAEN0005	7.5	12858.5	2	4	10952	22	ETH-63393
GAEN0005	5	12861	3	4	10988	21	ETH-63394
GAEN0005	9	12857	1	4	11013	22	ETH-63399
GAEN0005	153.5	12712.5	2	4	10695	23	ETH-63698
GAEN0005	151.5	12714.5	2	4	10692	23	ETH-63699
GAEN0005	149.5	12716.5	2	4	10682	24	ETH-63700
GAEN0005	147.5	12718.5	2	4	10667	23	ETH-63701
GAEN0005	145.5	12720.5	2	4	10678	23	ETH-63702
GAEN0005	143.5	12722.5	2	4	10710	23	ETH-63703
GAEN0005	141.5	12724.5	2	4	10705	23	ETH-63704
GAEN0005	139.5	12726.5	2	4	10684	22	ETH-63705
GAEN0005	137.5	12728.5	2	4	10715	23	ETH-63706
GAEN0005	135.5	12730.5	2	4	10725	23	ETH-63707
GAEN0005	133.5	12732.5	2	4	10742	24	ETH-63708
GAEN0005	131.5	12734.5	2	4	10755	23	ETH-63709
GAEN0005	131.5	12734.5	2	4	10748	24	ETH-63709
GAEN0005	131.5	12734.5	2	4	10734	20	ETH-63709
GAEN0005	129.5	12736.5	2	4	10763	22	ETH-63710
GAEN0005	129.5	12736.5	2	4	10734	20	ETH-63710
GAEN0005	127.5	12738.5	2	4	10804	23	ETH-63711
GAEN0005	127.5	12738.5	2	4	10743	20	ETH-63711
GAEN0005	125.5	12740.5	2	4	10749	23	ETH-63712

GAEN0005	125.5	12740.5	2	4	10746	20	ETH-63712
GAEN0005	123.5	12742.5	2	4	10770	22	ETH-63713
GAEN0005	123.5	12742.5	2	4	10754	20	ETH-63713
GAEN0005	121.5	12744.5	2	4	10859	22	ETH-63714
GAEN0005	121.5	12744.5	2	4	10817	20	ETH-63714
GAEN0005	119.5	12746.5	2	4	10793	22	ETH-63715
GAEN0005	119.5	12746.5	2	4	10782	20	ETH-63715
GAEN0005	117.5	12748.5	2	4	10844	23	ETH-63716
GAEN0005	117.5	12748.5	2	4	10817	20	ETH-63716
GAEN0005	115.5	12750.5	2	4	10820	23	ETH-63717
GAEN0005	115.5	12750.5	2	4	10774	20	ETH-63717
GAEN0005	113.5	12752.5	2	4	10815	22	ETH-63718
GAEN0005	113.5	12752.5	2	4	10801	20	ETH-63718
GAEN0005	111.5	12754.5	2	4	10853	23	ETH-63719
GAEN0005	111.5	12754.5	2	4	10798	20	ETH-63719
GAEN0005	109.5	12756.5	2	4	10848	23	ETH-63720
GAEN0005	109.5	12756.5	2	4	10780	20	ETH-63720
GAEN0005	107.5	12758.5	2	4	10852	24	ETH-63721
GAEN0005	107.5	12758.5	2	4	10875	20	ETH-63721
GAEN0005	105.5	12760.5	2	4	10847	23	ETH-63722
GAEN0005	105.5	12760.5	2	4	10837	20	ETH-63722
GAEN0005	103.5	12762.5	2	4	10840	23	ETH-63723
GAEN0005	103.5	12762.5	2	4	10840	20	ETH-63723
GAEN0005	101.5	12764.5	2	4	10873	23	ETH-63724
GAEN0005	101.5	12764.5	2	4	10833	20	ETH-63724
GAEN0005	49.5	12766.5	2	4	10884	23	ETH-63725
GAEN0005	49.5	12766.5	2	4	10860	20	ETH-63725
GAEN0005	97.5	12768.5	2	4	10958	23	ETH-63726
GAEN0005	95.5	12770.5	2	4	10957	23	ETH-63727
GAEN0005	95.5	12770.5	2	4	10937	26	ETH-63727
GAEN0005	93.5	12772.5	2	4	10951	22	ETH-63728
GAEN0005	91.5	12774.5	2	4	10943	23	ETH-63729
GAEN0005	91.5	12774.5	2	4	10919	20	ETH-63729
GAEN0005	89.5	12776.5	2	4	10918	23	ETH-63730
GAEN0005	89.5	12776.5	2	4	10904	20	ETH-63730
GAEN0005	87.5	12778.5	2	4	10879	21	ETH-63731
GAEN0005	87.5	12778.5	2	4	10912	21	ETH-63731
GAEN0005	85.5	12780.5	2	4	10950	24	ETH-63732
GAEN0005	85.5	12780.5	2	4	10914	24	ETH-63732
GAEN0005	85.5	12780.5	2	4	10941	23	ETH-63732
GAEN0005	83.5	12782.5	2	4	10875	23	ETH-63733
GAEN0005	80.5	12785.5	4	4	10927	23	ETH-63735
GAEN0005	80.5	12785.5	4	4	10886	20	ETH-63735
GAEN0005	76.5	12789.5	4	4	10930	23	ETH-63737
GAEN0005	76.5	12789.5	4	4	10947	21	ETH-63737
GAEN0005	73.5	12792.5	2	4	10926	22	ETH-63738
GAEN0005	73.5	12792.5	2	4	10913	20	ETH-63738
GAEN0005	71.5	12794.5	2	4	10896	23	ETH-63739
GAEN0005	69.5	12796.5	2	4	10911	23	ETH-63740
GAEN0005	67.5	12798.5	2	4	10886	23	ETH-63741
GAEN0005	65.5	12800.5	2	4	10921	22	ETH-63742
GAEN0005	132	12734	1	4	10783	26	ETH-66808
GAEN0005	133	12733	1	4	10738	21	ETH-66809
GAEN0005	134	12732	1	4	10750	21	ETH-66810
GAEN0005	135	12731	1	4	10765	21	ETH-66811
GAEN0005	136.5	12729.5	2	4	10734	21	ETH-66812
GAEN0005	138.5	12727.5	2	4	10670	21	ETH-66813
GAEN0005	140.5	12725.5	2	4	10724	24	ETH-66814
GAEN0005	142.5	12723.5	2	4	10709	21	ETH-66815
GAEN0005	144.5	12721.5	2	4	10670	21	ETH-66816
GAEN0005	146.5	12719.5	2	4	10711	21	ETH-66817
GAEN0005	148.5	12717.5	2	4	10685	20	ETH-66818
GAEN0005	150.5	12715.5	2	4	10698	20	ETH-66819
GAEN0005	152.5	12713.5	2	4	10677	21	ETH-66820
GAEN0005	156	12710	1	4	10665	20	ETH-66822
GAEN0005	157	12709	1	4	10628	21	ETH-66823

GAEN0005	158.5	12707.5	2	4	10671	20	ETH-66824
GAEN0005	160	12706	1	4	10664	21	ETH-66825
GAEN0005	161	12705	1	4	10646	20	ETH-66826
GAEN0005	162	12704	1	4	10601	21	ETH-66827
GAEN0005	163	12703	1	4	10669	21	ETH-66828
GAEN0005	164	12702	1	4	10625	21	ETH-66829
GAEN0005	165.5	12700.5	2	4	10677	21	ETH-66830
GAEN0005	167	12699	1	4	10669	21	ETH-66831
GAEN0005	168	12698	1	4	10676	20	ETH-66832
GAEN0005	169	12697	1	4	10678	21	ETH-66833
GAEN0005	170	12696	1	4	10660	21	ETH-66834
GAEN0005	171	12695	1	4	10644	21	ETH-66835
GAEN0005	172	12694	1	4	10660	21	ETH-66836
GAEN0005	173	12693	1	4	10666	21	ETH-66837
GAEN0005	174	12692	1	4	10667	21	ETH-66838
GAEN0005	175	12691	1	4	10674	21	ETH-66839
GAEN0005	175	12691	1	4	10668	21	ETH-66839
GAEN0005	176	12690	1	4	10664	20	ETH-66840
GAEN0005	176	12690	1	4	10659	21	ETH-66840
GAEN0005	177.5	12688.5	2	4	10655	21	ETH-66841
GAEN0005	177.5	12688.5	2	4	10618	21	ETH-66841
GAEN0005	179.5	12686.5	2	4	10674	20	ETH-66842
GAEN0005	179.5	12686.5	2	4	10594	21	ETH-66842
GAEN0005	181.5	12684.5	2	4	10622	21	ETH-66843
GAEN0005	181.5	12684.5	2	4	10628	21	ETH-66843
GAEN0005	183.5	12682.5	2	4	10606	20	ETH-66844
GAEN0005	183.5	12682.5	2	4	10598	21	ETH-66844
GAEN0005	185.5	12680.5	2	4	10607	21	ETH-66845
GAEN0005	187.5	12678.5	2	4	10590	21	ETH-66846
GAEN0005	189.5	12676.5	2	4	10576	21	ETH-66847
GAEN0005	191.5	12674.5	2	4	10555	21	ETH-66849
GAEN0005	191.5	12674.5	2	4	10629	21	ETH-66849
GAEN0005	202.5	12663.5	4	4	10541	20	ETH-66854
GAEN0005	209.5	12656.5	2	4	10541	21	ETH-66857
GAEN0005	214	12652	3	4	10591	21	ETH-66859
GAEN0005	218	12648	5	4	10564	20	ETH-66860
GAEN0005	221.5	12644.5	2	4	10579	21	ETH-66861
GAEN0005	231.5	12634.5	4	4	10586	20	ETH-66864
BREI0232	14.5	12021.5	4	0	10309	24	ETH-65259
BREI0232	19	12017	5	0	10339	22	ETH-65260
BREI0232	23.5	12012.5	4	0	10280	21	ETH-65261
BREI0232	27	12009	3	0	10299	22	ETH-65262
BREI0232	27	12009	3	0	10321	22	ETH-65262
BREI0232	30.5	12005.5	4	0	10318	22	ETH-65263
BREI0232	30.5	12005.5	4	0	10327	21	ETH-65263
BREI0232	34	12002	3	0	10310	22	ETH-65264
BREI0232	34	12002	3	0	10338	22	ETH-65264
BREI0232	37	11999	3	0	10315	22	ETH-65265
BREI0232	37	11999	3	0	10343	21	ETH-65265
BREI0232	40.5	11995.5	4	0	10314	22	ETH-65266
BREI0232	40.5	11995.5	4	0	10316	22	ETH-65266
BREI0232	44	11992	3	0	10306	21	ETH-65267
BREI0232	47	11989	3	0	10310	22	ETH-65268
BREI0232	47	11989	3	0	10286	22	ETH-65268
BREI0232	50	11986	3	0	10265	22	ETH-65269
BREI0232	53	11983	3	0	10267	22	ETH-65270
BREI0232	53	11983	3	0	10315	22	ETH-65270
BREI0232	56	11980	3	0	10288	22	ETH-65271
BREI0232	59.5	11976.5	4	0	10353	23	ETH-65272
BREI0232	59.5	11976.5	4	0	10328	22	ETH-65272
BREI0232	64	11972	5	0	10319	21	ETH-65273
BREI0232	69	11967	5	0	10288	22	ETH-65274
BREI0232	69	11967	5	0	10305	22	ETH-65274
BREI0232	79.5	11956.5	6	0	10297	22	ETH-65276
BREI0232	84	11952	3	0	10266	22	ETH-65277
BREI0232	84	11952	3	0	10296	22	ETH-65277

BREI0232	87	11949	3	0	10290	22	ETH-65278
BREI0232	87	11949	3	0	10245	22	ETH-65278
BREI0232	90	11946	3	0	10279	22	ETH-65279
BREI0232	93	11943	3	0	10246	22	ETH-65280
BREI0232	93	11943	3	0	10277	21	ETH-65280
BREI0232	96	11940	3	0	10218	21	ETH-65281
BREI0232	49.5	11936.5	4	0	10263	21	ETH-65282
BREI0232	104	11932	5	0	10217	22	ETH-65283
BREI0232	109	11927	5	0	10202	22	ETH-65284
BREI0232	109	11927	5	0	10221	22	ETH-65284
BREI0232	114	11922	5	0	10243	22	ETH-65285
BREI0232	119	11917	5	0	10224	22	ETH-65286
BREI0232	124	11912	5	0	10238	21	ETH-65287
BREI0232	129	11907	5	0	10255	22	ETH-65288
BREI0232	134	11902	5	0	10223	22	ETH-65289
BREI0232	139	11897	5	0	10219	22	ETH-65290
BREI0232	144	11892	5	0	10242	22	ETH-65291
BREI0232	149	11887	5	0	10250	22	ETH-65292
BREI0232	149	11887	5	0	10266	22	ETH-65292
GAEN0027	23.5	12652.5	2	4	10573	22	ETH-66392
GAEN0027	25	12651	1	4	10609	22	ETH-66393
GAEN0027	26	12650	1	4	10566	23	ETH-66394
GAEN0027	27	12649	1	4	10574	23	ETH-66395
GAEN0027	28	12648	1	4	10628	23	ETH-66396
GAEN0027	29	12647	1	4	10619	23	ETH-66397
GAEN0027	31	12645	1	4	10619	23	ETH-66399
GAEN0027	32	12644	1	4	10633	23	ETH-66400
GAEN0027	33	12643	1	4	10633	23	ETH-66401
GAEN0027	37	12639	1	4	10604	22	ETH-66402
GAEN0027	38	12638	1	4	10621	22	ETH-66403
GAEN0027	39	12637	1	4	10624	23	ETH-66404
GAEN0027	40	12636	1	4	10625	22	ETH-66405
GAEN0027	41	12635	1	4	10588	22	ETH-66406
GAEN0027	42	12634	1	4	10636	23	ETH-66407
GAEN0027	43	12633	1	4	10608	22	ETH-66408
GAEN0027	44	12632	1	4	10638	22	ETH-66409
GAEN0027	45	12631	1	4	10607	23	ETH-66410
GAEN0027	46	12630	1	4	10617	22	ETH-66411
GAEN0027	47	12629	1	4	10604	22	ETH-66412
GAEN0027	49	12627	1	4	10589	22	ETH-66414
GAEN0027	50	12626	1	4	10620	22	ETH-66415
GAEN0027	51	12625	1	4	10565	21	ETH-66424
GAEN0027	52	12624	1	4	10540	25	ETH-66425
GAEN0027	53	12623	1	4	10574	22	ETH-66426
GAEN0027	54.5	12621.5	2	4	10579	23	ETH-66428
GAEN0027	56	12620	1	4	10562	21	ETH-66429
GAEN0027	57	12619	1	4	10572	21	ETH-66430
GAEN0027	58	12618	1	4	10585	21	ETH-66431
GAEN0027	59	12617	1	4	10572	22	ETH-66432
GAEN0027	60	12616	1	4	10538	21	ETH-66433
GAEN0027	61	12615	1	4	10548	21	ETH-66434
GAEN0027	62	12614	1	4	10547	21	ETH-66435
GAEN0027	63	12613	1	4	10523	21	ETH-66436
GAEN0027	64	12612	1	4	10531	21	ETH-66437
GAEN0027	65	12611	1	4	10527	21	ETH-66438
GAEN0027	66	12610	1	4	10523	23	ETH-66439
GAEN0027	67	12609	1	4	10512	21	ETH-66440
GAEN0027	68	12608	1	4	10488	20	ETH-66441
GAEN0027	69	12607	1	4	10553	21	ETH-66442
GAEN0027	70	12606	1	4	10511	20	ETH-66443
GAEN0027	71	12605	1	4	10510	22	ETH-66444
GAEN0027	72	12604	1	4	10495	21	ETH-66445
GAEN0027	73	12603	1	4	10528	20	ETH-66446
GAEN0027	74	12602	1	4	10556	24	ETH-66447
GAEN0027	75	12601	1	4	10496	21	ETH-66448
GAEN0027	76	12600	1	4	10534	22	ETH-66473

GAEN0027	77	12599	1	4	10535	21	ETH-66474
GAEN0027	78	12598	1	4	10498	25	ETH-66475
GAEN0027	79	12597	1	4	10528	22	ETH-66476
GAEN0027	80	12596	1	4	10527	22	ETH-66477
GAEN0027	81	12595	1	4	10512	22	ETH-66478
GAEN0027	82	12594	1	4	10480	25	ETH-66479
GAEN0027	83	12593	1	4	10488	23	ETH-66480
GAEN0027	84	12592	1	4	10493	26	ETH-66481
GAEN0027	85	12591	1	4	10471	27	ETH-66482
GAEN0027	86	12590	1	4	10500	23	ETH-66483
GAEN0027	87	12589	1	4	10536	27	ETH-66484
GAEN0027	88	12588	1	4	10518	28	ETH-66485
GAEN0027	89	12587	1	4	10458	26	ETH-66486
GAEN0027	90	12586	1	4	10518	20	ETH-66487
GAEN0027	91	12585	1	4	10440	24	ETH-66488
GAEN0027	92	12584	1	4	10478	26	ETH-66489
GAEN0027	93	12583	1	4	10470	23	ETH-66490
GAEN0027	94	12582	1	4	10490	23	ETH-66491
GAEN0027	95	12581	1	4	10488	23	ETH-66492
GAEN0027	96	12580	1	4	10502	21	ETH-67166
GAEN0027	97	12579	1	4	10464	22	ETH-67167
GAEN0027	98	12578	1	4	10474	22	ETH-67168
GAEN0027	99	12577	1	4	10512	22	ETH-67169
GAEN0027	100	12576	1	4	10505	21	ETH-67170
GAEN0027	101	12575	1	4	10520	21	ETH-67171
GAEN0027	102	12574	1	4	10471	22	ETH-67172
GAEN0027	103	12573	1	4	10525	21	ETH-67173
GAEN0027	104	12572	1	4	10487	21	ETH-67174
GAEN0027	106	12570	1	4	10496	21	ETH-68048
GAEN0027	107	12569	1	4	10487	21	ETH-68049
GAEN0027	108	12568	1	4	10472	22	ETH-68050
GAEN0027	109	12567	1	4	10475	22	ETH-68051
GAEN0027	110	12566	1	4	10471	21	ETH-68052
GAEN0027	111	12565	1	4	10481	21	ETH-68053
GAEN0027	112	12564	1	4	10458	21	ETH-68054
GAEN0027	113	12563	1	4	10458	21	ETH-68055
GAEN0027	114	12562	1	4	10461	22	ETH-68056
GAEN0027	115	12561	1	4	10503	22	ETH-68057
GAEN0027	116	12560	1	4	10424	24	ETH-68095
GAEN0027	116	12560	1	4	10458	24	ETH-68095
GAEN0027	117	12559	1	4	10511	24	ETH-68096
GAEN0027	118	12558	1	4	10475	21	ETH-68097
GAEN0027	119	12557	1	4	10433	24	ETH-68098
GAEN0027	119	12557	1	4	10517	24	ETH-68098
GAEN0027	120	12556	1	4	10414	25	ETH-68099
GAEN0027	120	12556	1	4	10472	24	ETH-68099
GAEN0027	121	12555	1	4	10478	24	ETH-68100
GAEN0027	121	12555	1	4	10471	24	ETH-68100
GAEN0027	122	12554	1	4	10447	21	ETH-68101
GAEN0027	123	12553	1	4	10489	21	ETH-68102
GAEN0027	123	12553	1	4	10445	24	ETH-68102
GAEN0027	124	12552	1	4	10422	24	ETH-68103
GAEN0027	124	12552	1	4	10445	24	ETH-68103
GAEN0027	125	12551	1	4	10473	21	ETH-68104
GAEN0027	126	12550	1	4	10509	24	ETH-68105
GAEN0027	128	12548	1	4	10467	24	ETH-68107
GAEN0027	133	12543	1	4	10491	21	ETH-68112
GAEN0102	26	12631	1	4	10560	24	ETH-68120
GAEN0102	26	12631	1	4	10570	24	ETH-68120
GAEN0102	27	12630	1	4	10622	24	ETH-68121
GAEN0102	28	12629	1	4	10617	21	ETH-68122
GAEN0102	29	12628	1	4	10617	24	ETH-68123
GAEN0102	30	12627	1	4	10560	24	ETH-68124
GAEN0102	30	12627	1	4	10589	24	ETH-68124
GAEN0102	31	12626	1	4	10630	21	ETH-68125
GAEN0102	32	12625	1	4	10589	22	ETH-68126

GAEN0102	33	12624	1	4	10575	24	ETH-68127
GAEN0102	34	12623	1	4	10607	22	ETH-68128
GAEN0102	35	12622	1	4	10568	24	ETH-68129
GAEN0102	36	12621	1	4	10596	24	ETH-68130
GAEN0102	37	12620	1	4	10568	24	ETH-68131
GAEN0102	38	12619	1	4	10590	21	ETH-68132
GAEN0102	39	12618	1	4	10543	24	ETH-68133
GAEN0102	39	12618	1	4	10541	24	ETH-68133
GAEN0102	40	12617	1	4	10565	22	ETH-68134
GAEN0102	41	12616	1	4	10556	21	ETH-68135
GAEN0102	42	12615	1	4	10513	21	ETH-68136
GAEN0102	43	12614	1	4	10538	21	ETH-68137
GAEN0102	44	12613	1	4	10533	22	ETH-68138
GAEN0102	45	12612	1	4	10567	24	ETH-68139
GAEN0102	46	12611	1	4	10483	21	ETH-68140
GAEN0102	47	12610	1	4	10506	21	ETH-68141
GAEN0102	48	12609	1	4	10548	21	ETH-68142
GAEN0102	49	12608	1	4	10497	24	ETH-68143
GAEN0102	50	12607	1	4	10505	21	ETH-68144
GAEN0102	51	12606	1	4	10545	21	ETH-68145
GAEN0102	52	12605	1	4	10481	21	ETH-68381
GAEN0102	53	12604	1	4	10507	21	ETH-68382
GAEN0102	54	12603	1	4	10523	21	ETH-68383
GAEN0102	55	12602	1	4	10472	21	ETH-68384
GAEN0102	56	12601	1	4	10513	21	ETH-68385
GAEN0102	57	12600	1	4	10482	21	ETH-68386
GAEN0102	58	12599	1	4	10525	22	ETH-68786
GAEN0102	59	12598	1	4	10501	21	ETH-68787
GAEN0102	60	12597	1	4	10514	22	ETH-68788
GAEN0102	61	12596	1	4	10540	23	ETH-68789
GAEN0102	62	12595	1	4	10482	21	ETH-68790
GAEN0102	63	12594	1	4	10555	22	ETH-68791
GAEN0102	64	12593	1	4	10504	21	ETH-68792
GAEN0102	65	12592	1	4	10485	21	ETH-68793
GAEN0102	66	12591	1	4	10508	22	ETH-68794
GAEN0102	67	12590	1	4	10477	21	ETH-68795
GAEN0102	68	12589	1	4	10483	22	ETH-68796
GAEN0102	69	12588	1	4	10494	22	ETH-68797
GAEN0102	70	12587	1	4	10482	21	ETH-68798
GAEN0102	71	12586	1	4	10462	21	ETH-68799
GAEN0102	72	12585	1	4	10458	22	ETH-68800
GAEN0102	73	12584	1	4	10470	24	ETH-68801
GAEN0102	74	12583	1	4	10435	21	ETH-68802
GAEN0102	75	12582	1	4	10525	21	ETH-68803
GAEN0102	76	12581	1	4	10455	21	ETH-68804
GAEN0102	77	12580	1	4	10465	21	ETH-68805
GAEN0102	78	12579	1	4	10484	21	ETH-68806
GAEN0102	79	12578	1	4	10445	21	ETH-68807
GAEN0102	80	12577	1	4	10511	21	ETH-68808
GAEN0102	81	12576	1	4	10445	21	ETH-68809
GAEN0102	82	12575	1	4	10470	21	ETH-68810
GAEN0102	83	12574	1	4	10480	21	ETH-68811
GAEN0102	84	12573	1	4	10458	22	ETH-68812
GAEN0102	85	12572	1	4	10454	21	ETH-68813
GAEN0102	86	12571	1	4	10482	21	ETH-68814
GAEN0102	87	12570	1	4	10492	23	ETH-68815
GAEN0102	88	12569	1	4	10479	22	ETH-68816
GAEN0102	89	12568	1	4	10468	21	ETH-68817
GAEN0102	90	12567	1	4	10448	22	ETH-68818
GAEN0102	91	12566	1	4	10490	22	ETH-68819
GAEN0102	92	12565	1	4	10413	21	ETH-68820
GAEN0102	93	12564	1	4	10477	21	ETH-68821
GAEN0102	94	12563	1	4	10521	21	ETH-68822
GAEN0102	95	12562	1	4	10451	21	ETH-68823
GAEN0102	96	12561	1	4	10516	21	ETH-68824
GAEN0102	97	12560	1	4	10459	21	ETH-68825

GAEN0102	98	12559	1	4	10489	21	ETH-68826
GAEN0102	99	12558	1	4	10480	21	ETH-68827
GAEN0102	100	12557	1	4	10483	21	ETH-68828
GAEN0102	101	12556	1	4	10524	22	ETH-68829
GAEN0102	102	12555	1	4	10437	21	ETH-68830
GAEN0102	103	12554	1	4	10467	24	ETH-68831
GAEN0102	104	12553	1	4	10439	21	ETH-68832
GAEN0102	105	12552	1	4	10530	21	ETH-68833
GAEN0102	106	12551	1	4	10501	21	ETH-68834
GAEN0102	107	12550	1	4	10525	22	ETH-68835
GAEN0102	108	12549	1	4	10511	21	ETH-68836
GAEN0102	109	12548	1	4	10498	21	ETH-68837
GAEN0102	110	12547	1	4	10456	21	ETH-68838
GAEN0102	111	12546	1	4	10514	21	ETH-68839
BINZ0026	21	12628	1	4	10614	21	ETH-69725
BINZ0026	22	12627	1	4	10585	21	ETH-69726
BINZ0026	24	12625	1	4	10589	21	ETH-69728
BINZ0026	25	12624	1	4	10517	24	ETH-69729
BINZ0026	26	12623	1	4	10568	21	ETH-69730
BINZ0026	27	12622	1	4	10514	24	ETH-69731
BINZ0026	28	12621	1	4	10555	21	ETH-69732
BINZ0026	29	12620	1	4	10472	24	ETH-69733
BINZ0026	30	12619	1	4	10533	21	ETH-69734
BINZ0026	31	12618	1	4	10498	23	ETH-69735
BINZ0026	32	12617	1	4	10557	21	ETH-69736
BINZ0026	33	12616	1	4	10539	24	ETH-69737
BINZ0026	34	12615	1	4	10526	21	ETH-69738
BINZ0026	35	12614	1	4	10512	24	ETH-69739
BINZ0026	36	12613	1	4	10465	21	ETH-69740
BINZ0026	37	12612	1	4	10523	20	ETH-69741
BINZ0026	38	12611	1	4	10510	21	ETH-69742
BINZ0026	39	12610	1	4	10468	24	ETH-69743
BINZ0026	40	12609	1	4	10507	21	ETH-69744
BINZ0026	41	12608	1	4	10482	24	ETH-69745
BINZ0026	42	12607	1	4	10505	21	ETH-69746
BINZ0026	43	12606	1	4	10494	24	ETH-69747
BINZ0026	44	12605	1	4	10502	21	ETH-69748
BINZ0026	45	12604	1	4	10491	24	ETH-69749
BINZ0026	46	12603	1	4	10496	21	ETH-69750
BINZ0026	47	12602	1	4	10496	24	ETH-69751
BINZ0026	48	12601	1	4	10472	21	ETH-69752
BINZ0026	49	12600	1	4	10493	22	ETH-69753
BINZ0026	50	12599	1	4	10515	21	ETH-69754
BINZ0026	51	12598	1	4	10451	24	ETH-69755
BINZ0026	52	12597	1	4	10491	22	ETH-69756
BINZ0026	53	12596	1	4	10526	20	ETH-69757
BINZ0026	54	12595	1	4	10492	22	ETH-69758
BINZ0026	55	12594	1	4	10498	24	ETH-69759
BINZ0026	56	12593	1	4	10487	22	ETH-69760
BINZ0026	57	12592	1	4	10452	24	ETH-69761
BINZ0026	58	12591	1	4	10465	22	ETH-69762
BINZ0026	59	12590	1	4	10485	24	ETH-69763
BINZ0026	60	12589	1	4	10471	22	ETH-69764
BINZ0026	61	12588	1	4	10454	24	ETH-69765
BINZ0026	62	12587	1	4	10455	22	ETH-69766
BINZ0026	63	12586	1	4	10455	24	ETH-69767
BINZ0026	64	12585	1	4	10470	22	ETH-69768
BINZ0026	65	12584	1	4	10479	24	ETH-69769
BINZ0026	66	12583	1	4	10474	22	ETH-69770
BINZ0026	67	12582	1	4	10446	21	ETH-69771
BINZ0026	68	12581	1	4	10506	22	ETH-69772
BINZ0026	69	12580	1	4	10474	22	ETH-69773
BINZ0026	70	12579	1	4	10467	22	ETH-69774
BINZ0026	71	12578	1	4	10458	24	ETH-69775
BINZ0026	72	12577	1	4	10416	22	ETH-69776
BINZ0026	73	12576	1	4	10453	24	ETH-69777

BINZ0026	74	12575	1	4	10446	22	ETH-69778
BINZ0026	75	12574	1	4	10417	21	ETH-69779
BINZ0026	76	12573	1	4	10456	22	ETH-69780
BINZ0026	77	12572	1	4	10458	24	ETH-69781
BINZ0026	78	12571	1	4	10450	22	ETH-69782
BINZ0026	79	12570	1	4	10465	24	ETH-69783
BINZ0026	80	12569	1	4	10478	22	ETH-69784
BINZ0026	81	12568	1	4	10470	24	ETH-69785
BINZ0026	82	12567	1	4	10468	22	ETH-69786
BINZ0026	83	12566	1	4	10431	24	ETH-69787
BINZ0026	84	12565	1	4	10467	22	ETH-69788
BINZ0026	85	12564	1	4	10468	24	ETH-69789
BINZ0026	86	12563	1	4	10486	22	ETH-69790
BINZ0026	87	12562	1	4	10478	23	ETH-69791
BINZ0026	89	12560	1	4	10491	23	ETH-69793
BINZ0026	90	12559	1	4	10477	21	ETH-69794
BINZ0026	91	12558	1	4	10455	23	ETH-69795
BINZ0026	92	12557	1	4	10447	22	ETH-69796
BINZ0026	93	12556	1	4	10459	23	ETH-69797
BINZ0026	94	12555	1	4	10444	19	ETH-69798
BINZ0026	95	12554	1	4	10481	23	ETH-69799
BINZ0026	96	12553	1	4	10501	22	ETH-69800
BINZ0026	97	12552	1	4	10429	21	ETH-69801
BINZ0026	98	12551	1	4	10467	22	ETH-69802
BINZ0026	99	12550	1	4	10513	23	ETH-69803
BINZ0026	100	12549	1	4	10482	21	ETH-69804
BINZ0026	101	12548	1	4	10515	23	ETH-69805
BINZ0026	102	12547	1	4	10500	21	ETH-69806
BINZ0026	103	12546	1	4	10505	23	ETH-69807
BINZ0026	104	12545	1	4	10521	21	ETH-69808
BINZ0026	105	12544	1	4	10505	23	ETH-69809
BINZ0026	106	12543	1	4	10539	21	ETH-69810
BINZ0026	107	12542	1	4	10554	23	ETH-69811
BINZ0026	108	12541	1	4	10504	21	ETH-69812
BINZ0026	109	12540	1	4	10534	23	ETH-69813
BINZ0026	110	12539	1	4	10494	22	ETH-69814
BINZ0026	111	12538	1	4	10558	23	ETH-69815
BINZ0026	112	12537	1	4	10535	21	ETH-69816
BINZ0026	113	12536	1	4	10492	23	ETH-69817
BINZ0026	114	12535	1	4	10533	21	ETH-69818
BINZ0026	115	12534	1	4	10546	23	ETH-69819
BINZ0026	116	12533	1	4	10532	22	ETH-69820
BINZ0026	117	12532	1	4	10541	23	ETH-69821
BINZ0026	118	12531	1	4	10556	22	ETH-69822
BINZ0026	119	12530	1	4	10540	23	ETH-69823
BINZ0026	120	12529	1	4	10535	21	ETH-69824
COTT0418	32.5	12165.5	2	0	10350	22	ETH-70509
COTT0418	34.5	12163.5	2	0	10382	21	ETH-70510
COTT0418	36.5	12161.5	2	0	10375	21	ETH-70511
COTT0418	38.5	12159.5	2	0	10301	22	ETH-70512
COTT0418	40.5	12157.5	2	0	10327	22	ETH-70513
COTT0418	42.5	12155.5	2	0	10345	22	ETH-70514
COTT0418	45	12153	3	0	10356	22	ETH-70515
COTT0418	48	12150	3	0	10332	22	ETH-70516
COTT0418	51	12147	3	0	10367	22	ETH-70517
COTT0418	54.5	12143.5	4	0	10363	22	ETH-70518
COTT0418	59	12139	5	0	10346	22	ETH-70519
COTT0418	63.5	12134.5	4	0	10344	22	ETH-70520
COTT0418	67	12131	3	0	10365	21	ETH-70521
COTT0418	70.5	12127.5	4	0	10323	22	ETH-70522
COTT0418	74	12124	3	0	10323	22	ETH-70523
COTT0418	77.5	12120.5	4	0	10348	21	ETH-70524
COTT0418	81	12117	3	0	10325	21	ETH-70525
COTT0418	84	12114	3	0	10388	21	ETH-70526
COTT0418	87.5	12110.5	4	0	10370	21	ETH-70527
COTT0418	91	12107	3	0	10395	21	ETH-70528

COTT0418	94	12104	3	0	10366	22	ETH-70529
COTT0418	97	12101	3	0	10379	22	ETH-70530
COTT0418	50	12098	3	0	10336	22	ETH-70531
COTT0418	102.5	12095.5	2	0	10338	21	ETH-70532
COTT0418	104.5	12093.5	2	0	10290	21	ETH-70533
COTT0418	106.5	12091.5	2	0	10327	21	ETH-70534
COTT0418	108.5	12089.5	2	0	10321	21	ETH-70535
COTT0418	110.5	12087.5	2	0	10323	21	ETH-70536
COTT0418	112.5	12085.5	2	0	10339	21	ETH-70537
COTT0418	114.5	12083.5	2	0	10355	21	ETH-70538
COTT0418	117	12081	3	0	10359	21	ETH-70539
COTT0418	122	12076	7	0	10342	22	ETH-70540
COTT0418	127	12071	3	0	10348	21	ETH-70541
COTT0418	131	12067	5	0	10317	21	ETH-70542
COTT0418	135.5	12062.5	4	0	10357	21	ETH-70543
COTT0418	140	12058	5	0	10299	21	ETH-70544
COTT0418	147	12051	9	0	10347	21	ETH-70545
COTT0418	154	12044	5	0	10338	21	ETH-70546
COTT0418	158.5	12039.5	4	0	10324	21	ETH-70547
COTT0418	165	12033	9	0	10322	21	ETH-70548
COTT0418	172	12026	5	0	10314	21	ETH-70549
COTT0418	176	12022	3	0	10338	22	ETH-70550
COTT0418	179.5	12018.5	4	0	10298	21	ETH-70551
COTT0418	184	12014	5	0	10348	21	ETH-70552
COTT0418	189	12009	5	0	10342	21	ETH-70553
COTT0418	193	12005	3	0	10329	22	ETH-70554
COTT0418	196	12002	3	0	10292	21	ETH-70555
COTT0418	199	11999	3	0	10272	22	ETH-70556
BINZ0073	41.5	12571.5	2	4	10468	21	ETH-71460
BINZ0073	43.5	12569.5	2	4	10472	21	ETH-71461
BINZ0073	45	12568	1	4	10471	21	ETH-71462
BINZ0073	46.5	12566.5	2	4	10484	21	ETH-71463
BINZ0073	48	12565	1	4	10467	21	ETH-71464
BINZ0073	49	12564	1	4	10471	21	ETH-71465
BINZ0073	50	12563	1	4	10472	21	ETH-71466
BINZ0073	51	12562	1	4	10449	21	ETH-71467
BINZ0073	52.5	12560.5	2	4	10496	21	ETH-71468
BINZ0073	54.5	12558.5	2	4	10461	21	ETH-71469
BINZ0073	56.5	12556.5	2	4	10460	21	ETH-71470
BINZ0073	58.5	12554.5	2	4	10479	21	ETH-71471
BINZ0073	60.5	12552.5	2	4	10463	21	ETH-71472
BINZ0073	63	12551	3	4	10498	21	ETH-71473
BINZ0073	66	12547	3	4	10504	21	ETH-71474
BINZ0073	68.5	12544.5	2	4	10500	20	ETH-73306
BINZ0073	70.5	12542.5	2	4	10523	20	ETH-73307
BINZ0073	72.5	12540.5	2	4	10519	21	ETH-73308
BINZ0073	74.5	12538.5	2	4	10549	20	ETH-73309
BINZ0073	76.5	12536.5	2	4	10566	20	ETH-73310
BINZ0073	78.5	12534.5	2	4	10553	20	ETH-73311
BINZ0073	80.5	12532.5	2	4	10545	20	ETH-73312
BINZ0073	82.5	12530.5	2	4	10597	20	ETH-73313
BINZ0073	84.5	12528.5	2	4	10578	21	ETH-73314
BINZ0073	86.5	12526.5	2	4	10576	21	ETH-73315
BINZ0073	89	12524	3	4	10567	22	ETH-73316
BINZ0073	91.5	12521.5	2	4	10586	21	ETH-73317
BINZ0073	93.5	12519.5	2	4	10579	21	ETH-73318
BINZ0073	95.5	12517.5	2	4	10564	21	ETH-73319
BINZ0073	98	12515	3	4	10522	21	ETH-73320
BINZ0073	98	12515	3	4	10552	20	ETH-73320
BINZ0073	100.5	12512.5	2	4	10555	21	ETH-73321
BINZ0073	102.5	12510.5	2	4	10566	21	ETH-73322
BINZ0073	104.5	12508.5	2	4	10560	21	ETH-73323
BINZ0073	106.5	12506.5	2	4	10589	20	ETH-73324
BINZ0073	108.5	12504.5	2	4	10540	21	ETH-73325
BINZ0073	110.5	12502.5	2	4	10546	22	ETH-73326
BINZ0073	112.5	12500.5	2	4	10540	23	ETH-73327

BINZ0073	114.5	12498.5	2	4	10522	21	ETH-73328
BINZ0073	116.5	12496.5	2	4	10523	23	ETH-73329
BINZ0073	118.5	12494.5	2	4	10483	21	ETH-73330
BINZ0073	120.5	12492.5	2	4	10475	21	ETH-73331
BINZ0073	122.5	12490.5	2	4	10514	21	ETH-73332
BINZ0073	124.5	12488.5	2	4	10503	21	ETH-73333
BINZ0073	126.5	12486.5	2	4	10469	21	ETH-73334
BINZ0073	128.5	12484.5	2	4	10494	21	ETH-73335
BINZ0073	131	12482	3	4	10473	21	ETH-73336
BINZ0073	134	12479	3	4	10433	21	ETH-73337
BINZ0073	137.5	12475.5	4	4	10413	22	ETH-73338
BINZ0073	141.5	12471.5	4	4	10400	21	ETH-73339
BINZ0073	146	12467.5	4	4	10412	21	ETH-73340
BINZ0073	161.5	12451.5	6	4	10386	21	ETH-73341
BINZ0073	167.5	12445.5	6	4	10372	21	ETH-73342
BINZ0073	172	12441	3	4	10378	22	ETH-73343
BINZ0073	176	12437	5	4	10382	22	ETH-73344
BINZ0073	180	12433	3	4	10364	23	ETH-73345
BINZ0073	182.5	12430.5	2	4	10353	22	ETH-73346
BINZ0073	186	12427	5	4	10369	22	ETH-73347
BINZ0073	189.5	12423.5	2	4	10344	23	ETH-73348
BINZ0073	192.5	12420.5	4	4	10349	22	ETH-73349
BINZ0073	195.5	12417.5	2	4	10324	22	ETH-73350
BINZ0073	197.5	12415.5	2	4	10315	23	ETH-73351
BINZ0073	197.5	12415.5	2	4	10401	21	ETH-73351
BINZ0073	199.5	12413.5	2	4	10358	21	ETH-73352
BINZ0073	201.5	12411.5	2	4	10361	20	ETH-73353
BINZ0073	204	12409	3	4	10344	20	ETH-73354
BINZ0073	206.5	12406.5	2	4	10311	20	ETH-73355
BINZ0073	209	12404	3	4	10362	21	ETH-73356
BINZ0073	211.5	12401.5	2	4	10359	21	ETH-73357
BINZ0073	214	12399	3	4	10362	22	ETH-73358
BINZ0073	216.5	12396.5	2	4	10374	20	ETH-73359
BINZ0073	216.5	12396.5	2	4	10346	22	ETH-73359
BINZ0073	218.5	12394.5	2	4	10381	20	ETH-73360
BINZ0073	218.5	12394.5	2	4	10416	22	ETH-73360
BINZ0073	220.5	12392.5	2	4	10401	21	ETH-73361
BINZ0073	220.5	12392.5	2	4	10415	22	ETH-73361
BINZ0073	222.5	12390.5	2	4	10406	22	ETH-73362
BINZ0073	224.5	12388.5	2	4	10325	20	ETH-73363
BINZ0073	224.5	12388.5	2	4	10341	22	ETH-73363
BINZ0073	226.5	12386.5	2	4	10419	23	ETH-73364
BINZ0073	226.5	12386.5	2	4	10381	22	ETH-73364
BINZ0073	228.5	12384.5	2	4	10360	21	ETH-73365
BINZ0073	228.5	12384.5	2	4	10391	22	ETH-73365
BINZ0073	230.5	12382.5	2	4	10372	21	ETH-73366
BINZ0073	230.5	12382.5	2	4	10388	22	ETH-73366
BINZ0073	232.5	12380.5	2	4	10351	20	ETH-73367
BINZ0073	234.5	12378.5	2	4	10368	21	ETH-73368
BINZ0073	236.5	12376.5	2	4	10392	21	ETH-73369
BINZ0073	238.5	12374.5	2	4	10368	20	ETH-73370
BINZ0073	240.5	12372.5	2	4	10395	20	ETH-73371
BINZ0073	242.5	12370.5	2	4	10393	21	ETH-73372
BINZ0073	244.5	12368.5	2	4	10391	21	ETH-73373
BINZ0073	154	12459	3	4	10394	23	ETH-73374
BINZ0073	150	12463	3	4	10401	22	ETH-73375
BINZ0073	157	12456	3	4	10342	22	ETH-73376
BINZ0073	157	12456	3	4	10367	21	ETH-73376
GAEN0008	2.5	12703.5	4	4	10654	23	ETH-73751
GAEN0008	5	12701	1	4	10639	22	ETH-73752
GAEN0008	6.5	12699.5	2	4	10645	23	ETH-73753
GAEN0008	9	12697	3	4	10628	23	ETH-73754
GAEN0008	11	12695	1	4	10637	23	ETH-73755
GAEN0008	11	12695	1	4	10591	23	ETH-73755
GAEN0008	12	12694	1	4	10610	23	ETH-73756
GAEN0008	13	12693	1	4	10643	23	ETH-73757

GAEN0008	14	12692	1	4	10627	23	ETH-73758
GAEN0008	15	12691	1	4	10618	23	ETH-73759
GAEN0008	16	12690	1	4	10622	23	ETH-73760
GAEN0008	16	12690	1	4	10618	23	ETH-73760
GAEN0008	17	12689	1	4	10652	23	ETH-73761
GAEN0008	20.5	12685.5	2	4	10625	23	ETH-73763
GAEN0008	22.5	12683.5	2	4	10629	23	ETH-73764
GAEN0008	25	12681	3	4	10609	23	ETH-73765
GAEN0008	25	12681	3	4	10583	23	ETH-73765
GAEN0008	27.5	12683.5	2	4	10566	23	ETH-73766
GAEN0008	29	12677	1	4	10577	23	ETH-73767
GAEN0008	30.5	12675.5	2	4	10598	24	ETH-73768
GAEN0008	32.5	12673.5	2	4	10615	24	ETH-73769
GAEN0008	34.5	12671.5	2	4	10615	23	ETH-73770
GAEN0008	36.5	12669.5	2	4	10592	24	ETH-73771
GAEN0008	38	12668	1	4	10596	23	ETH-73772
GAEN0008	39	12667	1	4	10572	23	ETH-73773
GAEN0008	40	12666	1	4	10572	23	ETH-73774
GAEN0008	41	12665	1	4	10609	23	ETH-73775
GAEN0008	42	12664	1	4	10610	23	ETH-73776
GAEN0008	43	12663	1	4	10590	22	ETH-73777
GAEN0008	44	12662	1	4	10604	23	ETH-73778
GAEN0008	45	12661	1	4	10563	23	ETH-73779
GAEN0008	46	12660	1	4	10596	24	ETH-73780
GAEN0008	47	12659	1	4	10546	23	ETH-73781
GAEN0008	48	12658	1	4	10541	22	ETH-73782
GAEN0008	49	12657	1	4	10570	23	ETH-73783
GAEN0008	50	12656	1	4	10577	23	ETH-73784
GAEN0008	51	12655	1	4	10580	23	ETH-73785
GAEN0008	52	12654	1	4	10565	23	ETH-73786
GAEN0008	53	12653	1	4	10566	23	ETH-73787
GAEN0008	54	12652	1	4	10625	23	ETH-73788
GAEN0008	54	12652	1	4	10562	21	ETH-73788
GAEN0008	55	12651	1	4	10576	24	ETH-73789
GAEN0008	56	12650	1	4	10591	22	ETH-73790
GAEN0008	57	12649	1	4	10563	22	ETH-73791
GAEN0008	58	12648	1	4	10600	22	ETH-73792
GAEN0008	59	12647	1	4	10566	22	ETH-73793
GAEN0008	60	12646	1	4	10600	22	ETH-73794
GAEN0008	61	12645	1	4	10587	22	ETH-73795
GAEN0008	62	12644	1	4	10557	23	ETH-73796
GAEN0008	62	12644	1	4	10539	23	ETH-73796
GAEN0008	63	12643	1	4	10619	23	ETH-73797
GAEN0008	64	12642	1	4	10604	23	ETH-73798
GAEN0008	65	12641	1	4	10555	23	ETH-73799
GAEN0008	66	12640	1	4	10613	22	ETH-73800
GAEN0008	67	12639	1	4	10608	23	ETH-73811
GAEN0008	68	12638	1	4	10553	24	ETH-74375
GAEN0008	68	12638	1	4	10572	20	ETH-74375
GAEN0008	84	12622	1	4	10579	23	ETH-74391
GAEN0008	94	12612	1	4	10511	21	ETH-74401
GAEN0008	95	12611	1	4	10495	21	ETH-74402
GAEN0008	96	12610	1	4	10492	21	ETH-74403
GAEN0008	97	12609	1	4	10485	21	ETH-74404
GAEN0008	98	12608	1	4	10496	21	ETH-74405
GAEN0008	99	12607	1	4	10529	21	ETH-74406
GAEN0008	100	12606	1	4	10505	21	ETH-74407
GAEN0008	101	12605	1	4	10543	21	ETH-74408
GAEN0008	102	12604	1	4	10499	22	ETH-74409
GAEN0008	103	12603	1	4	10529	21	ETH-74410
GAEN0008	104.5	12601.5	2	4	10496	21	ETH-74411
GAEN0008	106.5	12599.5	2	4	10534	21	ETH-74412
GAEN0008	109	12597	3	4	10437	21	ETH-74413
GAEN0008	109	12597	3	4	10518	20	ETH-74413
GAEN0008	111.5	12594.5	2	4	10512	21	ETH-74414
GAEN0008	114	12592	3	4	10478	21	ETH-74415

GAEN0008	116.5	12589.5	2	4	10496	21	ETH-74416
GAEN0008	120.5	12585.5	2	4	10459	21	ETH-74418
GAEN0008	122.5	12583.5	2	4	10453	20	ETH-74419
GAEN0008	126.5	12579.5	4	4	10483	24	ETH-74420
GAEN0008	130	12576	3	4	10461	21	ETH-74421
GAEN0008	134.5	12571.5	6	4	10473	21	ETH-74422
GAEN0008	139	12567	3	4	10500	30	ETH-74424
GAEN0008	143	12563	5	4	10497	23	ETH-74425
GAEN0008	123	12583	3	4	10440	24	ETH-74762
GAEN0008	148	12558	5	4	10471	24	ETH-74763
GAEN0008	153	12553	5	4	10485	24	ETH-74764
GAEN0008	159.5	12546.5	8	4	10431	24	ETH-74765
LAND0062	33	12149	1	0	10331	23	ETH-76226
LAND0062	34	12148	1	0	10368	23	ETH-76227
LAND0062	35	12147	1	0	10409	23	ETH-76228
LAND0062	36	12146	1	0	10321	23	ETH-76229
LAND0062	37	12145	1	0	10349	23	ETH-76230
LAND0062	38	12144	1	0	10334	23	ETH-76231
LAND0062	39	12143	1	0	10355	23	ETH-76232
LAND0062	40.5	12141.5	2	0	10339	23	ETH-76233
LAND0062	42	12140	1	0	10329	23	ETH-76234
LAND0062	43	12139	1	0	10345	23	ETH-76235
LAND0062	44	12138	1	0	10349	23	ETH-76236
LAND0062	45	12137	1	0	10351	24	ETH-76237
LAND0062	46	12136	1	0	10334	23	ETH-76238
LAND0062	47	12135	1	0	10329	24	ETH-76239
LAND0062	48	12134	1	0	10352	23	ETH-76240
LAND0062	49	12133	1	0	10358	23	ETH-76241
LAND0062	50	12132	1	0	10381	23	ETH-76242
LAND0062	51.5	12130.5	2	0	10367	23	ETH-76243
LAND0062	53	12129	1	0	10366	24	ETH-76244
LAND0062	54	12128	1	0	10387	24	ETH-76245
LAND0062	55	12127	1	0	10361	24	ETH-76246
LAND0062	56	12126	1	0	10329	24	ETH-76247
LAND0062	57	12125	1	0	10338	24	ETH-76248
LAND0062	58	12124	1	0	10320	24	ETH-76249
LAND0062	59	12123	1	0	10387	24	ETH-76250
LAND0062	60	12122	1	0	10378	24	ETH-76251
LAND0062	61	12121	1	0	10348	24	ETH-76252
LAND0062	62	12120	1	0	10367	24	ETH-76253
LAND0062	63	12119	1	0	10344	24	ETH-76254
LAND0062	64	12118	1	0	10383	24	ETH-76255
LAND0062	65	12117	1	0	10363	24	ETH-76256
LAND0062	66	12116	1	0	10409	24	ETH-76257
LAND0062	67	12115	1	0	10341	23	ETH-76258
LAND0062	68	12114	1	0	10375	24	ETH-76259
LAND0062	69	12113	1	0	10360	24	ETH-76260
LAND0062	70	12112	1	0	10399	24	ETH-76261
LAND0062	71	12111	1	0	10376	23	ETH-76262
LAND0062	72	12110	1	0	10415	24	ETH-76263
LAND0062	73	12109	1	0	10397	24	ETH-76264
LAND0062	74	12108	1	0	10381	24	ETH-76265
LAND0062	75	12107	1	0	10395	24	ETH-76266
LAND0062	76	12106	1	0	10353	24	ETH-76267
LAND0062	77	12105	1	0	10404	23	ETH-76268
LAND0062	78	12104	1	0	10417	24	ETH-76269
LAND0062	79	12103	1	0	10376	24	ETH-76270
LAND0062	80	12102	1	0	10347	24	ETH-76271
LAND0062	81	12101	1	0	10311	24	ETH-76272
LAND0062	82	12100	1	0	10341	24	ETH-76273
LAND0062	83	12099	1	0	10331	23	ETH-76274
LAND0062	84	12098	1	0	10373	24	ETH-76275
LAND0062	85	12097	1	0	10303	23	ETH-76853
LAND0062	86	12096	1	0	10377	25	ETH-76854
LAND0062	87	12095	1	0	10341	24	ETH-76855
LAND0062	88	12094	1	0	10317	23	ETH-76856

LAND0062	89	12093	1	0	10352	24	ETH-76857
LAND0062	90	12092	1	0	10347	25	ETH-76858
LAND0062	92	12090	1	0	10337	24	ETH-76860
LAND0062	93	12089	1	0	10317	24	ETH-76861
LAND0062	94	12088	1	0	10305	21	ETH-76862
LAND0062	95	12087	1	0	10330	24	ETH-76863
LAND0062	96	12086	1	0	10313	24	ETH-76864
LAND0062	97	12085	1	0	10296	23	ETH-76865
LAND0062	98	12084	1	0	10357	24	ETH-76866
LAND0062	99	12083	1	0	10341	24	ETH-76867
LAND0062	100	12082	1	0	10327	20	ETH-76868
LAND0062	101	12081	1	0	10341	24	ETH-76869
LAND0062	103	12079	1	0	10353	21	ETH-76871
LAND0062	104	12078	1	0	10353	24	ETH-76872
LAND0062	105	12077	1	0	10333	24	ETH-76873
LAND0062	106	12076	1	0	10323	24	ETH-76874
LAND0062	107	12075	1	0	10345	24	ETH-76875
LAND0062	108	12074	1	0	10319	24	ETH-76876
LAND0062	109	12073	1	0	10294	23	ETH-76877
LAND0062	110	12072	1	0	10311	24	ETH-76878
LAND0062	111	12071	1	0	10351	24	ETH-76879
LAND0062	112	12070	1	0	10305	23	ETH-76880
LAND0062	113	12069	1	0	10340	24	ETH-76881
LAND0062	114	12068	1	0	10349	24	ETH-76882
LAND0062	115	12067	1	0	10350	23	ETH-76883
LAND0062	116	12066	1	0	10345	24	ETH-76884
LAND0062	117	12065	1	0	10328	24	ETH-76885
LAND0062	118	12064	1	0	10323	21	ETH-76886
LAND0062	119	12063	1	0	10361	24	ETH-76887
LAND0062	120	12062	1	0	10353	24	ETH-76888
LAND0062	121	12061	1	0	10371	21	ETH-76889
LAND0062	122	12060	1	0	10346	24	ETH-76890
LAND0062	123	12059	1	0	10341	25	ETH-76891
LAND0062	124	12058	1	0	10386	23	ETH-76892
LAND0062	125	12057	1	0	10343	25	ETH-76893
LAND0062	126	12056	1	0	10312	24	ETH-76894
LAND0062	127	12055	1	0	10276	21	ETH-76895
LAND0062	128	12054	1	0	10334	24	ETH-76896
LAND0062	129	12053	1	0	10348	24	ETH-76897
LAND0062	130	12052	1	0	10309	23	ETH-76898
LAND0062	131	12051	1	0	10348	24	ETH-76899
LAND0062	132	12050	1	0	10333	24	ETH-76900
LAND0062	134	12048	1	0	10346	24	ETH-76902
LAND0062	136	12046	1	0	10347	24	ETH-76904
LAND0062	137	12045	1	0	10373	24	ETH-76905
LAND0062	138	12044	1	0	10298	23	ETH-76906
LAND0062	139	12043	1	0	10356	24	ETH-76907
LAND0062	140	12042	1	0	10277	24	ETH-76908
LAND0062	141	12041	1	0	10298	24	ETH-76909
LAND0062	142	12040	1	0	10336	24	ETH-76910
LAND0062	143	12039	1	0	10337	24	ETH-76911
LAND0062	144	12038	1	0	10269	23	ETH-76912
LAND0062	145	12037	1	0	10328	24	ETH-76913
LAND0062	146	12036	1	0	10289	24	ETH-76914
LAND0062	147	12035	1	0	10330	24	ETH-76915
LAND0062	148	12034	1	0	10287	24	ETH-76916
LAND0062	149	12033	1	0	10298	24	ETH-76917
LAND0062	151	12031	1	0	10286	24	ETH-76919
LAND0062	152	12030	1	0	10267	24	ETH-76920
LAND0062	153	12029	1	0	10305	24	ETH-76921
LAND0062	154	12028	1	0	10341	24	ETH-76922
LAND0062	155	12027	1	0	10344	24	ETH-76923
LAND0062	156	12026	1	0	10327	25	ETH-76924
LAND0062	158	12024	3	0	10321	23	ETH-76925
LAND0062	160	12022	1	0	10339	24	ETH-76926
LAND0062	161	12021	1	0	10297	24	ETH-76927

LAND0062	163	12019	1	0	10299	20	ETH-76929
LAND0062	165.5	12016.5	2	0	10274	21	ETH-76931
LAND0062	168	12014	1	0	10304	24	ETH-76933
LAND0062	169	12013	1	0	10327	20	ETH-76934
LAND0062	171	12011	1	0	10311	23	ETH-76936
LAND0062	172	12010	1	0	10315	20	ETH-76937
LAND0062	177	12005	1	0	10322	23	ETH-76942
LAND0062	178	12004	1	0	10327	20	ETH-76943
LAND0062	180	12002	1	0	10293	21	ETH-76945
LAND0062	181	12001	1	0	10300	20	ETH-76946
LAND0062	183	11999	1	0	10262	21	ETH-76948
LAND0062	184	11998	1	0	10311	20	ETH-76949
LAND0062	186	11996	1	0	10309	21	ETH-76951
LAND0062	187	11995	1	0	10273	20	ETH-76952
LAND0062	188	11994	1	0	10283	21	ETH-76953
LAND0062	190	11992	1	0	10287	20	ETH-76955
LAND0062	191	11991	1	0	10290	21	ETH-76956
LAND0062	192	11990	1	0	10276	20	ETH-76957
LAND0062	194	11988	1	0	10281	21	ETH-76959
LAND0062	195	11987	1	0	10280	20	ETH-76960
LAND0062	197	11985	1	0	10282	20	ETH-76962
LAND0062	198	11984	1	0	10269	21	ETH-76963
LAND0062	201	11981	1	0	10292	21	ETH-76966
LAND0062	202	11980	1	0	10316	20	ETH-76967
LAND0062	204	11978	1	0	10327	21	ETH-76969
LAND0062	205	11977	1	0	10251	20	ETH-76970
LAND0062	207	11975	1	0	10268	21	ETH-76972
LAND0062	208	11974	1	0	10265	20	ETH-76973
LAND0062	210	11972	1	0	10263	21	ETH-76975
LAND0062	211	11971	1	0	10272	20	ETH-76976
LAND0062	213	11969	1	0	10259	21	ETH-76978
LAND0062	214	11968	1	0	10301	20	ETH-76979
LAND0062	215	11967	1	0	10288	20	ETH-76980
LAND0062	216	11966	1	0	10271	21	ETH-76981
LAND0062	218	11964	1	0	10228	19	ETH-76983
LAND0062	219	11963	1	0	10246	21	ETH-76984
LAND0062	222	11960	1	0	10271	21	ETH-76987
LAND0062	225	11957	1	0	10285	21	ETH-76990
LAND0062	229	11953	1	0	10299	21	ETH-76993
LAND0062	166	12016	1	0	10321	20	ETH-76998
GAEN0007	18.5	12698.5	4	4	10583	22	ETH-78846
GAEN0007	23	12694	5	4	10640	21	ETH-78847
GAEN0007	26.5	12690.5	2	4	10605	21	ETH-78848
GAEN0007	28.5	12688.5	2	4	10627	21	ETH-78849
GAEN0007	32.5	12684.5	2	4	10602	21	ETH-78851
GAEN0007	34.5	12682.5	2	4	10572	21	ETH-78852
GAEN0007	38.5	12678.5	2	4	10596	21	ETH-78854
GAEN0007	38.5	12678.5	2	4	10595	22	ETH-78854
GAEN0007	40.5	12676.5	2	4	10604	21	ETH-78855
GAEN0007	42	12675	1	4	10574	21	ETH-78856
GAEN0007	43	12674	1	4	10580	21	ETH-78857
GAEN0007	44	12673	1	4	10619	21	ETH-78858
GAEN0007	45	12672	1	4	10572	21	ETH-78859
GAEN0007	46.5	12670.5	2	4	10601	21	ETH-78860
GAEN0007	48	12669	1	4	10583	21	ETH-78861
GAEN0007	49.5	12667.5	2	4	10594	20	ETH-78862
GAEN0007	51	12666	1	4	10557	20	ETH-78863
GAEN0007	52	12665	1	4	10577	21	ETH-78864
GAEN0007	52	12665	1	4	10571	23	ETH-78864
GAEN0007	55.5	12661.5	2	4	10523	20	ETH-78867
GAEN0007	55.5	12661.5	2	4	10537	22	ETH-78867
GAEN0007	57	12660	1	4	10556	21	ETH-78868
GAEN0007	58	12659	1	4	10556	21	ETH-78869
GAEN0007	59	12658	1	4	10535	21	ETH-78870
GAEN0007	60	12657	1	4	10574	21	ETH-78871
GAEN0007	61	12656	1	4	10568	21	ETH-78872

GAEN0007	62	12655	1	4	10594	21	ETH-78873
GAEN0007	63	12654	1	4	10568	21	ETH-78874
LAND0004	19	12296	1	0	10415	21	ETH-79039
LAND0004	20	12295	1	0	10388	21	ETH-79040
LAND0004	21	12294	1	0	10375	21	ETH-79041
LAND0004	22	12293	1	0	10393	19	ETH-79042
LAND0004	23	12292	1	0	10434	21	ETH-79043
LAND0004	24	12291	1	0	10408	21	ETH-79044
LAND0004	25	12290	1	0	10420	21	ETH-79045
LAND0004	26	12289	1	0	10453	21	ETH-79046
LAND0004	27	12288	1	0	10414	21	ETH-79047
LAND0004	28	12287	1	0	10411	21	ETH-79048
LAND0004	29	12286	1	0	10430	21	ETH-79049
LAND0004	30	12285	1	0	10410	21	ETH-79050
LAND0004	31	12284	1	0	10430	21	ETH-79051
LAND0004	32	12283	1	0	10420	21	ETH-79052
LAND0004	33	12282	1	0	10443	21	ETH-79053
LAND0004	34	12281	1	0	10393	19	ETH-79054
LAND0004	35	12280	1	0	10432	21	ETH-79055
LAND0004	36	12279	1	0	10445	21	ETH-79056
LAND0004	37	12278	1	0	10401	21	ETH-79057
LAND0004	38	12277	1	0	10395	20	ETH-79058
LAND0004	39	12276	1	0	10437	21	ETH-79059
LAND0004	40	12275	1	0	10439	21	ETH-79060
LAND0004	41	12274	1	0	10382	21	ETH-79061
LAND0004	42	12273	1	0	10409	21	ETH-79062
LAND0004	43	12272	1	0	10393	21	ETH-79063
LAND0004	44	12271	1	0	10407	21	ETH-79064
LAND0004	45	12270	1	0	10383	19	ETH-79065
LAND0004	46	12269	1	0	10386	21	ETH-79066
LAND0004	47	12268	1	0	10388	21	ETH-79067
LAND0004	48	12267	1	0	10379	19	ETH-79068
LAND0004	49	12266	1	0	10380	19	ETH-79069
LAND0004	50	12265	1	0	10334	19	ETH-79070
LAND0004	51	12264	1	0	10389	19	ETH-79071
LAND0004	52	12263	1	0	10371	19	ETH-79072
LAND0004	53	12262	1	0	10382	19	ETH-79073
LAND0004	54	12261	1	0	10398	19	ETH-79074
LAND0004	55	12260	1	0	10381	19	ETH-79075
LAND0004	56	12259	1	0	10384	20	ETH-79076
LAND0004	57	12258	1	0	10388	19	ETH-79077
LAND0004	58	12257	1	0	10401	19	ETH-79078
LAND0004	59	12256	1	0	10384	19	ETH-79079
LAND0004	60	12255	1	0	10384	18	ETH-79080
LAND0004	61	12254	1	0	10369	19	ETH-79081
LAND0004	62	12253	1	0	10369	20	ETH-79082
LAND0004	63	12252	1	0	10365	20	ETH-79083
LAND0004	64	12251	1	0	10370	20	ETH-79084
LAND0004	65	12250	1	0	10351	20	ETH-79085
LAND0004	66	12249	1	0	10369	20	ETH-79086
LAND0004	67	12248	1	0	10350	20	ETH-79087
LAND0004	68	12247	1	0	10379	20	ETH-79088
LAND0004	69	12246	1	0	10361	21	ETH-79280
LAND0004	70	12245	1	0	10324	21	ETH-79281
LAND0004	71	12244	1	0	10309	21	ETH-79282
LAND0004	72	12243	1	0	10368	21	ETH-79283
LAND0004	73	12242	1	0	10345	21	ETH-79284
LAND0004	74	12241	1	0	10374	21	ETH-79285
LAND0004	75	12240	1	0	10377	21	ETH-79286
LAND0004	76	12239	1	0	10383	21	ETH-79287
LAND0004	77	12238	1	0	10396	21	ETH-79288
LAND0004	78	12237	1	0	10339	21	ETH-79289
LAND0004	79	12236	1	0	10387	21	ETH-79290
LAND0004	80	12235	1	0	10379	21	ETH-79291
LAND0004	81	12234	1	0	10359	21	ETH-79292
LAND0004	82	12233	1	0	10362	21	ETH-79293

LAND0004	83	12232	1	0	10381	21	ETH-79294
LAND0004	84	12231	1	0	10394	21	ETH-79295
LAND0004	85	12230	1	0	10388	21	ETH-79296
LAND0004	86	12229	1	0	10393	21	ETH-79297
LAND0004	87	12228	1	0	10371	21	ETH-79298
LAND0004	88	12227	1	0	10392	21	ETH-79299
LAND0004	89	12226	1	0	10401	21	ETH-79300
LAND0004	90	12225	1	0	10374	21	ETH-79301
LAND0004	91	12224	1	0	10402	21	ETH-79302
LAND0004	92	12223	1	0	10395	21	ETH-79303
LAND0004	93	12222	1	0	10460	21	ETH-79304
LAND0004	94	12221	1	0	10422	21	ETH-79305
LAND0004	95	12220	1	0	10399	21	ETH-79306
LAND0004	96	12219	1	0	10373	22	ETH-79307
LAND0004	97	12218	1	0	10394	21	ETH-79308
LAND0004	98	12217	1	0	10411	21	ETH-79309
LAND0004	99	12216	1	0	10427	21	ETH-79310
LAND0004	100	12215	1	0	10420	21	ETH-79311
LAND0004	101	12214	1	0	10469	21	ETH-79312
LAND0004	102	12213	1	0	10451	21	ETH-79313
LAND0004	103	12212	1	0	10470	22	ETH-79314
LAND0004	104	12211	1	0	10445	22	ETH-79315
LAND0004	105	12210	1	0	10426	22	ETH-79316
LAND0004	106	12209	1	0	10434	22	ETH-79317
LAND0004	107	12208	1	0	10397	21	ETH-79318
LAND0004	108	12207	1	0	10435	22	ETH-79319
LAND0004	109	12206	1	0	10382	21	ETH-79320
LAND0004	110	12205	1	0	10409	21	ETH-79321
LAND0004	111	12204	1	0	10386	22	ETH-79322
LAND0004	112	12203	1	0	10387	22	ETH-79323
LAND0004	113	12202	1	0	10404	22	ETH-79324
LAND0004	114	12201	1	0	10413	22	ETH-79325
LAND0004	115	12200	1	0	10409	21	ETH-79326
LAND0004	116	12199	1	0	10400	22	ETH-79327
LAND0004	117	12198	1	0	10446	22	ETH-79328
LAND0004	118	12197	1	0	10420	22	ETH-79329
LAND0004	119	12196	1	0	10389	19	ETH-79843
LAND0004	119	12196	1	0	10390	22	ETH-79843
LAND0004	120	12195	1	0	10435	19	ETH-79844
LAND0004	120	12195	1	0	10354	22	ETH-79844
LAND0004	121	12194	1	0	10386	19	ETH-79845
LAND0004	121	12194	1	0	10373	22	ETH-79845
LAND0004	122	12193	1	0	10355	22	ETH-79846
LAND0004	123	12192	1	0	10379	22	ETH-79847
LAND0004	124	12191	1	0	10357	22	ETH-79848
LAND0004	125	12190	1	0	10302	23	ETH-79849
LAND0004	125	12190	1	0	10343	22	ETH-79849
LAND0004	126	12189	1	0	10346	22	ETH-79850
LAND0004	127	12188	1	0	10354	22	ETH-79851
LAND0004	128	12187	1	0	10380	22	ETH-79852
LAND0004	129	12186	1	0	10321	24	ETH-79853
LAND0004	129	12186	1	0	10377	22	ETH-79853
LAND0004	130	12185	1	0	10330	24	ETH-79854
LAND0004	130	12185	1	0	10339	22	ETH-79854
LAND0004	131	12184	1	0	10343	24	ETH-79855
LAND0004	131	12184	1	0	10383	22	ETH-79855
LAND0004	132	12183	1	0	10357	24	ETH-79856
LAND0004	132	12183	1	0	10406	22	ETH-79856
LAND0004	133	12182	1	0	10391	24	ETH-79857
LAND0004	133	12182	1	0	10397	22	ETH-79857
LAND0004	134	12181	1	0	10350	24	ETH-79858
LAND0004	134	12181	1	0	10390	22	ETH-79858
LAND0004	135	12180	1	0	10343	24	ETH-79859
LAND0004	135	12180	1	0	10380	22	ETH-79859
LAND0004	136	12179	1	0	10391	24	ETH-79860
LAND0004	136	12179	1	0	10370	22	ETH-79860

LAND0004	137	12178	1	0	10357	24	ETH-79861
LAND0004	137	12178	1	0	10381	22	ETH-79861
LAND0004	138	12177	1	0	10364	24	ETH-79862
LAND0004	138	12177	1	0	10379	22	ETH-79862
LAND0004	139	12176	1	0	10327	24	ETH-79863
LAND0004	139	12176	1	0	10366	22	ETH-79863
LAND0004	140	12175	1	0	10316	23	ETH-79864
LAND0004	140	12175	1	0	10356	22	ETH-79864
LAND0004	141	12174	1	0	10344	23	ETH-79865
LAND0004	141	12174	1	0	10388	22	ETH-79865
LAND0004	142	12173	1	0	10369	24	ETH-79866
LAND0004	142	12173	1	0	10364	22	ETH-79866
LAND0004	143	12172	1	0	10378	24	ETH-79867
LAND0004	143	12172	1	0	10360	22	ETH-79867
LAND0004	144	12171	1	0	10359	24	ETH-79868
LAND0004	144	12171	1	0	10385	22	ETH-79868
LAND0004	145	12170	1	0	10367	24	ETH-79869
LAND0004	145	12170	1	0	10372	22	ETH-79869
LAND0004	146	12169	1	0	10352	24	ETH-79870
LAND0004	146	12169	1	0	10361	22	ETH-79870
GAEN0008	32	12674	1	4	10600	20	ETH-79226
GAEN0008	33	12673	1	4	10581	20	ETH-79227
GAEN0008	34	12672	1	4	10552	20	ETH-79228
GAEN0008	35	12671	1	4	10609	20	ETH-79229
GAEN0008	36	12670	1	4	10618	23	ETH-79230
GAEN0008	37.5	12668.5	2	4	10619	20	ETH-79231
GAEN0008	39.5	12666.5	2	4	10588	21	ETH-79232
GAEN0008	41	12665	1	4	10575	21	ETH-79233
GAEN0008	42	12664	1	4	10573	20	ETH-79234
GAEN0008	43	12663	1	4	10595	21	ETH-79235
GAEN0008	44	12662	1	4	10587	21	ETH-79236
GAEN0008	45	12661	1	4	10578	21	ETH-79237
GAEN0008	45	12661	1	4	10575	24	ETH-79237
GAEN0008	46	12660	1	4	10609	24	ETH-79238
GAEN0008	47	12659	1	4	10562	20	ETH-79239
GAEN0008	48	12658	1	4	10596	20	ETH-79240
GAEN0008	49	12657	1	4	10593	20	ETH-79241
GAEN0008	50	12656	1	4	10628	20	ETH-79242
GAEN0008	50	12656	1	4	10605	22	ETH-79242
GAEN0008	50	12656	1	4	10563	24	ETH-79242
GAEN0008	51	12655	1	4	10585	20	ETH-79243
GAEN0008	52	12654	1	4	10600	20	ETH-79244
GAEN0008	53	12653	1	4	10548	21	ETH-79245
GAEN0008	53	12653	1	4	10623	23	ETH-79245
GAEN0008	54	12652	1	4	10590	23	ETH-79246
GAEN0008	55	12651	1	4	10589	21	ETH-79247
GAEN0008	56	12650	1	4	10532	20	ETH-79248
GAEN0008	57	12649	1	4	10593	23	ETH-79249
GAEN0008	58	12648	1	4	10568	24	ETH-79250
GAEN0008	59	12647	1	4	10531	25	ETH-79251
GAEN0008	60	12646	1	4	10583	23	ETH-79252
GAEN0008	61	12645	1	4	10524	23	ETH-79253
GAEN0008	62	12644	1	4	10584	23	ETH-79254
GAEN0008	63	12643	1	4	10639	24	ETH-79255
GAEN0008	64	12642	1	4	10610	23	ETH-79256
GAEN0008	65	12641	1	4	10645	23	ETH-79257
GAEN0008	66	12640	1	4	10575	23	ETH-79258
GAEN0008	67	12639	1	4	10614	25	ETH-79259
GAEN0008	76	12630	1	4	10634	24	ETH-79260
GAEN0008	79	12627	1	4	10588	23	ETH-79263
GAEN0008	96	12610	1	4	10554	23	ETH-79264
GAEN0008	97	12609	1	4	10556	23	ETH-79265
GAEN0008	98	12608	1	4	10491	23	ETH-79266
GAEN0008	107	12599	1	4	10496	23	ETH-79267
GAEN0008	108	12598	1	4	10518	23	ETH-79268
GAEN0008	109	12597	1	4	10503	20	ETH-79269

KHWI0030	24.5	12473.5	2	4	10430	20	ETH-75666
KHWI0030	32	12466	3	4	10420	21	ETH-75667
KHWI0030	45.5	12452.5	2	4	10390	21	ETH-75668
KHWI0030	76	12422	3	4	10311	20	ETH-75669
KHWI0030	171	12327	3	4	10418	20	ETH-75670
KHWI0030	78	12420	1	4	10301	19	ETH-79886
KHWI0030	88	12410	1	4	10337	19	ETH-79887
KHWI0030	98	12400	1	4	10359	19	ETH-79888
KHWI0030	118	12380	1	4	10371	19	ETH-79889
KHWI0030	128	12370	1	4	10361	19	ETH-79890
KHWI0030	138	12360	1	4	10372	19	ETH-79891
KHWI0030	152	12346	1	4	10410	19	ETH-79892
KHWI0030	158	12340	1	4	10446	19	ETH-79893
KHWI0030	79	12419	1	4	10330	19	ETH-80061
KHWI0030	81	12417	1	4	10292	20	ETH-80062
KHWI0030	83	12415	1	4	10310	20	ETH-80063
KHWI0030	85	12413	1	4	10348	20	ETH-80064
KHWI0030	87	12411	1	4	10312	22	ETH-80065
KHWI0030	89	12409	1	4	10307	20	ETH-80066
KHWI0030	89	12409	1	4	10324	22	ETH-80066
KHWI0030	91	12407	1	4	10341	20	ETH-80067
KHWI0030	93	12405	1	4	10330	20	ETH-80068
KHWI0030	95	12403	1	4	10351	20	ETH-80069
KHWI0030	97	12401	1	4	10338	20	ETH-80070
KHWI0030	99	12399	1	4	10368	20	ETH-80071
KHWI0030	103	12395	1	4	10342	20	ETH-80073
KHWI0030	105	12393	1	4	10370	20	ETH-80074
KHWI0030	107	12391	1	4	10384	20	ETH-80075
KHWI0030	109	12389	1	4	10396	22	ETH-80076
KHWI0030	109	12389	1	4	10376	23	ETH-80076
KHWI0030	109	12389	1	4	10408	23	ETH-80076
KHWI0030	111	12387	1	4	10359	20	ETH-80077
KHWI0030	111	12387	1	4	10371	23	ETH-80077
KHWI0030	111	12387	1	4	10393	23	ETH-80077
KHWI0030	113	12385	1	4	10348	20	ETH-80078
KHWI0030	113	12385	1	4	10391	23	ETH-80078
KHWI0030	113	12385	1	4	10397	23	ETH-80078
KHWI0030	115	12383	1	4	10326	20	ETH-80079
KHWI0030	115	12383	1	4	10400	23	ETH-80079
KHWI0030	115	12383	1	4	10386	23	ETH-80079
KHWI0030	117	12381	1	4	10346	20	ETH-80080
KHWI0030	117	12381	1	4	10403	20	ETH-80080
KHWI0030	117	12381	1	4	10389	20	ETH-80080
KHWI0030	119	12379	1	4	10372	20	ETH-80081
KHWI0030	119	12379	1	4	10398	20	ETH-80081
KHWI0030	119	12379	1	4	10412	20	ETH-80081
KHWI0030	121	12377	1	4	10374	20	ETH-80082
KHWI0030	123	12375	1	4	10367	20	ETH-80083
KHWI0030	125	12373	1	4	10344	20	ETH-80084
KHWI0030	127	12371	1	4	10360	22	ETH-80085
KHWI0030	129	12369	1	4	10342	20	ETH-80086
KHWI0030	131	12367	1	4	10385	19	ETH-80087
KHWI0030	133	12365	1	4	10325	22	ETH-80088
KHWI0030	135	12363	1	4	10322	20	ETH-80089
KHWI0030	137	12361	1	4	10401	22	ETH-80090
KHWI0030	139	12359	1	4	10363	22	ETH-80091
KHWI0030	141	12357	1	4	10376	22	ETH-80092
KHWI0030	143	12355	1	4	10370	22	ETH-80093
KHWI0030	145	12353	1	4	10406	22	ETH-80094
KHWI0030	147	12351	1	4	10406	22	ETH-80095
KHWI0030	149	12349	1	4	10433	22	ETH-80096
KHWI0030	151	12347	1	4	10428	22	ETH-80097
KHWI0030	153	12345	1	4	10421	22	ETH-80098
KHWI0030	155	12343	1	4	10447	22	ETH-80099
KHWI0030	157	12341	1	4	10445	22	ETH-80100
KHWI0030	159	12339	1	4	10446	22	ETH-80101

KHWI0030	160.5	12337.5	2	4	10453	22	ETH-80102
KHWI0030	163	12335	1	4	10457	22	ETH-80103
KHWI0030	165	12333	1	4	10413	22	ETH-80104
KHWI0030	167	12331	1	4	10391	21	ETH-80105
KHWI0030	169	12329	1	4	10361	21	ETH-80106
KHWI0030	171	12327	1	4	10378	21	ETH-80107
KHWI0030	173	12325	1	4	10353	21	ETH-80108
KHWI0030	175	12323	1	4	10390	21	ETH-80109
KHWI0030	178.5	12319.5	2	4	10362	21	ETH-80110
KHWI0030	80	12418	1	4	10366	20	ETH-80195
KHWI0030	82	12416	1	4	10370	20	ETH-80196
KHWI0030	84	12414	1	4	10339	20	ETH-80197
KHWI0030	86	12412	1	4	10360	20	ETH-80198
KHWI0030	90	12408	1	4	10357	21	ETH-80199
KHWI0030	92	12406	1	4	10356	20	ETH-80200
KHWI0030	94	12404	1	4	10377	21	ETH-80201
KHWI0030	96	12402	1	4	10369	20	ETH-80202
KHWI0030	100	12398	1	4	10375	20	ETH-80203
KHWI0030	102	12396	1	4	10359	22	ETH-80204
KHWI0030	104	12394	1	4	10394	21	ETH-80205
KHWI0030	106	12392	1	4	10379	20	ETH-80206
KHWI0030	108	12390	1	4	10386	21	ETH-80207
KHWI0030	110	12389	1	4	10373	21	ETH-80208
KHWI0030	110	12389	1	4	10371	23	ETH-80208
KHWI0030	110	12389	1	4	10393	23	ETH-80208
KHWI0030	112	12386	1	4	10349	23	ETH-80209
KHWI0030	114	12384	1	4	10364	20	ETH-80210
KHWI0030	114	12384	1	4	10433	23	ETH-80210
KHWI0030	114	12384	1	4	10420	27	ETH-80210
KHWI0030	116	12382	1	4	10361	21	ETH-80211
KHWI0030	116	12382	1	4	10406	23	ETH-80211
KHWI0030	116	12382	1	4	10400	20	ETH-80211
KHWI0030	120	12378	1	4	10348	21	ETH-80212
KHWI0030	122	12376	1	4	10378	21	ETH-80213
KHWI0030	124	12374	1	4	10389	19	ETH-80214
KHWI0030	126	12372	1	4	10375	21	ETH-80215
KHWI0030	130	12368	1	4	10392	21	ETH-80216
KHWI0030	132	12366	1	4	10334	21	ETH-80217
KHWI0030	134	12364	1	4	10366	21	ETH-80218
KHWI0030	136	12362	1	4	10390	19	ETH-80219
KHWI0030	140	12358	1	4	10344	22	ETH-80220
KHWI0030	142	12356	1	4	10401	21	ETH-80221
KHWI0030	144	12354	1	4	10401	21	ETH-80222
KHWI0030	146	12352	1	4	10403	22	ETH-80223
KHWI0030	148	12350	1	4	10408	22	ETH-80224
KHWI0030	150	12348	1	4	10415	22	ETH-80225
KHWI0030	154	12344	1	4	10440	21	ETH-80226
KHWI0030	156	12342	1	4	10444	22	ETH-80227
KHWI0030	162	12336	1	4	10444	22	ETH-80228
KHWI0030	164	12334	1	4	10408	22	ETH-80229
KHWI0030	166	12332	1	4	10393	21	ETH-80230
KHWI0030	168	12330	1	4	10385	22	ETH-80231
KHWI0030	170	12328	1	4	10386	22	ETH-80232
KHWI0030	172	12326	1	4	10392	22	ETH-80233
KHWI0030	176.5	12321.5	2	4	10332	22	ETH-80235
KHWI0030	182	12316	1	4	10361	22	ETH-80238
KHWI0030	183	12315	1	4	10374	23	ETH-80239
KHWI0030	184	12314	1	4	10344	22	ETH-80240
KHWI0030	185	12313	1	4	10368	22	ETH-80241
KHWI0030	186	12312	1	4	10372	22	ETH-80242
KHWI0028	27	12219	1	0	10343	23	ETH-81017
KHWI0028	27	12219	1	0	10385	23	ETH-81017
KHWI0028	29	12217	1	0	10442	22	ETH-81018
KHWI0028	29	12217	1	0	10377	23	ETH-81018
KHWI0028	31	12215	1	0	10394	23	ETH-81019
KHWI0028	31	12215	1	0	10445	23	ETH-81019

KHWI0028	33	12213	1	0	10445	22	ETH-81020
KHWI0028	37	12209	1	0	10383	23	ETH-81021
KHWI0028	37	12209	1	0	10381	23	ETH-81021
KHWI0028	39	12207	1	0	10400	23	ETH-81022
KHWI0028	41	12205	1	0	10406	23	ETH-81023
KHWI0028	43	12203	1	0	10426	23	ETH-81024
KHWI0028	45	12201	1	0	10403	23	ETH-81025
KHWI0028	47	12199	1	0	10454	22	ETH-81026
KHWI0028	47	12199	1	0	10403	23	ETH-81026
KHWI0028	49	12197	1	0	10396	23	ETH-81027
KHWI0028	51	12195	1	0	10395	22	ETH-81028
KHWI0028	51	12195	1	0	10382	23	ETH-81028
KHWI0028	53	12193	1	0	10370	23	ETH-81029
KHWI0028	55	12191	1	0	10392	22	ETH-81030
KHWI0028	57	12189	1	0	10405	23	ETH-81031
KHWI0028	59	12187	1	0	10427	22	ETH-81032
KHWI0028	59	12187	1	0	10390	23	ETH-81032
KHWI0028	61	12185	1	0	10399	23	ETH-81033
KHWI0028	61	12185	1	0	10384	23	ETH-81033
KHWI0028	63	12183	1	0	10394	22	ETH-81034
KHWI0028	65	12181	1	0	10407	23	ETH-81035
KHWI0028	65	12181	1	0	10409	23	ETH-81035
KHWI0028	67	12179	1	0	10419	22	ETH-81036
KHWI0028	67	12179	1	0	10376	23	ETH-81036
KHWI0028	69	12177	1	0	10409	23	ETH-81037
KHWI0028	71	12175	1	0	10389	22	ETH-81038
KHWI0028	73	12173	1	0	10371	23	ETH-81039
KHWI0028	75	12171	1	0	10367	22	ETH-81040
KHWI0028	75	12171	1	0	10367	23	ETH-81040
KHWI0028	77	12169	1	0	10375	23	ETH-81041
KHWI0028	77	12169	1	0	10384	23	ETH-81041
KHWI0028	79	12167	1	0	10323	22	ETH-81042
KHWI0028	81	12165	1	0	10364	23	ETH-81043
KHWI0028	83	12163	1	0	10310	22	ETH-81044
KHWI0028	86	12160	1	0	10363	23	ETH-81045
KHWI0028	88	12158	1	0	10348	22	ETH-81046
KHWI0028	90	12156	1	0	10363	23	ETH-81047
KHWI0028	90	12156	1	0	10347	23	ETH-81047
KHWI0028	92	12154	1	0	10405	22	ETH-81048
KHWI0028	92	12154	1	0	10349	23	ETH-81048
KHWI0028	95	12151	1	0	10376	22	ETH-81049
KHWI0028	97	12149	1	0	10405	22	ETH-81050
KHWI0028	97	12149	1	0	10360	23	ETH-81050
KHWI0028	99	12147	1	0	10364	24	ETH-81051
KHWI0028	101	12145	1	0	10353	23	ETH-81052
KHWI0028	103	12143	1	0	10380	24	ETH-81053
KHWI0028	105	12141	1	0	10401	22	ETH-81054
KHWI0028	105	12141	1	0	10398	24	ETH-81054
KHWI0028	107	12139	1	0	10358	24	ETH-81055
KHWI0028	107	12139	1	0	10367	23	ETH-81055
KHWI0028	111	12135	1	0	10338	23	ETH-81056
KHWI0028	121	12125	1	0	10329	24	ETH-81057
KHWI0028	121	12125	1	0	10368	23	ETH-81057
KHWI0028	129.5	12116.5	2	0	10376	24	ETH-81058
KHWI0028	129.5	12116.5	2	0	10368	23	ETH-81058
KHWI0028	131.5	12114.5	2	0	10357	24	ETH-81059
KHWI0028	131.5	12114.5	2	0	10368	23	ETH-81059
KHWI0028	136	12110	1	0	10382	24	ETH-81060
KHWI0028	136	12110	1	0	10371	23	ETH-81060
KHWI0028	137	12109	1	0	10352	24	ETH-81061
KHWI0031	121	12386	1	4	10412	22	ETH-81957
KHWI0031	121	12386	1	4	10398	22	ETH-81957
KHWI0031	121	12386	1	4	10370	23	ETH-81957
KHWI0031	123	12384	1	4	10355	23	ETH-81958
KHWI0031	123	12384	1	4	10379	23	ETH-81958
KHWI0031	123	12384	1	4	10385	23	ETH-81958

KHWI0031	125	12382	1	4	10376	21	ETH-81959
KHWI0031	125	12382	1	4	10369	23	ETH-81959
KHWI0031	125	12382	1	4	10387	23	ETH-81959
KHWI0031	127	12380	1	4	10411	23	ETH-81960
KHWI0031	127	12380	1	4	10387	20	ETH-81960
KHWI0031	129	12378	1	4	10396	23	ETH-81961
KHWI0031	129	12378	1	4	10376	20	ETH-81961
KHWI0031	131	12376	1	4	10330	23	ETH-81962
KHWI0031	133	12374	1	4	10377	22	ETH-81963
KHWI0031	135	12372	1	4	10323	23	ETH-81964
KHWI0031	137	12370	1	4	10423	22	ETH-81965
KHWI0031	139	12368	1	4	10358	23	ETH-81966
KHWI0031	141	12366	1	4	10357	23	ETH-81967
KHWI0031	143	12364	1	4	10359	23	ETH-81968
KHWI0031	145	12362	1	4	10382	23	ETH-81969
KHWI0031	147	12360	1	4	10361	23	ETH-81970
KHWI0031	149	12358	1	4	10385	22	ETH-81971
KHWI0031	151	12356	1	4	10390	23	ETH-81972
KHWI0031	153	12354	1	4	10367	23	ETH-81973
KHWI0031	155	12352	1	4	10388	23	ETH-81974
KHWI0031	157	12350	1	4	10408	22	ETH-81975
KHWI0031	159	12348	1	4	10365	23	ETH-81976
KHWI0031	161	12346	1	4	10413	22	ETH-81977
KHWI0031	179	12328	1	4	10391	24	ETH-81985
KHWI0031	182	12325	1	4	10353	23	ETH-81986
KHWI0031	184	12323	1	4	10360	23	ETH-81987
KHWI0031	186	12321	1	4	10340	23	ETH-81988
KHWI0031	189	12318	1	4	10352	23	ETH-81989
KHWI0031	193	12314	1	4	10369	23	ETH-81991
KHWI0031	195	12312	1	4	10372	23	ETH-81992
KHWI0031	197.5	12309.5	2	4	10384	23	ETH-81993
KHWI0031	199	12308	1	4	10348	23	ETH-81994
KHWI0031	200	12307	1	4	10382	23	ETH-81995
KHWI0031	201.5	12305.5	2	4	10421	23	ETH-81996
KHWI0031	203.5	12303.5	2	4	10402	23	ETH-81997
KHWI0031	205.5	12301.5	2	4	10418	23	ETH-81998
KHWI0031	207.5	12299.5	2	4	10400	23	ETH-81999
KHWI0031	209.5	12297.5	2	4	10374	23	ETH-82000
KHWI0031	212	12295	1	4	10411	24	ETH-82002
KHWI0031	213.5	12293.5	2	4	10439	24	ETH-82003
KHWI0031	120	12386	1	4	10316	22	ETH-82213
KHWI0031	120	12386	1	4	10393	23	ETH-82213
KHWI0031	120	12386	1	4	10341	23	ETH-82213
KHWI0031	122	12384	1	4	10329	22	ETH-82214
KHWI0031	122	12384	1	4	10337	22	ETH-82214
KHWI0031	122	12384	1	4	10366	23	ETH-82214
KHWI0031	124	12382	1	4	10348	22	ETH-82215
KHWI0031	124	12382	1	4	10360	23	ETH-82215
KHWI0031	124	12382	1	4	10382	23	ETH-82215
KHWI0031	126	12380	1	4	10375	22	ETH-82216
KHWI0031	126	12380	1	4	10410	23	ETH-82216
KHWI0031	126	12380	1	4	10372	23	ETH-82216
KHWI0031	128	12378	1	4	10386	22	ETH-82217
KHWI0031	128	12378	1	4	10321	21	ETH-82217
KHWI0031	128	12378	1	4	10386	20	ETH-82217
KHWI0031	130	12376	1	4	10380	22	ETH-82218
KHWI0031	132	12374	1	4	10361	22	ETH-82219
KHWI0031	134	12372	1	4	10351	22	ETH-82220
KHWI0031	136	12370	1	4	10363	22	ETH-82221
KHWI0031	138	12368	1	4	10372	22	ETH-82222
KHWI0031	140	12366	1	4	10346	21	ETH-82223
KHWI0031	142	12364	1	4	10362	22	ETH-82224
KHWI0031	144	12362	1	4	10346	21	ETH-82225
KHWI0031	146	12360	1	4	10389	22	ETH-82226
KHWI0031	148	12358	1	4	10356	22	ETH-82227
KHWI0031	150	12356	1	4	10372	22	ETH-82228

KHWI0031	152	12354	1	4	10376	22	ETH-82229
KHWI0031	154	12352	1	4	10384	22	ETH-82230
KHWI0031	156	12350	1	4	10400	22	ETH-82231
KHWI0031	158	12348	1	4	10406	22	ETH-82232
KHWI0031	160	12346	1	4	10388	22	ETH-82233
KHWI0031	180.5	12325.5	2	4	10340	22	ETH-82241
KHWI0031	183	12323	1	4	10328	22	ETH-82242
KHWI0031	185	12321	1	4	10347	22	ETH-82243
KHWI0031	187.5	12318.5	2	4	10336	22	ETH-82244
KHWI0031	190	12316	1	4	10362	22	ETH-82245
KHWI0031	196	12310	1	4	10320	22	ETH-82248
KHWI0031	163	12343	1	4	10439	22	ETH-83841
KHWI0031	164	12342	1	4	10400	24	ETH-83842
KHWI0031	165	12341	1	4	10433	22	ETH-83843
KHWI0031	166	12340	1	4	10435	22	ETH-83844
KHWI0031	167	12339	1	4	10405	23	ETH-83845
KHWI0031	168	12338	1	4	10447	22	ETH-83846
KHWI0031	169	12337	1	4	10405	24	ETH-83847
KHWI0031	170	12336	1	4	10439	23	ETH-83848
KHWI0031	171	12335	1	4	10394	22	ETH-83849
KHWI0031	172	12334	1	4	10390	22	ETH-83850
KHWI0031	173	12333	1	4	10404	22	ETH-83851
KHWI0031	174	12332	1	4	10377	22	ETH-83852
KHWI0031	175	12331	1	4	10352	24	ETH-83853
KHWI0031	176	12330	1	4	10405	22	ETH-83854
KHWI0031	177	12329	1	4	10384	22	ETH-83855
KHWI0031	178.5	12327.5	2	4	10319	23	ETH-83856
KHWI0031	180	12326	1	4	10383	22	ETH-83858
GAEN0071	43.5	13161.5	2	4	11212	24	ETH-85697
GAEN0071	47	13158	1	4	11190	24	ETH-85699
GAEN0071	49	13156	1	4	11244	22	ETH-85701
GAEN0071	51	13154	1	4	11227	24	ETH-85703
GAEN0071	53	13152	1	4	11182	24	ETH-85705
GAEN0071	55	13150	1	4	11212	24	ETH-85707
GAEN0071	57	13148	1	4	11193	24	ETH-85709
GAEN0071	59	13146	1	4	11213	24	ETH-85711
GAEN0071	61	13144	1	4	11248	23	ETH-85713
GAEN0071	64	13141	3	4	11209	23	ETH-85715
GAEN0071	67	13138	1	4	11229	23	ETH-85717
GAEN0071	69	13136	1	4	11249	24	ETH-85719
GAEN0071	72.5	13132.5	2	4	11275	24	ETH-85721
GAEN0071	75	13130	1	4	11256	24	ETH-85723
GAEN0071	77	13128	1	4	11263	24	ETH-85725
GAEN0071	79	13126	1	4	11300	24	ETH-85727
GAEN0071	81	13124	1	4	11219	22	ETH-85729
GAEN0071	83	13122	1	4	11218	24	ETH-85731
GAEN0071	85	13120	1	4	11206	24	ETH-85733
GAEN0071	87	13118	1	4	11221	23	ETH-85735
GAEN0071	89	13116	1	4	11214	23	ETH-85737
GAEN0071	91	13114	1	4	11198	24	ETH-85739
GAEN0071	93	13112	1	4	11137	23	ETH-85741
GAEN0071	95	13110	1	4	11192	24	ETH-85743
GAEN0071	97	13108	1	4	11232	22	ETH-85745
GAEN0071	99	13106	1	4	11233	24	ETH-85747
GAEN0071	101	13104	1	4	11240	24	ETH-85749
GAEN0071	103	13102	1	4	11219	23	ETH-85751
GAEN0071	105.5	13099.5	2	4	11186	24	ETH-85753
GAEN0071	109.5	13095.5	2	4	11100	22	ETH-85755
GAEN0071	112	13093	1	4	11092	22	ETH-85757
GAEN0071	114	13091	1	4	11113	22	ETH-85759
GAEN0071	116	13089	1	4	11051	22	ETH-85761
GAEN0071	118	13087	1	4	11107	22	ETH-85763
GAEN0071	120	13085	1	4	11117	22	ETH-85765
GAEN0071	123.5	13081.5	2	4	11129	22	ETH-85767
GAEN0071	127	13078	1	4	11100	22	ETH-85769
GAEN0071	129.5	13075.5	2	4	11037	22	ETH-85771

GAEN0071	132	13073	1	4	11049	22	ETH-85773
GAEN0071	135.5	13069.5	2	4	11063	22	ETH-85775
GAEN0071	139.5	13065.5	2	4	11055	23	ETH-85777
GAEN0071	142	13063	1	4	11064	22	ETH-85779
GAEN0071	144	13061	1	4	11066	22	ETH-85781
GAEN0071	147.5	13057.5	2	4	11073	22	ETH-85783
GAEN0071	151	13054	1	4	11010	22	ETH-85785
GAEN0071	153	13052	1	4	11007	22	ETH-85787
GAEN0071	156.5	13048.5	2	4	11032	22	ETH-85789
GAEN0071	160.5	13044.5	2	4	11043	22	ETH-85791
GAEN0071	163	13042	1	4	11048	22	ETH-85793
GAEN0071	165	13040	1	4	11066	22	ETH-85795
GAEN0071	166	13039	1	4	11038	22	ETH-86134
GAEN0071	168	13037	1	4	11012	22	ETH-86136
GAEN0071	169	13036	1	4	11007	22	ETH-86137
GAEN0071	170	13035	1	4	11025	22	ETH-86138
GAEN0071	172	13033	1	4	11045	23	ETH-86140
GAEN0071	174	13031	1	4	11060	22	ETH-86142
GAEN0071	176.5	13028.5	2	4	11062	22	ETH-86144
GAEN0071	179	13026	1	4	11041	22	ETH-86146
GAEN0071	180.5	13024.5	2	4	11081	22	ETH-86147
GAEN0071	182	13023	1	4	11061	22	ETH-86148
GAEN0071	185.5	13019.5	2	4	11073	23	ETH-86150
GAEN0071	189.5	13015.5	2	4	11068	22	ETH-86152
GAEN0071	193.5	13011.5	2	4	11077	22	ETH-86154
GAEN0071	197.5	13007.5	2	4	11029	21	ETH-86156
GAEN0071	199.5	13005.5	2	4	11052	22	ETH-86157
GAEN0071	201.5	13003.5	2	4	11076	22	ETH-86158
GAEN0071	206.5	12998.5	2	4	11039	22	ETH-86160
GAEN0071	210.5	12994.5	2	4	11044	22	ETH-86162
GAEN0071	214.5	12990.5	2	4	11053	22	ETH-86164
GAEN0071	218.5	12986.5	2	4	11018	23	ETH-86166
GAEN0071	222.5	12982.5	2	4	11061	22	ETH-86168
GAEN0071	225	12980	1	4	11023	22	ETH-86170
GAEN0071	227	12978	1	4	11037	22	ETH-86172
GAEN0071	229	12976	1	4	11052	22	ETH-86174
GAEN0071	231	12974	1	4	11067	22	ETH-86176
GAEN0071	233	12972	1	4	11035	22	ETH-86178
GAEN0071	235	12970	1	4	11041	23	ETH-86180
GAEN0071	237.5	12967.5	2	4	11056	22	ETH-86182
GAEN0071	242	12963	3	4	11021	22	ETH-86184
GAEN0071	250.5	12954.5	2	4	11042	23	ETH-86187
GAEN0071	254.5	12950.5	2	4	11030	23	ETH-86189
GAEN0071	258.5	12946.5	2	4	11033	23	ETH-86191
GAEN0071	262.5	12942.5	2	4	11052	23	ETH-86193
GAEN0071	266.5	12938.5	2	4	11050	23	ETH-86195
GAEN0071	270.5	12934.5	2	4	11047	23	ETH-86197
GAEN0071	274.5	12930.5	2	4	10997	23	ETH-86199
GAEN0071	278.5	12926.5	2	4	10981	23	ETH-86201
GAEN0071	282.5	12922.5	2	4	11002	23	ETH-86203
GAEN0071	286.5	12918.5	2	4	10963	23	ETH-86205
GAEN0071	290.5	12914.5	2	4	11009	23	ETH-86207
GAEN0071	294.5	12910.5	2	4	11004	23	ETH-86209
GAEN0071	298.5	12906.5	2	4	10999	24	ETH-86211
GAEN0071	302.5	12902.5	2	4	10983	24	ETH-86213
GAEN0071	306.5	12898.5	2	4	10964	24	ETH-86215
GAEN0071	312	12893	3	4	10961	24	ETH-86217
GAEN0071	316.5	12888.5	2	4	10967	24	ETH-86220
GAEN0071	320.5	12884.5	2	4	10975	23	ETH-86222
GAEN0071	324.5	12880.5	2	4	10958	23	ETH-86224
GAEN0071	328.5	12876.5	2	4	10992	24	ETH-86226
GAEN0071	330.5	12874.5	2	4	10984	24	ETH-86227
LAND0004	5.5	12309.5	2	0	10394	22	ETH-87465
LAND0004	7	12308	1	0	10394	22	ETH-87466
LAND0004	8	12307	1	0	10384	22	ETH-87467
LAND0004	9	12306	1	0	10373	22	ETH-87468

LAND0004	10.5	12304.5	2	0	10389	22	ETH-87469
LAND0004	12	12303	1	0	10373	22	ETH-87470
LAND0004	13	12302	1	0	10380	22	ETH-87471
LAND0004	14	12301	1	0	10420	22	ETH-87472
LAND0004	15	12300	1	0	10407	23	ETH-87473
LAND0004	16	12299	1	0	10424	22	ETH-87474
LAND0004	17	12298	1	0	10395	22	ETH-87475
LAND0004	18	12297	1	0	10425	22	ETH-87476
LAND0004	19	12296	1	0	10430	22	ETH-87477
GAEN0102	111	12546	1	4	10511	21	ETH-71434
GAEN0102	112	12545	1	4	10523	21	ETH-71435
GAEN0102	113	12544	1	4	10525	21	ETH-71436
GAEN0102	116	12541	1	4	10476	21	ETH-71439
GAEN0102	117	12540	1	4	10514	21	ETH-71440
GAEN0102	118.5	12538.5	1	4	10517	21	ETH-71441
GAEN0102	120	12537	1	4	10536	21	ETH-71442
GAEN0102	121	12536	1	4	10512	22	ETH-71443
GAEN0102	122	12535	1	4	10565	21	ETH-71444
GAEN0102	123.5	12533.5	2	4	10510	21	ETH-71445
GAEN0102	125	12532	1	4	10576	21	ETH-71446
GAEN0102	126	12531	1	4	10528	21	ETH-71447
GAEN0102	127	12530	1	4	10554	21	ETH-71448
GAEN0102	128	12529	1	4	10545	21	ETH-71449
GAEN0102	129	12528	1	4	10544	22	ETH-71450
GAEN0102	130	12527	1	4	10534	21	ETH-71451
GAEN0102	131	12526	1	4	10557	21	ETH-71452
GAEN0102	132	12525	1	4	10530	21	ETH-71453
GAEN0102	135.5	12521.5	2	4	10540	21	ETH-71455
GAEN0102	139.5	12517.5	2	4	10551	21	ETH-71457
GAEN0102	141.5	12515.5	2	4	10561	21	ETH-71458
GAEN0102	143.5	12513.5	2	4	10513	21	ETH-71459
BINZ0020	2	12829	1	4	10945	23	ETH-67192
BINZ0020	70	12761	1	4	10856	31	ETH-70645
BINZ0020	122.5	12708.5	2	4	10607	31	ETH-70646
BINZ0020	127	12704	1	4	10581	30	ETH-70647
BINZ0020	1	12831	1	4	10894	21	ETH-87231
BINZ0020	2	12829	1	4	10924	21	ETH-87232
BINZ0020	4	12827	1	4	10903	21	ETH-87233
BINZ0020	6	12825	1	4	10942	21	ETH-87234
BINZ0020	8	12823	1	4	10899	21	ETH-87235
BINZ0020	10	12821	1	4	10921	21	ETH-87236
BINZ0020	12	12819	1	4	10930	21	ETH-87237
BINZ0020	16	12815	1	4	10906	21	ETH-87239
BINZ0020	18	12813	1	4	10878	21	ETH-87240
BINZ0020	20	12811	1	4	10920	21	ETH-87241
BINZ0020	22	12809	1	4	10915	21	ETH-87242
BINZ0020	24	12807	1	4	10912	21	ETH-87243
BINZ0020	26	12805	1	4	10919	21	ETH-87244
BINZ0020	28	12803	1	4	10929	21	ETH-87245
BINZ0020	32	12799	1	4	10914	21	ETH-87247
BINZ0020	34	12797	1	4	10946	21	ETH-87248
BINZ0020	36	12795	1	4	10912	20	ETH-87249
BINZ0020	38	12793	1	4	10931	21	ETH-87250
BINZ0020	40	12791	1	4	10945	21	ETH-87251
BINZ0020	42	12789	1	4	10844	21	ETH-87252
BINZ0020	44	12787	1	4	10888	21	ETH-87253
BINZ0020	48	12783	1	4	10895	21	ETH-87255
BINZ0020	50	12781	1	4	10898	21	ETH-87256
BINZ0020	52.5	12778.5	2	4	10893	21	ETH-87257
BINZ0020	57.5	12773.5	2	4	10836	21	ETH-87258
BINZ0020	14	12817	1	4	10915	21	ETH-87238
BINZ0020	30	12801	1	4	10913	21	ETH-87246
BINZ0020	46	12785	1	4	10866	21	ETH-87254
BINZ0020	59.5	12771.5	2	4	10901	21	ETH-87259
BINZ0020	63.5	12767.5	2	4	10859	21	ETH-87260
BINZ0020	66	12765	1	4	10774	21	ETH-87261

BINZ0020	68	12763	1	4	10853	21	ETH-87262
BINZ0020	70	12761	1	4	10856	21	ETH-87263
BINZ0020	72	12759	1	4	10795	21	ETH-87264
BINZ0020	74	12757	1	4	10796	21	ETH-87265
BINZ0020	76	12755	1	4	10800	21	ETH-87266
BINZ0020	77	12754	1	4	10749	21	ETH-87267
BINZ0020	78.5	12752.5	2	4	10823	21	ETH-87268
BINZ0020	81	12750	1	4	10815	21	ETH-87269
BINZ0020	83	12748	1	4	10796	21	ETH-87270
BINZ0020	85	12746	1	4	10763	21	ETH-87271
BINZ0020	87	12744	1	4	10795	21	ETH-87272
BINZ0020	88	12743	1	4	10800	21	ETH-87273
BINZ0020	89	12742	1	4	10791	21	ETH-87274
BINZ0020	90	12741	1	4	10794	21	ETH-87275
BINZ0020	91	12740	1	4	10756	21	ETH-87276
BINZ0020	92	12739	1	4	10774	21	ETH-87277
BINZ0020	93	12738	1	4	10762	21	ETH-87278
BINZ0020	94	12737	1	4	10746	21	ETH-87279
BINZ0020	95	12736	1	4	10745	21	ETH-87280
GAEN0025	3.0	12777.0	1	4	10829.3	23.5	ETH-65911
GAEN0025	6.0	12774.0	1	4	10848.9	23.5	ETH-65914
GAEN0025	8.0	12772.0	1	4	10843.1	23.5	ETH-65916
GAEN0025	10.0	12770.0	1	4	10846.0	23.4	ETH-65918
GAEN0025	11.0	12769.0	1	4	10843.3	23.4	ETH-65919
GAEN0025	12.0	12768.0	1	4	10857.6	23.4	ETH-65920
GAEN0025	13.0	12767.0	1	4	10875.8	23.5	ETH-65921
GAEN0025	14.0	12766.0	1	4	10913.0	23.6	ETH-65922
GAEN0025	15.0	12765.0	1	4	10886.5	23.6	ETH-65923
GAEN0025	16.0	12764.0	1	4	10820.4	23.5	ETH-65924
GAEN0025	17.0	12763.0	1	4	10863.3	23.5	ETH-65925
GAEN0025	18.0	12762.0	1	4	10835.4	23.5	ETH-65926
GAEN0025	19.0	12761.0	1	4	10848.9	23.5	ETH-65927
GAEN0025	20.0	12760.0	1	4	10804.3	23.5	ETH-65928
GAEN0025	21.0	12759.0	1	4	10808.8	23.5	ETH-65929
GAEN0025	22.0	12758.0	1	4	10821.7	23.5	ETH-65930
GAEN0025	23.0	12757.0	1	4	10819.4	23.6	ETH-65931
GAEN0025	24.0	12756.0	1	4	10849.4	23.5	ETH-65932
GAEN0025	25.0	12755.0	1	4	10816.3	23.5	ETH-69670
GAEN0025	26.0	12754.0	1	4	10775.8	23.5	ETH-69671
GAEN0025	27.0	12753.0	1	4	10774.2	23.5	ETH-69672
GAEN0025	28.0	12752.0	1	4	10756.2	23.5	ETH-69673
GAEN0025	29.0	12751.0	1	4	10776.9	23.6	ETH-69674
GAEN0025	30.0	12750.0	1	4	10754.3	23.5	ETH-69675
GAEN0025	31.0	12749.0	1	4	10747.1	23.5	ETH-69676
GAEN0025	32.0	12748.0	1	4	10713.5	20.8	ETH-70158
GAEN0025	33.0	12747.0	1	4	10715.8	20.9	ETH-70159
GAEN0025	34.0	12746.0	1	4	10724.4	21.0	ETH-70160
GAEN0025	35.0	12745.0	1	4	10748.9	21.1	ETH-70161
GAEN0025	36.0	12744.0	1	4	10756.7	21.0	ETH-70162
GAEN0025	37.0	12743.0	1	4	10762.9	21.0	ETH-70163
GAEN0025	38.0	12742.0	1	4	10727.5	20.9	ETH-70164
GAEN0025	39.0	12741.0	1	4	10777.3	21.0	ETH-70165
GAEN0025	40.0	12740.0	1	4	10771.2	20.9	ETH-70166
GAEN0025	41.0	12739.0	1	4	10769.0	20.9	ETH-70167
GAEN0025	42.0	12738.0	1	4	10796.3	21.0	ETH-70168
GAEN0025	43.0	12737.0	1	4	10749.8	21.0	ETH-70169
GAEN0025	44.0	12736.0	1	4	10714.5	21.0	ETH-70170
GAEN0025	45.0	12735.0	1	4	10717.8	21.2	ETH-70171
GAEN0025	46.0	12734.0	1	4	10729.5	20.9	ETH-70172
GAEN0025	47.0	12733.0	1	4	10740.6	20.8	ETH-70173
GAEN0025	48.0	12732.0	1	4	10747.5	20.7	ETH-70174
GAEN0025	49.0	12731.0	1	4	10726.0	20.7	ETH-70175
GAEN0025	50.0	12730.0	1	4	10719.8	20.8	ETH-70176
GAEN0025	15.0	12765.0	1	4	10,892	20	ETH-70910
GAEN0025	16.0	12764.0	1	4	10,894	20	ETH-70911
GAEN0025	17.0	12763.0	1	4	10,939	20	ETH-70912

GAEN0025	18.0	12762.0	1	4	10,906	20	ETH-70913
GAEN0025	19.5	12760.5	2	4	10,894	20	ETH-70914
GAEN0025	20.5	12759.5	2	4	10,900	22	ETH-70915
GAEN0025	23.0	12757.0	1	4	10,898	20	ETH-70916
GAEN0025	25.00	12755.0	1	4	10,862	20	ETH-70917
GAEN0025	26.0	12754.0	1	4	10,846	20	ETH-70918
GAEN0025	27.0	12753.0	1	4	10,838	20	ETH-70919
GAEN0025	28.0	12752.0	1	4	10,865	20	ETH-70920
GAEN0025	29.0	12751.0	1	4	10,820	20	ETH-70921
GAEN0025	30.0	12750.0	1	4	10,885	20	ETH-70922
GAEN0025	31.0	12749.0	1	4	10,843	20	ETH-70923
GAEN0025	32.0	12748.0	1	4	10,841	20	ETH-70924
GAEN0025	34.0	12746.0	1	4	10,888	20	ETH-70926
GAEN0025	35.0	12745.0	1	4	10,852	20	ETH-70927
GAEN0025	36.0	12744.0	1	4	10,824	20	ETH-70928
GAEN0025	37.0	12743.0	1	4	10,848	20	ETH-70929
GAEN0025	38.0	12742.0	1	4	10,873	20	ETH-70930
GAEN0025	39.0	12741.0	1	4	10,853	20	ETH-70931
GAEN0025	40.0	12740.0	1	4	10,844	20	ETH-70932
GAEN0025	41.0	12739.0	1	4	10,850	20	ETH-70933
GAEN0025	42.0	12738.0	1	4	10,831	20	ETH-70934
GAEN0025	43.0	12737.0	1	4	10,870	20	ETH-70935
GAEN0025	52.0	12728.0	1	4	10709.2	22.4	ETH-81063
GAEN0025	53.0	12727.0	1	4	10,703	23	ETH-81064
GAEN0025	54.0	12726.0	1	4	10653.6	22.3	ETH-81065
GAEN0025	56.0	12724.0	1	4	10675.9	22.2	ETH-81066
GAEN0025	57.0	12723.0	1	4	10676.9	22.4	ETH-81067
GAEN0025	58.0	12722.0	1	4	10679.7	22.3	ETH-81068
GAEN0025	59.0	12721.0	1	4	10686.6	22.5	ETH-81069
GAEN0025	61.0	12719.0	1	4	10719.0	22.7	ETH-81071
GAEN0025	63.0	12717.0	1	4	10700.5	22.5	ETH-81073
GAEN0025	67.0	12713.0	1	4	10681.8	22.2	ETH-81076
GAEN0025	68.0	12712.0	1	4	10677.0	22.8	ETH-81077
GAEN0025	69.0	12711.0	1	4	10655.7	22.4	ETH-81078
GAEN0025	71.0	12709.0	1	4	10681.1	22.4	ETH-81080
GAEN0025	73.0	12707.0	1	4	10664.7	22.1	ETH-81082
GAEN0025	74.0	12706.0	1	4	10665.2	23.1	ETH-81083
GAEN0025	76.0	12704.0	1	4	10667.9	23.0	ETH-81084
GAEN0025	77.0	12703.0	1	4	10635.2	23.0	ETH-81085
GAEN0025	78.0	12702.0	1	4	10676.6	22.5	ETH-81086
GAEN0025	79.0	12701.0	1	4	10602.2	25.2	ETH-81087
GAEN0025	81.0	12699.0	1	4	10623.9	22.3	ETH-81089
GAEN0025	82.0	12698.0	1	4	10653.1	22.3	ETH-81090
GAEN0025	83.0	12697.0	1	4	10676.2	22.5	ETH-81091
GAEN0025	93.0	12687.0	1	4	10687.8	23.0	ETH-81100
GAEN0025	98.0	12682.0	1	4	10612.3	22.6	ETH-81104
GAEN0025	104.0	12676.0	1	4	10633.1	22.5	ETH-81110
GAEN0025	51.0	12729.0	1	4	10,723	20	ETH-81062
GAEN0025	62.0	12718.0	1	4	10,647	21	ETH-81072
GAEN0025	64.0	12716.0	1	4	10,654	20	ETH-81074
GAEN0025	66.0	12714.0	1	4	10,652	20	ETH-81075
GAEN0025	70.0	12710.0	1	4	10,637	20	ETH-81079
GAEN0025	80.0	12700.0	1	4	10,606	20	ETH-81088
GAEN0025	84.0	12696.0	1	4	10,615	20	ETH-81092
GAEN0025	86.0	12694.0	1	4	10,604	20	ETH-81093
GAEN0025	88.0	12692.0	1	4	10,624	20	ETH-81095
GAEN0025	89.0	12691.0	1	4	10,649	20	ETH-81096
GAEN0025	90.0	12690.0	1	4	10,637	20	ETH-81097
GAEN0025	91.0	12689.0	1	4	10,643	20	ETH-81098
GAEN0025	94.0	12686.0	1	4	10,608	20	ETH-81101
GAEN0025	96.0	12684.0	1	4	10,606	20	ETH-81102
GAEN0025	102.0	12678.0	1	4	10,580	20	ETH-81108
GAEN0025	103.0	12677.0	1	4	10,578	21	ETH-81109

Appendix B

Publications

B.1 Primary author

Sookdeo, A., Kromer, B., Adolphi, F., Beer, J., Büntgen, U., Friedrich, M., Guidobaldi, G., Helle, G., Hogg, A., Muscheler, R., Nievergelt, D., Palmer, J., Pauly, M., Reinig, F., Tegel, W., Treydte, K., Turney, C., Synal, H.-A., Wacker, L. in preparation.Here comes the Sun: Solar variability in Allerød and Younger Dryas from a redefined high resolution atmospheric ^{14}C record. Quaternary Science Reviews

Sookdeo, A., Kromer, B., Büntgen, U., Friedrich, M., Friedrich, R., Helle, G., Pauly, M., Nievergelt, D., Reinig, F., Treydte, K., Synal, H.-A., Wacker, L. in press. Quality Dating: A protocol for reproducible high precision ^{14}C dates applied to Late Glacial wood. Radiocarbon

Sookdeo, A., Wacker, L., Fahrni, S., McIntyre, C.P., Friedrich, M., Reinig, F., Nievergelt, D., Tegel, W., Kromer, B., Büntgen, U., 2017. Speed dating: a rapid way to determine the radiocarbon age of wood by EA-AMS. Radiocarbon 59, 933-939.

Sookdeo, A., Cornett, J., Kieser, W.E., 2015. Optimizing production of Pb beams for ^{205,210}Pb analysis by Accelerator Mass Spectrometry. Nuclear Instruments and Methods in Physics Research Section B: Beam Interactions with Materials and Atoms 361, 450-453.

Sookdeo, A., Cornett, R.J., Zhao, X.L., Charles, C.R.J., Kieser, W.E., 2016. Measuring ^{210}Pb by accelerator mass spectrometry: a study of isobaric interferences of ^{204,205,208}Pb and ^{210}Pb. Rapid Communications in Mass Spectrometry 30, 867-872.

B.2 Co-authorship

Wacker, L., Bollhalder, S., Sookdeo, A., H.-A Synal. Accepted. Re-evaluation of the New Oxalic Acid Standard with AMS. Nuclear Instruments and Methods in Physics Research Section B: Beam Interactions with Materials and Atoms

Pauly, M., Helle, G., Miramont, C., Büntgen, U., Treydte, K., Reinig, F., Guibal, F., Sivan, O., Heinrich, I., Riedel, F., Kromer, B., Balanzategui, D., Wacker, L., Sookdeo, A., Brauer, A., 2018. Subfossil trees suggest enhanced Mediterranean hydroclimate variability at the onset of the Younger Dryas. Scientific reports 8, 13980.

Reinig, F., Gärtner, H., Crivellaro, A., Nievergelt, D., Pauly, M., Schweingruber, F., Sookdeo, A., Wacker, L., Büntgen, U., 2018. Introducing anatomical techniques to subfossil wood. Den-

drochronologia 52, 146-151.

Reinig, F., Nievergelt, D., Esper, J., Friedrich, M., Helle, G., Hellmann, L., Kromer, B., Morganti, S., Pauly, M., Sookdeo, A., Tegel, W., Treydte, K., Verstege, A., Wacker, L., Büntgen, U., 2018. New tree-ring evidence for the Late Glacial period from the northern pre-Alps in eastern Switzerland. Quaternary Science Reviews 186, 215-224.

Appendix C

Radiocarbon dating course

As part of effort to get undergraduates at ETH engaged in ^{14}C I along with L. Wacker and C.Welte created an advanced student laboratory course. I have taught this course for last two year as ETH. It was received extremely as I awarded the Experimental Innovation award. The manual for the course is presented below.

Radiocarbon Dating

Advanced Student Laboratory Course

Laboratory for Ion Beam Physics
Fall 2016

Adam Sookdeo, Caroline Welte and Lukas Wacker

Version 1.1
30.09.2016

Overview

You will gain a concrete knowledge of radiocarbon dating. In this course you will learn about ^{14}C, why it is useful and why radiocarbon is used in various scientific disciplines. In addition, you will gain an understanding about the workings of Accelerator Mass Spectrometer, a tool crucial for dating radioisotopes. And you will gain comprehensive knowledge of the statistical analysis involved in ^{14}C dating.

1.1 Task

In this course you will chemically extract cellulose from Swiss trees. Along with the extracted cellulose you will measure blanks, standards and reference materials on a MIni CArbon DAting System (MICADAS). With the raw data you will perform the necessary data reduction and submit a report showing their calculations and answering the questions below:

i) What is radiocarbon dating?
ii) Determine the decay constant for radiocarbon, using Libby's half-life.
iii) What is the activity of 2 grams of modern of carbon? (Hint use atmospheric $^{14}C/^{12}C$ ratio)
iv) Briefly explain why $^{14}C^{+}$ ions collected in gas ionization chamber rather than a Faraday cup.
v) Why do we isolate cellulose?
vi) What consequences would you expect if no "pre" was prepared?
vii) Why is the graphitization process carried out in the excess of hydrogen?
viii) Why does the pressure decrease overtime during the graphitization process?
ix) Describe a situation in how we can determine if contamination come from the BABA bleaching treatment.
x) If the extraction potential is -40kV what is the momentum of $^{14}C^{-}$?
xi) If the radius of low energy magnet is 25cm, what is the magnetic field required for $^{14}C^{-}$? What should the pulse offset be for $^{12}C^{-}$?
xii) If the terminal voltage on the tandem accelerator is 200kV and the radius of the high energy magnet is 35cm, what is the magnetic field required for $^{14}C^{+}$?
xiii) If the radius of the ESA is 35cm, what magnetic field is required?

2 Introduction

2.1 What is Radiocarbon Dating?

Radiocarbon (^{14}C) dating can be used to determine the age of a variety of materials. The principle of ^{14}C dating was first presented in 1949 by W.F. Libby (Arnold 1949) for which he was awarded the Nobel Prize in chemistry in 1960. The concept was, and still is that material containing carbon can be dated based on the radioactivity of ^{14}C, as ^{14}C decays according to the law of radioactive decay. To understand properties of radioactive decay there are a few basic principles to understand:

$$\text{Activity } (A) = -dN/dt = \lambda N \quad (1)$$

Where N is number of atoms, t is time and λ is the decay constant (yr^{-}). The change is number of atoms from time 0 (N_0) is thus represented as

$$N = N_0 e^{-\lambda t} \quad (2)$$

The half-life ($t_{1/2}$) is the time it takes for half of the original number of radioactive atoms to decay. Libby reported the half-life ($t_{1/2}$) of ^{14}C as 5568 yr, which is called the conventionally Libby half-life (Libby 1955). Later, it was discovered the $t_{1/2}$ of ^{14}C is 5730 yr (Godwin 1962).To further understand the principles of ^{14}C dating we must know how it is formed and where it is incorporated.

^{14}C is continually formed and in the upper atmosphere by the interaction of neutrons formed as secondary cosmic ray particles and nitrogen atoms.

$$^{14}N + \text{neutron} \rightarrow {}^{14}C + \text{proton}$$

^{14}C atoms combine with oxygen to form CO_2 that is transported and mixed throughout the atmosphere, where it dissolves into the oceans and enters the biosphere via photosynthesis. The formation and decay of ^{14}C is somewhat constant throughout time; the $^{14}C/^{12}C$ ratio in the atmosphere is approximately 1.2×10^{-12}. This noteworthy because as certain organisms grow and incorporate carbon into their structures they incorporate ^{14}C from the atmosphere. However, the $^{14}C/^{12}C$ ratio in the organism is not the same as the atmosphere because of isotope fractionation.

Trees, for instance, experience fractionation because for photosynthesis stomata cells preferentially up-take lighter CO_2 from the atmospheres, figure 1.

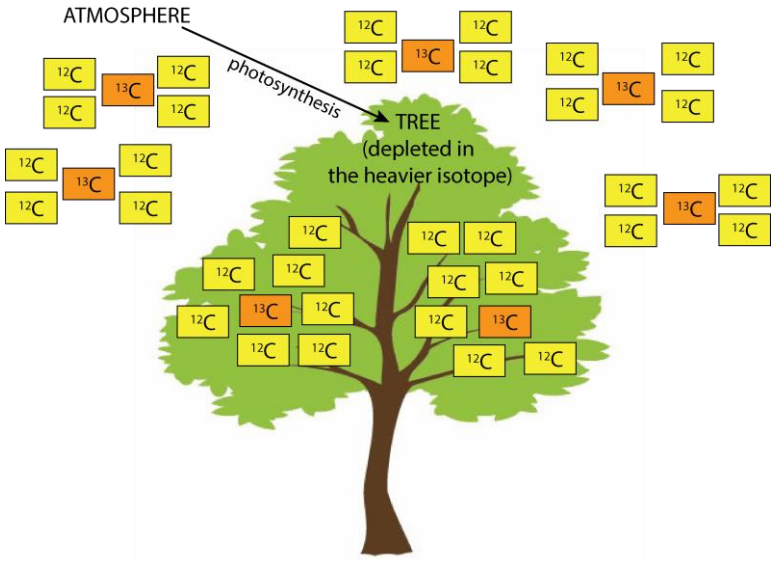

Figure 1 Schematic of mass-dependent fractionation happening between ^{12}C and ^{13}C during photosynthesis. The ratio in the tree is shifted towards the lighter isotope compared to the atmosphere.

In this case, the $^{14}C/^{12}C$ ratios in trees are depleted compared to atmosphere. Fractionation affects have to be taken into account to accurately ^{14}C date samples, something we discuss in the calculations part of this course.

Furthermore, it is important to note that when CO_2 exchange is stopped (when a tree-ring is formed or the tree dies), the radiocarbon clock begins to tick. This is because as no new ^{14}C is being incorporated the $^{14}C/^{12}C$ ratio begins to drop, the decrease in this ratio can be used a marker of time. For instance, if $^{14}C/^{12}C$ ratio of a tree was determined to be roughly 50% (1 $t_{1/2}$) of what it is today, the tree would have grown ~5568 years ago. However, this date is not completely accurate because we assumed that the $^{14}C/^{12}C$ ratio in the atmosphere has been constant between now and when this tree grow, this known as a "uncalibrated date" or "conventional date." Conventional dates are reported using Libby's half-life and are calculated as follows:

$$T = -8033 \cdot \ln(F^{14}C) \qquad (3)$$

Where T is time and $F^{14}C$ is fraction modern (a term discussed in section 2.3). Although, this can be useful, we know the atmospheric ^{14}C concentration varies over time; therefore, to accurately date an object, the uncalibrated ^{14}C age needs to be converted into a calendar age.

In order to determine the calendar age of an object uncalibrated ^{14}C date needs to be compared to a ^{14}C record that is independently dated, for example through dendrochronology, where the age is derived from tree-ring counting. Tree-rings are used because as mentioned they uptake ^{14}C from the atmosphere while growing. The same trees-rings can be assigned a calendar age by dendrochronology.

Dendrochronology is the evaluation of tree-ring growth patterns and by creating groups of trees with overlapping by extending tree-ring growth patterns a chronology is formed. There are two types of dendrochronology dates i) *absolute* and ii) *floating*. A dendrochronology date is considered to be absolute dated when part of the chronology is

cross-dated to the present. If no cross date to the present can be established a dendrochronology record is considered floating. Floating chronologies can have multiple placements throughout time, e.g. placement one 500 BP, placement two 7000 BP. A more accurate placement (±20 years) can established, by ^{14}C dating a subset of a floating chronology. In addition, absolutely dated dendrochronology records have been ^{14}C dated to create a calibration curve.

By ^{14}C dating numerous absolutely dated dendrochronology records a calibration curve extending back to roughly ~12 000 years Before Present (BP) has been established. For samples older than 12 000 BP, marine sediments are used to fill the calibration curve. The combination of dendrochronology and marine records form the International Calibration curve (Intcal, (Reimer 2013)), which extends back to 50 000 BP.

For the practical part of this course you will prepare and ^{14}C date tree-rings that are part of a Swiss floating chronology.

Questions

i) What is radiocarbon dating?
ii) Determine the decay constant for radiocarbon, using Libby's half-life.
iii) What is the activity of 2 grams of modern of carbon? (Hint use atmospheric $^{14}C/^{12}C$ ratio)

2.2 Radiocarbon measurements

Initially, measurements of ^{14}C were carried out via radiometric techniques as the decay of ^{14}C emits beta particles with energies around 0.15MeV. Radiometry measurements of ^{14}C have been come to known as the "conventional method". The conventional method involves using a beta-counter to measure the number of beta particles emitted from the nucleus per unit time by the decay of ^{14}C. At times, samples were chemically treated to remove material with ^{14}C that changes over time; for instance in trees lignin's continually incorporated ^{14}C overtime, while cellulose once it is formed does not incorporate new ^{14}C content. Chemically treated samples were combusted in the presence of excess oxygen to produce CO_2 and the CO_2 was measured by a gas proportional beta counter. With the induction of liquid scintillation counters, samples were converted to benzene and a scintillator was added so that the samples could be measured photometrically. Both techniques require approximately 1 gram or more of carbon and counting times could vary between days and month depending on the desired precision and age of the material. Nevertheless, the conventional method was used since the discovery of ^{14}C to the late 1990's and even sporadically nowadays. However, today the determination of ^{14}C is dominated by Accelerator Mass Spectrometry (AMS).

AMS was first used in 1977 in Toronto, Canada at the IsoTrace Laboratory (Bennett 1978). The main goals of AMS at the time were to eliminate the isobar ^{14}Ne and measure ^{14}C by directly counting the proportion of ^{14}C atoms to ^{13}C and ^{12}C (which requires accelerations of atoms).

By directly measuring ^{14}C results in much quicker measurements times (1-3days) and yield sensitivities of up to 4 orders of magnitude higher than beta-counting. There are various types of AMS setups but the principles remain the same.

Commonly AMS systems are equipped with Cs^+ sputter ion sources that are used to produce negative ions a process known as ionization. This is particular advantageous for ^{14}C analysis as the enormously abundant isobar ^{14}N does not form negative ions and is

suppressed at this ionization stage. The negative molecules are extracted and sometimes run through an electrostatic analyser (ESA) that allows for the passage ions with specific energy and the negative ions are always run through a low energy magnet. The low energy magnet is a momentum filter and thus is used to discriminate and select for $^{12,13,14}C^-$ ions. The selected ions are then fed through a tandem accelerator. Here the ions are accelerated towards the terminal at high potential (sometimes several MV) where the ions enter the "stripper" (either a gas filled volume or a foil). The stripper is important for two reasons: i) the charge state of the entering ions is changed to positive, as electrons are being ripped off. The newly formed positive ions are accelerated back to ground potential. ii) Interfering molecules (e.g. $^{13}CH^-$) injected together with the rare isotope (^{14}C), are destroyed. Depending on the setup, either outer electrons are ripped off and molecules break apart due to Coulomb explosion, or the molecules dissociate due to multiple collisions with the residual gas in the stripper. After the tandem accelerator the positive ions are passed through a High-Energy (HE) magnet and $^{12,\,13}C^+$ are collected in Faraday cups, while $^{14}C^+$ ions in addition to the HE magnet are passed through a ESA and are counted in a gas ionization chamber.

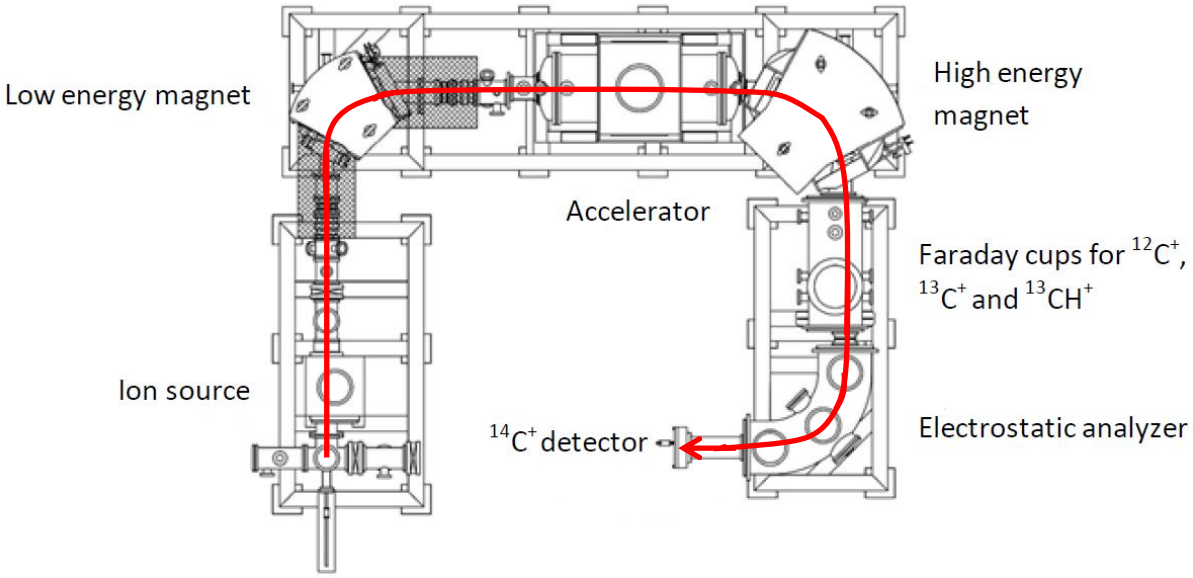

Figure 2 Image of standard AMS set-up. The path of the ions is indicated by red lines. Imagine modified from Synal et al 2007.

For this course we will be using a small AMS with a terminal voltage of only 200 kV know as MIni CArbon DAting System (MICADAS). Further details about this machine will be discussed in section 2.2.

Questions

iv) Briefly explain why $^{14}C^+$ ions collected in gas ionization chamber rather than a Faraday cup.

3 Methods

There is a wide range of materials that can be dated using the ^{14}C method, from wooden objects to paintings to archaeological artifacts to bone, but regardless of the chemical compositions some sort of sample preparation is required for precise ^{14}C measurements. Sample preparation is done for primarily two reasons, 1) eliminate containments or remove part of the material that contains interchangeable ^{14}C and/or 2) to ensure that material is in an appropriate chemical state to be measured (either CO_2 gas or graphite).

It is beyond the scope of this course to discuss all the various sample preparation techniques. Instead we will focus on one of the most commonly ^{14}C dated objects, wood.

3.1 Sample Preparation

Students will be responsible for preparing and graphitizing their samples (3-5) along with two standards and two blanks

Prior to any chemical preparation steps, samples measured at the LIP must be labeled by entering them into the database via a program called LAMA. This can be done using an excel sheet that will be provided. *It will be the job of the student to fill in the relevant sections of this excel sheet for their samples.* When the excel sheet is uploaded into LAMA, a unique ETH sample ID consisting of a lab prefix (ETH) and a number (ETH-xxxxx) will be generated. LAMA will also create a preparation number (e.g. xxxxx.1 if it was a second preparation it would xxxxx.2) this number will be used as a label for the chemical extraction procedure. And lastly the program LAMA will we create a target ID (e.g. xxxxx.1.1) this number is used when samples are being measured. You can print samples by right clicking on sample number in the LAMA and selecting print label. Be sure to label your vials accordingly. Samples and targets are contained in Eppendorf vials, but preparation vials are 10 ml glass tubes from Faust.

Once you have labeled your vials, weigh in 20-30 mg of your sample and place it into 10 ml glass tube. To ensure the best possible results make sure your samples are cut into thin pieces.

3.1.1 Isolation of Cellulose

Typically, when dating wood/plant material only the easily exchangeable components are removed (such as roots). This is normally clean enough for standard radiocarbon measurement but in some cases it is desirable to have pure cellulose; part of wood/plant that has remained unchanged and immobile since it formed (Hoper 1998). *For this course students will isolate cellulose from tree-rings and measure the ^{14}C content with a MICADAS*.

For the samples you weighed in the preparation vial we will chemically extract cellulose with an Base-Acid-Base-Acid-Bleach (BABAB) protocol, figure 3 (Brock et al. 2010, Němec 2010a)). The base steps removes humic acid and degrades part of the cell walls particularly the polysaccharide component, the acid step eliminates carbonates and the bleaching step degrades ligands (Le Moigne 2010). In-between, changing solutions from base to acid (or acid to base) samples have to be washed twice with MiliQ water. It is not required to wash the samples with MiliQ water when switching from an acid to bleach.

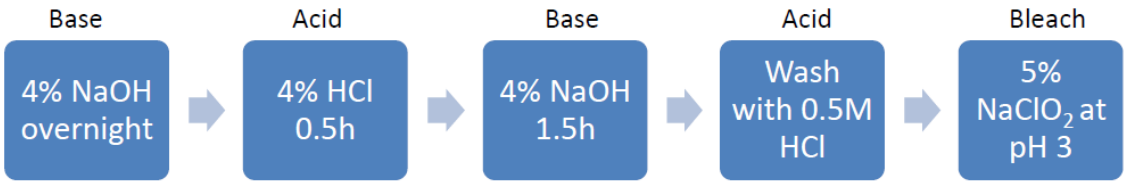

Figure 3 Reaction protocol to extract cellulose from wood.

The BABAB procedure from start to finish takes about two days. After, bleaching the samples are washed twice (or more until cellulose is white) with MiliQ water and the samples are placed in a freezer for an hour. Then the samples are placed into a freeze dryer overnight to remove H_2O.

Once the samples are dried, weigh out approx. 2.5-3 mg of cellulose in aluminum capsules (4x4x11 mm^3, Elementar, Germany) and place it in the target vial. Please write down the weight of the samples on the vial. For a single sample, please make a duplicate, but instead of using a target label, on the vial write *PRE*, the last 3 digits of the ETH number and the weight. A preconditioning (PRE) sample is used when switching between samples with large radiocarbon activity difference i.e. a standard and a blank or a blank and sample etc, to help remove cross contamination from the graphitization process, see Wacker 2013.

Questions

v) Why do we isolate cellulose?
vi) What consequences would you expect if no "pre" was prepared?

3.1.2 Conversion to Graphite

For the purpose of this course we will measure the carbon content of our samples in a solid state as graphite rather than in a gaseous state. Graphite measurements by AMS are a standard in the field and provide the highest precision, with uncertainties down to 2‰ (±16yrs uncalibrated). While gas measurements are also possible these measurements are not as precise but can be done much quicker.

Graphitization is a chemical process in which CO_2 is converted to graphite with the use extreme temperatures, excess H_2 and Fe as a catalyst (Vogel 1984)(Němec 2010b). For graphitization, the samples are placed in an Elemental Analyser (EA, vario MICRO cube, Elementar) where the material is combusted and carbon is converted to CO_2 in the presence of excess oxygen. The CO_2 produced is then fed into a 3rd generation Automated Graphitization Equipment (AGE-3) (Wacker 2013). Students will be will responsible for graphitizing their samples.

For the graphitization, the following preparations are necessary: first add Fe from the dispenser to 7 glass tubes and place and securely tighten the tubes in the AGE-3 (Figure 4). Then in the AGE-3 program, click on "Condition" and under options make sure "Auto" is deselected. Conditioning will heat up the Fe and air in the tube (to 500 °C) and the system will perform a leak test, to ensure the system is airtight. If the leak test fails, tighten the connection of the tube to the AGE. When the leak test passes, the tubes will be evacuated, filled with hydrogen and heated to the same temperature three times, to clean the Fe and to get rid of any carbon present in the glass tubes. While this process is ongoing you can start preparing the EA.

Before you enter the sample information, reference the sample carousel wheel and check that it is on position 1. This is accomplished in the EA program (VarioMirco) by

selecting XXX then wheel position and in dialog box check all samples removed and reference run then click OK. Afterwards, you can start a “RunIn” to ensure that EA that there is no left over carbon from previous combustion and the combustion process is running smoothly. To start a RunIn, enter “1” in the first row of the weight column, in the name column write or select RunIn and in the method column select G_50s (this method will add excess oxygen for 50 seconds).

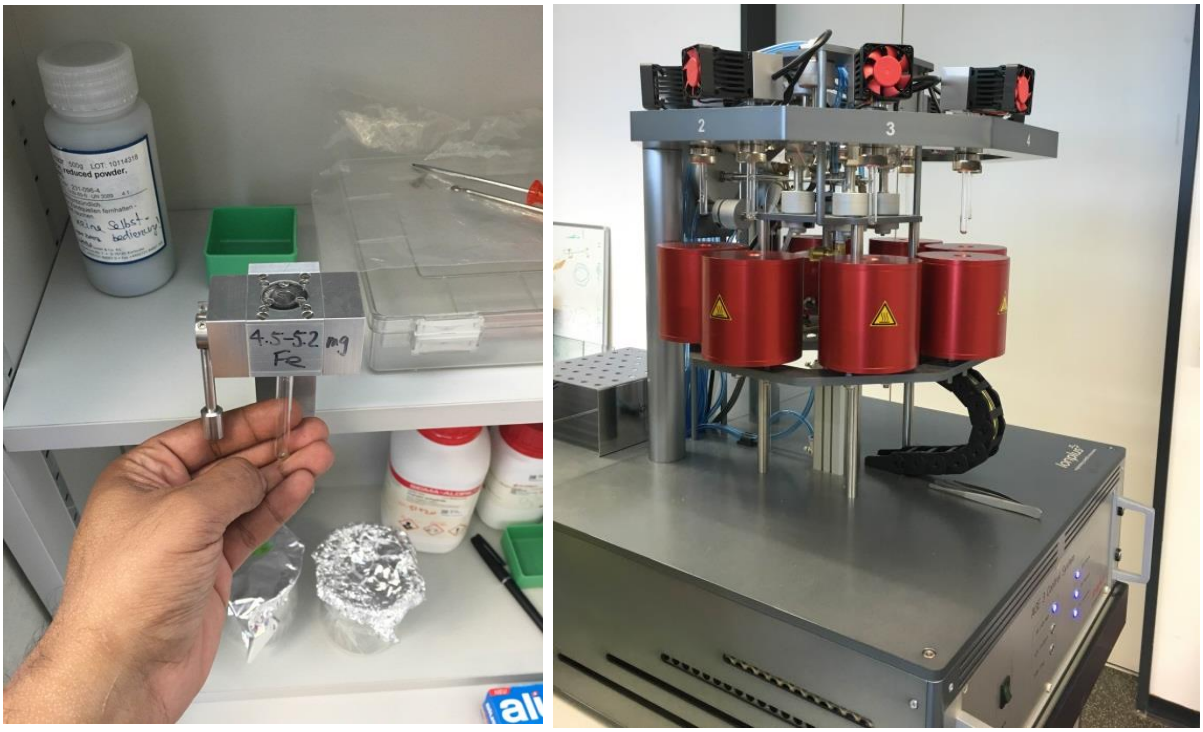

Figure 4 The left figure shows the Fe dispenser with a glass tube, which is being filled with Fe. The right figure depicts the AGE-3 system with the glass tubes containing Fe inserted.

Once the AGE is done with conditioning, select single run and a chromatograph will appear on the right side of the screen. Do RunIn’s until the peak area corresponding to carbon (at 200 to 300 seconds) is a straight line without peaks or bumbs. Once the system is clean, you can enter the sample info into the EA list and load your samples into the EA. Enter sample information into the weight, name (sample ID), and method columns (G_50s). The row number corresponds to the wheel position number; therefore, it is recommended to double check that both numbers match.

Go back to the AGE program. Under options make sure *Auto*, *EA Sleep* and *Remove* H_2O are selected. Click on sample, it will ask if you are sure click YES and each reactor will be loaded with a sample and excess hydrogen. Once all 7 reactors are loaded, the ovens will heat up to 500 °C the graphitization process will begin, which takes 120min. You can occasionally check in on the reaction; you should see a decrease in pressure in the reactors overtime.

Once the graphitization process is finished and water is removed from the reactors, transfer the graphite to cathode targets and press them. This process will be demonstrated to you in the lab. The pressed targets are then entered in LAMA as being squeezed and a magazine is created using the program PrepMag40. The details on how to accomplish this will be shown to you in the lab. Lastly, the pressed targets are then loaded in a magazine and are ready for analysis (see section 2.2).

Questions

vii) Why is the graphitization process carried out in the excess of hydrogen?
viii) *Why does the pressure decrease overtime during the graphitization process*?

3.1.3 Standards, Blanks and Reference Materials

Standards

In order to determine the radiocarbon age of a sample, a standard with a known ^{14}C activity is measured. The principal modern radiocarbon standard is National Institute of Standards and Technology (N.I.S.T) Oxalic Acid ($C_2H_2O_4$). There are two types of Oxalic acid designated as HOxI and HOxII. The activity of HOxI is defined as 95% of the ^{14}C activity from the year 1950 (Stuiver 1980). This is equivalent to activity wood from 1890 AD. Wood from 1890 AD was chosen as the radiocarbon standard because it was growing prior to the fossil fuel-fossil fuels are radiocarbon dead-effects of the industrial revolution. The activity of 1890 AD wood is corrected for radioactive decay to 1950. Thus 1950, is year 1 BP by convention in radiocarbon dating and is deemed to be the 'present'.

The HOxI standard was made from a crop of 1955 sugar beet. In total there was roughly 1000 lbs made; however, as ^{14}C measurements became more common supplies began to dwindle and HOxI was no longer commercially available. Therefore, another standard was created, HOxII. HOxII was made from a crop of 1977 French beet molasses (Stuiver 1983). The ^{14}C activity of HOxII is about ~23% higher than that of HOxI. *For this course we will use HOxII.*

Blanks

The weighted means of $^{14}C/^{12}C$ for a blank is subtracted from the weighted means of sample to account for background correction. Therefore it is important that a blank be radiocarbon dead (older than 50 kyrs BP).

There are two types of blanks that we will be using for this course, a *chemical blank* that is phthalic anhydride (PhA) and *process blanks* that are brown coal and Kauri wood. PhA is a chemical that is radiocarbon dead i.e. made from carbon that is over 100 kyrs old. The chemical blank is graphitized but is not chemical treated with a BABA bleaching method. In this respect, if a PhA blank shows signs of contamination it likely came from the graphitization process or pressing of targets. Brown coal and Kauri are both older than 200 kyrs and are subjected to a BABA bleaching treatment as well as graphitization.

Reference material

A reference material is a sample that has been measured in the past by previous laboratories and there is consensus value in the community. The reference material should be selected carefully as it is used for quality assurance of the analysis. Ideally it is of similar age to the samples being measured. The measurements of reference material should be within 1-2 σ of the cited value. If the measurements fall outside of the 2 σ range the measurement may be considered void. For this course we will use part of a Kauri tree (TK121) that grew over 10 kBP ago and has been measured by five other laboratories (Hogg 2013).

Note: for blanks, standards and reference materials have an ETH sample ID but we will show you how to create a preparation and a target ID.

Question

ix) Describe a situation in how we can determine if contamination come from the BABA bleaching treatment

3.2 MIni CArbon DAting System (MICADAS)

Programs Panda, Squirrel and Nemo will be discussed in during the course.

For this course will be using a MICADAS with permanent magnets at both the Low-Energy (LE) and High-Energy (HE) side to ^{14}C date our samples. There are many components to a MICADAS and it is beyond the scope of this course to go into details of all of them; rather, we will focus on the `tunable` components. Tunable components are part of a MICADAS that are regularly modified to maximize measurement precision and efficiency, which is done using the program Panda.

i. The extraction potential controls the potential of the extraction lens that in turn affects the energy and path of ions after Cs^+ sputter. Therefore, at the start of a measurement we tune the extraction potential by maximizing the $^{13}C^+$ current.

ii. x- and y-steerers: The x- and y-steers are changed by altering the Potential Energy (PE) and this then modifies where the carbon ion beams sit in space. The x- and y-steers are tuned by again maximizing the $^{13}C^+$ current by changing the PE of the steers. In addition, a box lens is used to change the divergence of the carbon ion beams and thus the focal point of beam. This is done to ensure the focal point of the beam has maximum transmission through the LE magnet, which is considered to be at maximum by optimizing $^{13}C^+$ current.

iii. LE-magnet: A LE scan is performed to minimize fractionation of carbon isotopes caused by AMS. The currents of $^{12}C^+$ and $^{13}C^+$ should lay on top of each over a varying magnet fields and minimal fractionation is expected when the ratio of $^{13}CH/^{12}C$ is stable over a narrow magnetic field this is called as a flat-top range. Before you begin a LE scan note the set-point of the LE magnet then lower the magnetic field until background currents are measured in the Faraday cups. In Squirrel start a LE scan with steps sizes of +300, the magnetic field should then slowly increase in stepwise manner all the while the $^{12,\,13}C^+$ currents are measured. If no flat-top region is observed at the set-point of LE magnet the pulses of either A (^{12}C) and/or B (^{13}C) are changed accordingly. The pulse system makes uses of small accelerators tubes to accelerate either $^{12}C^-$ or $^{13}C^-$ so that they have the momentum as $^{14}C^-$ and thus follow the same path through the LE magnet. By lowering the PE of pulse A, $^{12}C^-$ will deflected less by the magnet and vice versa. Once the pulse A and B are adjusted so that at the set-point LE magnet is in a flat top region, the LE magnet is tuned.

iv. HE-magnet: Normally a tuning of the HE magnet is not necessary. However, it should be checked that the carbon beams are passing through the centre of the magnet. For a HOxII we expect the ratio of $^{14}C/^{12}C$ to $1.5x10^{-12} \pm 0.3x10^{-12}$, the position of the ^{14}C beam is checked by manually decreasing the aperture of the beam path by 3 mm, the beam path itself is slightly over 6 mm. Therefore, expect roughly half the citied ratio when the slit is inserted by 3 mm. However, if the ratio is not between 0.8-0.85 the voltage of accelerator or the pressure in stripper is adjusted rather than HE magnet as the magnet is permanent. Increasing the voltage in the accelerator or decreasing the pressure of the stripper results in more energetic carbon ions and vice versa.

When the appropriate ratio of $^{14}C/^{12}$ is reached, the slit has to be manually retracted by 3 mm.

The extraction potential, y-steerer and box-lens can be adjusted a final time to double check that maximum currents are achieved. Afterwards, you can start your measurement (this will be discussed in person).

Questions

x) If the extraction potential is -40kV what is the momentum of $^{14}C^-$?

xi) If the radius of low energy magnet is 25cm, what is the magnetic field required for $^{14}C^-$? What should the pulse offset be for $^{12}C^-$?

xii) If the terminal voltage on the tandem accelerator is 200kV and the radius of the high energy magnet is 35cm, what is the magnetic field required for $^{14}C^+$?

xiii) If the radius of the ESA is 35cm, what magnetic field is required?

3.3 Statistical Data Evaluation

Once the measurements are complete students will be given the raw data and it will be their job to calculate the radiocarbon age of their samples along with errors. Below students will find the relevant information that they need.

3.3.1 Overview

In general, calculations follow the procedure suggested by Stuiver and Polach (Stuiver 1977). An overview of the calculations performed for ^{14}C analysis can be seen in figure 5.

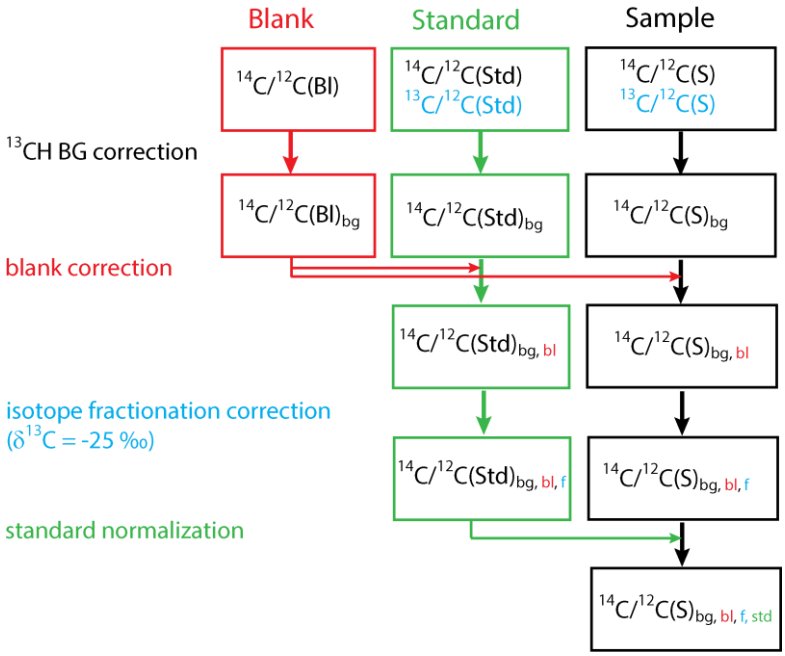

Figure 5 Overview of the data evaluation steps necessary after ^{14}C analysis. The abbreviations stand for: bg = background corrected, bl = blank subtracted, f = mass dependent fractionation corrected, std =after standard normalization, Bl = blank, Std = standard, S = sample.

3.3.2 Calculations

You will have to use the equations and methods below to evaluate your data!

Typically, two uncertainties are calculated when performing radiocarbon analyses: the "internal error" derived from counting statistics (i.e. Poisson) and the external error, which corresponds to the standard deviation of the repeated measurements. Both errors should be on the same order and comparing them gives information about the quality of the measurement (χ^2-test).

Often, a dependency of the measured ratios on the beam current intensities can be observed during ^{14}C measurements. In the following, weighted mean values are calculated according to:

$$\langle X \rangle = \frac{\sum_i (X_i \cdot p_i)}{\sum_i p_i}$$, where the weighting factor p_i is given by $p_i = {}^{12}C \cdot t$

Below is table abbreviations used for calculations:

Table 1 Overview of variables and their abbreviations used in the calculations:

Abbreviation	Physical quantity	Value (if applicable)
R	$^{14}C/^{12}C$ ratio (x 10^{-12})	
δ	absolute internal uncertainty (counting statistics)	
σ	absolute external uncertainty (standard deviation)	
^{14}C	^{14}C counts	
^{12}C or ^{13}C	^{12}C or ^{13}C current [µA]	
$^{13}C_{mo}$	^{13}C(H) current [µA]	
$k \pm \delta_k$	correction factor for molecular background	(200 ± 50)*t
t	runtime [sec] = net measurement time (dead time of detector not included)	
$F^{14}C_{OXII,nom}$	Nominal $F^{14}C$ of OxII standard	1.34066
$\delta^{13}C_{OxII,nom}$	Nominal $\delta^{13}C$ of OxII standard	-17.8‰

3.3.2.1 Background Correction

The MICADAS instrument is equipped with three Faraday cups on the HE-side: two cups are installed to detect the $^{12,13}C^+$ currents. The third one is used to measure $^{13}C^+$ions coming from broken-up ^{13}CH molecules. A small portion of these broken-up molecules reaches the detector, where it is counted as if it was a $^{14}C^+$ ion. Generally, a linear correlation is observed between the detected $^{14}C/^{12}C$-ratio and the measured $^{13}C(H)/^{12}C$ ratio for blank samples.

This allows us to perform a background correction, which is applied to all runs of all samples (blanks, standards, samples):

$$R_{mol} = \frac{^{14}C - k \cdot ^{13}C_{mol}}{^{12}C} \tag{4}$$

The uncertainty is derived from the error propagation of the uncertainty δ_k of the correction factor k (experimentally determined) and of the uncertainty $\delta^{14}C$, which corresponds to the counting statistics error of the ^{14}C counts.

$$\delta_{mol} = \sqrt{\delta_{14C}^2 + \delta_k^2} \tag{5}$$

3.3.2.2 Blank subtraction

The weighted mean of all background corrected blank measurements and its corresponding uncertainty are calculated. Sometimes, when blanks are analysed for either long periods of time or a large number of blanks are measured the uncertainty of the blanks may be underestimated. Therefore, the uncertainty of blank should be set to 3×10^{-16} unless it is higher.

A relative blank correction is performed to all standards and samples:

$$R_{mol,bl} = R_{mol} - \langle R(bl)_{mol} \rangle \tag{6}$$

The uncertainty is derived by error propagation:

$$\delta_{mol,bl} = \sqrt{\delta_{bl}^2 + \delta_{mol}^2} \tag{7}$$

3.3.2.3 Mass-Fractionation correction

Fractionation and δ-notation

The different isotopic ratios of different reservoirs are expressed in the δ-notation (definition see first part of equation (5)).

In order to ^{14}C date it is crucial to translate the stable isotope ratio of the material to be dated into a substance with a known stable isotope ratio. Since in ^{14}C dating, the activity of the sample is compared to the activity of tree rings, it is translated into the activity it would have if it was wood with a $\delta^{13}C$ = -25‰. For mass-dependent fractionation, the mathematical relation between the fractionation of $^{13}C/^{12}C$ and $^{14}C/^{13}C$ is known and is approximately quadratic. This allows us to perform a fractionation correction using the following calculations:

The $\delta^{13}C$ of ***standards and samples*** (in the following equation denoted as "sample") for each run is calculated according to:

$$\delta^{13}C_{sample} := \left(\frac{(^{13}C/^{12}C)_{sample}}{(^{13}C/^{12}C)_{VPDB}} - 1 \right) \cdot 1000 = \left(\frac{(^{13}C/^{12}C)_{sample} \cdot (1 + \delta^{13}C_{std}/1000)}{\langle (^{13}C/^{12}C)_{std} \rangle} - 1 \right) \cdot 1000 \tag{8}$$

For the algebraic transformation, the fraction was expanded with $(^{13}C/^{12}C)_{Std}/(^{13}C/^{12}C)_{VPDB}$.

The abbreviations represent:

$(^{13}C/^{12}C)_{VPDB}$	limestone standard (Friedman 1982)
$(^{13}C/^{12}C)_{sample}$	stable isotope ratio of the sample
$\langle(^{13}C/^{12}C)_{std}\rangle$	weighted mean of stable isotope ratio of all standards
$\delta^{13}C_{std}$	nominal isotopic signature of the primary standard

Fractionation correction

The fractionation $F_{13/12}$ happening between ^{13}C and ^{12}C is known to be approximately quadratic compared to the fractionation $F_{14/12}$ between ^{14}C and ^{12}C. Considering this relationship, the fractionation correction can be performed with all ***samples and standards*** according to:

$$R_{mol,bl,f} = R_{mol,bl} \cdot F_{14/12} \approx R_{mol,bl} \cdot F(_{13/12})^2 = R_{mol,bl} \cdot \left(\frac{(^{13}C/^{12}C)_{-25}}{(^{13}C/^{12}C)_{sample}} \right)^2 = \\ = R_{mol,bl} \cdot \left(\frac{0.975}{(1+\delta^{13}C_{sample}/1000)} \right)^2 \tag{9}$$

For the last algebraic transformation, the definition of $\delta^{13}C$ was substituted.
The uncertainty is calculated from:

$$\delta_{mol,bl,f} = \delta_{mol,bl} \cdot \left(\frac{0.975}{(1+\delta^{13}C_{sample}/1000)} \right)^2 \tag{10}$$

3.3.2.4 Standard normalisation

Mean of standards, χ^2-test and sample scatter:

For the standard normalization, we first have to calculate the weighted mean $\langle R(std)_{mol,bl,f} \rangle$ of all fractionation corrected standards and its uncertainty. This is also a good point to get an estimate on the quality of our measurement by comparing the internal $\langle \delta(std)_{mol,bl,f} \rangle$ and external uncertainty $\langle \sigma(std) \rangle$. The χ^2 is calculated according to:

$$\chi^2 = \sum_i^N \frac{(\bar{x} - x_i)^2}{\sigma_i^2} \tag{11}$$

An approximation of the χ^2_{red} is given by:

$$\chi^2_{red} = \frac{\chi^2}{(N-1)} \approx \frac{\sigma^2}{\delta^2} = \frac{\langle \sigma(std) \rangle^2}{\langle \delta(std)_{mol,bl,f} \rangle^2} \tag{12}$$

For a measurement to be considered good, the χ^2_{red} should be close to 1, which means that the internal and external uncertainty are in agreement. A χ^2_{red} that is larger than 2 is a sign for an additional external error source that has not been taken into consideration. This could be caused by variation in target preparation or measurement instabilities. Consequently, the scatter of the samples is larger than the error derived from counting statistics. By adding an additional external error σ^2_{ext}, this can be corrected for:

$$\langle \sigma(std) \rangle_{mol,bl,f,ext} = \sqrt{\delta(std)^2_{mol,bl,f} + \sigma^2_{ext}} \tag{13}$$

From long-term experience it is known, that the value of σ^2_{ext} is typically around 0.2% (verify this by calculating the χ^2_{red} and also check the limits in a table for a confidence interval of 95%).

Standard normalization calculations

There are numerous conventions to report radiocarbon data. Depending on the purpose, the most suitable reporting mode should be chosen. There are three different ways of reporting ^{14}C data:

i) Absolute activity
ii) Activity ratio (ratio between the absolute activities of a sample and the standard)
iii) Relative activity (comparable to δ-notation of stable isotopes)

In this lab course the unit Fraction Modern ($F^{14}C$) will be used, which falls under category (ii). It corresponds to the activity ratio of the sample relative to the radiocarbon standard (OxII). $F^{14}C$ does not change with time and it is independent of the year of measurement.

$$F^{14}C = \langle R_{mol,bl,f}(sample) \rangle \cdot \frac{F^{14}C_{OxII,nom}}{\langle R(std)_{mol,bl,f} \rangle} \tag{14}$$

Where $\langle R_{mol,bl,f}(sample) \rangle$ is the weighted mean of the $^{14}C/^{12}C$ ratios of all runs of the sample and $\langle R(std)_{mol,bl,f} \rangle$ is the weighted mean of corrected $^{14}C/^{12}C$ ratios of all standards and $F^{14}C_{OxII,nom}$ is nominal fraction modern value of OxII standard.

The uncertainty of the $F^{14}C$ value of each run is derived from propagating the error of $R_{mol,bl,f}$ and of $\langle R(std)_{mol,bl,f} \rangle$.

$$\delta_{F^{14}C} = F^{14}C \cdot \sqrt{\left(\frac{\delta_{mol,bl,f}}{R_{mol,bl,f}}\right)^2 + \left(\frac{\langle \delta(std)_{mol,bl,f} \rangle}{\langle R(std)_{mol,bl,f} \rangle}\right)^2} \tag{15}$$

4 Appendix

4.1 Constant Contamination

Chemical purification methods such as gas chromatography (GC) or high-pressure liquid chromatography (HPLC) allow radiocarbon analyses on specific organic compounds. However, only small amounts of these substances (i.e. low µg level) can be isolated with commercially available GC and HPLC instruments in a single run. Thus, even very small contaminations will bias any radiocarbon determination of the isolated compound.
The measured $^{14}C/^{12}C$ ratio (R_m) is always a superposition of the $^{14}C/^{12}C$ ratios of both the sample (R_s) and the contaminant (R_c). R_s can be extracted applying the model of constant contamination, if the total carbon content (m_m) and the contaminant mass (m_c) and $^{14}C/^{12}C$ ratio (R_c) is known:

$$R_s = \frac{R_m \cdot m_m - R_c \cdot m_c}{m_m - m_c}$$

To determine $m_c \pm \sigma_{m_c}$ and $R_c \pm \sigma_{R_c}$ reliably multiple processing standards of different but known radiocarbon content (typically modern and dead) need to be analyzed. The relative errors for both parameters are typically large compared with the relative measurement uncertainty of m_m. Error propagation yields σ_{R_s}:

$$\sigma_{R_s}^2 = \left[\sigma_{m_c}\left(\frac{R_m \cdot m_m - R_c \cdot m_c}{(m_m - m_c)^2} - \frac{R_c}{(m_m - m_c)}\right)\right]^2 + \left[\sigma_{m_m}\left(\frac{R_m}{(m_m - m_c)} - \frac{R_m \cdot m_m - R_c \cdot m_c}{(m_m - m_c)^2}\right)\right]^2 + \left[\sigma_{R_m}\frac{m_m}{m_m - m_c}\right]^2 + \left[\sigma_{R_c}\frac{-m_c}{m_m - m_c}\right]^2$$

As an example, the uncertainty σ_{R_s} of the $^{14}C/^{12}C$ ratio of a 10 µg C sample is shown as a function of its radiocarbon content in Fig 1. For the constant contamination two typical values are used (red and blue lines). A minimal absolute uncertainty is observed when the radiocarbon level of the contamination (here R_c = 0.6 ± 0.2 $F^{14}C$) is close to that of the sample R_s. We note that the contribution from the counting statistics (σ_{R_m}, dashed lines) to the total uncertainty σ_{R_s} is relatively small, even for a contamination of only 0.6 ± 0.2 µg C. In reality, contaminations of more than 1 µg C are frequently observed.

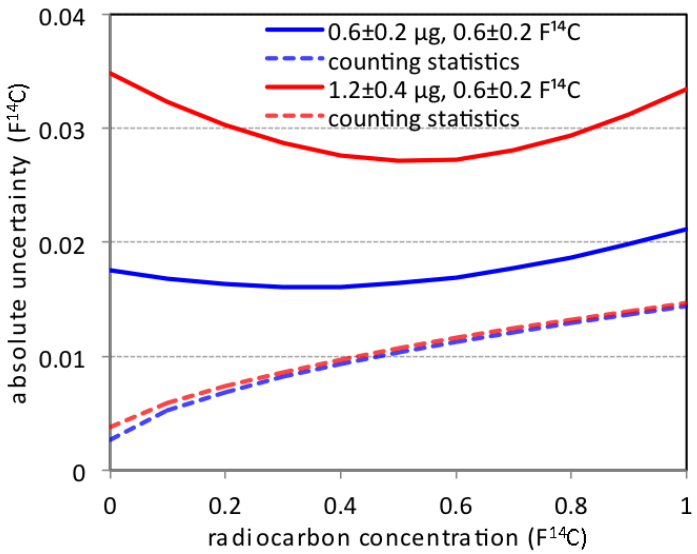

Figure 6 *Calculated total uncertainty of a 10 µg C sample as a function of its radiocarbon concentration. The dashed lines show the uncertainty from counting statistics; the solid lines represent the total uncertainty including a constant contamination with 0.6 ± 0.2 µg C (blue) and 1.2 ± 0.4 µg C (red) with 0.6 ± 0.2 $F^{14}C$, respectively.*

The results shown in Fig. 1 demonstrate the importance to precisely determine the total carbon amount and the $^{14}C/^{12}C$ ratio of the contaminant when processing very small radiocarbon samples. The propagated uncertainties derived from counting statistics alone are not the limiting factor anymore.

5 Citations

J.R. Arnold and W.F. Libby. *Age determinations by radiocarbon content - Checks with samples of known age*. Science **110** (1949) 678-680

H. Godwin. *Half-life of radiocarbon*. Nature **195** (1962) 984-&

P.J. Reimer, E. Bard, A. Bayliss, J.W. Beck, P.G. Blackwell, C.B. Ramsey, C.E. Buck, H. Cheng, R.L. Edwards, M. Friedrich, P.M. Grootes, T.P. Guilderson, H. Haflidason, I. Hajdas, C. Hatte, T.J. Heaton, D.L. Hoffmann, A.G. Hogg, K.A. Hughen, K.F. Kaiser, B. Kromer, S.W. Manning, M. Niu, R.W. Reimer, D.A. Richards, E.M. Scott, J.R. Southon, R.A. Staff, C.S.M. Turney and J. van der Plicht. *Intcal13 and Marine13 Radiocarbon Age Calibration Curves 0-50,000 Years Cal Bp* Radiocarbon **55** (2013) 1869-1887

C.L. Bennett, R.P. Beukens, M.R. Clover, D. Elmore, H.E. Gove, L. Kilius, A.E. Litherland and K.H. Purser. *Radiocarbon Dating with Electrostatic Accelerators - Dating of Milligram Samples*. Science **201** (1978) 345-347

D. Elmore. *Additions to the Rochester MP tandem for ultrasensitive isotope analysis* Proc. 1st Conf. on Radiocarbon Dating with Accelerators, ed. H.E. Gove, University of Rochester, Rochester NY, USa (1978) 220-238

S.T. Hoper, F.G. McCormac, A.G. Hogg, T.F.G. Higham and M.J. Head *Evaluation of wood pretreatments on oak and cedar*. Radiocarbon **40** (1998) 45-50

N. Němec, L. Wacker, I. Hajdas and H. Gäggeler. *Alternative Methods for Cellulose Preparation for AMS measurement*. Radiocarbon **52** (2010a) 1358-1370

L. Wacker, S.M. Fahrni, I. Hajdas, M. Molnar, H.A. Synal, S. Szidat and Y.L. Zhang *A versatile gas interface for routine radiocarbon analysis with a gas ion source* Nuclear Instruments & Methods in Physics Research Section B-Beam Interactions with Materials and Atoms **294** (2013) 315-319

J.S. Vogel, J.R. Southon, D.E. Nelson and T.A. Brown. *Performance of Catalytically Condensed Carbon for Use in Accelerator Mass-Spectrometry*. Nuclear Instruments & Methods in Physics Research Section B-Beam Interactions with Materials and Atoms **5** (1984) 289-293

N. Němec, L. Wacker and H. Gäggeler*Optimization of the Graphitization Process at AGE-1*. Radiocarbon **52** (2010b) 1380-1393

M. Stuiver. *Workshop on ^{14}C data reporting*. Radiocarbon **22** (1980) 964-966

M. Stuiver. *International Agreements and the Use of the New Oxalic-Acid Standard* Radiocarbon **25** (1983) 793-795

A. Hogg, C. Turney, J. Palmer, J. Southon, B. Kromer, C.B. Ramsey, G. Boswijk, P. Fenwick, A. Noronha, R. Staff, M. Friedrich, L. Reynard, D. Guetter, L. Wacker and R. Jones

The New Zealand Kauri (Agathis Australis) Research Project: A Radiocarbon Dating Intercomparison of Younger Dryas Wood and Implications for Intcal13
Radiocarbon **55** (2013) 2035-2048

M. Stuiver and H.A. Polach. *Reporting of C-14 Data - Discussion* .Radiocarbon **19** (1977) 355-363

Le Moigne N, Navard P. *Dissolution mechanisms of wood cellulose fibres in NaOH–water. Cellulose*. Cellulose **17** (2010):31-45.

Wacker L, Bonani G, Friedrich M, Hajdas I, Kromer B, Nemec M, Ruff M, Suter M, Synal HA, Vockenhuber C. *MICADAS: routine and high-precision radiocarbon dating*. Radiocarbon. **52** (2010):252.

Wacker L, Němec M, Bourquin J. *A revolutionary graphitisation system: fully automated, compact and simple*. Nuclear Instruments and Methods in Physics Research Section B: Beam Interactions with Materials and Atoms. **268** (2010):931-4.

Synal HA, Stocker M, Suter M. *MICADAS: a new compact radiocarbon AMS system*. Nuclear Instruments and Methods in Physics Research Section B: Beam Interactions with Materials and Atoms. **259** (2007):7-13.

Appendix D

Acknowledgments

I would like to express my heartfelt gratitude to my supervisor Dr. Lukas Wacker for his suggestions, encouragement and relentless criticism. From the start Dr. Wacker was invested in the project picking me up from the airport when I arrived from Canada, showing me the lab, giving me readings and strongly suggesting I take German lessons. Without his eagerness to push the project and myself forward, I would have not been able to complete my Ph.D. Additionally, special thanks to Prof. Bernd Kromer, for his tireless discussions on radiocarbon and words of encouragement.

I would also like give recognition to the head of the group, Prof. Hans-Arno Synal who allowed us to measure as many samples as we wanted and for trusting in the work we were doing. Prof. Synal only showed positivity towards me and made my time at ETH extremely enjoyable. Likewise, huge thank you Dr. Marcus Christl who when we meet at conference during my M.Sc believed me when I said I wanted to do a Ph.D. and helped facilitate my transition into the group.

To my fellow Ph.D. Binz members Maren and Freddy, thanks for listening to my presentations and putting up with all of emails with new placements of chronologies, especially Freddy. To rest of Binz team, Ulf, Gerd, Danny, Willy, Giulia and Kerstin you have my gratitude for making this project successful.

Maria and Mantana thank you for putting up with all my questions when I started and getting me set-up in the radiocarbon lab. To my colleagues over the years, Caro, Sascha, Nuria, Martina, Anita, Chrisi, Laura, Maxi, Daniele, Anne-Maire, Klaus-Ulrich, Oliva and Stefano you made my time at ETH one to remember.

Max and Tarek you guys kept me sane and became my closest friends, thanks of all the laughs.

Special thanks to my Mom, Tara who showed me only love and support when I decided to move overseas, love you. My brothers, Matt, Martin and Ryan you guys always made me feel at home and it meant a lot to have you here when I defended, love you all. And to my fianceé, Taylor for always standing by my side through it all, you are amazing and I am lucky to have you.